UNIVERSITÀ DELLA CALABRIA

UNIVERSITÀ DELLA CALABRIA

Dipartimento di Fisica

Dottorato di Ricerca in

Scienze e Tecnologie Fisiche, chimiche e dei Materiali in convenzione con il Consiglio Nazionale delle Ricerche (CNR)

CICLO

XXXIV

TITOLO TESI

Scaling properties and multifractal dynamic of greenhouses gases

Settore Scientifico Disciplinare

Fis/06 Fisica per il Sistema Terra e per il Mezzo Circumterrestre

Coordinatore: Prof.ssa Gabriella Cipparrone

Firma Firma oscurata in base alle linee guida del Garante della privacy

Supervisori: Dott.ssa Francesca Sprovieri

Firma Firma oscurata in base alle linee guida del Garante della privacy

Dott. Francesco Carbone

Firma Firma oscurata in base alle linee guida del Garante della privacy

Dottorando: Dott. Giovanni Tripicchio

Firma Firma oscurata in base alle linee guida del Garante della privacy

A mia nipote Francesca

Contents

Abstract

In questo lavoro é stata effettuata un'analisi estensiva delle proprietá di scala intraday, attraverso l'utilizzo di differenti metodologie, delle componenti che costituiscono le serie temporali dei GHG tracers, CO_2, CH_4 e CO, campionate all'osservatorio di Monte Curcio tra il 2015 e il 2017. Attraverso l'utilizzo dell'Empirical Mode Decomposition e della Mutual information sono state estrapolate le componenti fast e slow che caratterizzano l'evoluzione temporale giornaliera dei GHG tracers. Dall'analisi della varianza, delle funzioni di struttura, degli spettri di potenza e attraverso i metodi DFA e MFDFA é stato possibile studiare le proprietá di scala, definite dal coefficiente Hurst, delle componenti fast e slow che costituiscono le serie temporali dei GHG tracers. Da questa analisi si evidenziano differenti proprietá locali delle fluttuazioni che caratterizzano queste componenti in base alla scala e al periodo temporale scelto. Lo studio attraverso la funzione di struttura ha permesso di relazionare l'evoluzione temporale della componente fast della CO_2 e della CH_4 con il fenomeno di turbolenza in atmosfera. Tuttavia, la discrepanza degli esponenti di scala suggerisce che le dinamiche delle componenti slow sono legate a fenomeni di diversa natura che contribuiscono con maggiore energia. Il coefficiente Hurst della componente slow a grandi scale (H_s) della CO_2 presenta una modulazione temporale. In accordo con la teoria dell'invarianza di scala della turbolenza, questa modulazione potrebbe essere relazionata con i principali drivers ambientali che guidano la dinamica delle concentrazioni della CO_2. In questo contesto é stato considerato il processo fotosintesi-respirazione, attraverso l'analisi degli indici vegetazionali EVI e NDVI, e la variazione dell'altezza del Boundary Layers (BL). L'alto valore di correlazione misurato tra le variazioni mensili di questi indici e la variazione del coefficiente H_s suggeriscono che questi fenomeni giocano un ruolo principale nel definire le proprietá frattali intraday della CO_2. I risultati ottenuti risultano essere di aiuto per l'implementazione di nuove metodologie nei modelli climatici-atmosferici.

Abstract

This work presents an extensive analysis of scaling properties of the intra-day components that constitute the temporal behaviour of GHG tracers (CO_2, CH_4 and CO), recorded during the period from 2015 to 2017 at Monte Curcio Observatory. Through the application of Empirical Mode Decomposition and Mutual Information methods, fast and slow components have been highlighted, which characterize the dynamics of GHG tracers at small and large scales, respectively. From analyses of these two components, it was possible to investigate the scaling properties related to the Hurst coefficient. The results highlight different local properties that characterize the fluctuations of the two components, particularly according to the scale and time period under investigation. The discrepancy of scaling exponents suggests that the dynamics of slow components are related to different phenomena that contribute more energy (force) to the process, while fast components are governed by small-scale turbulent processes. The Hurst coefficient of slow component for CO_2 exhibits a large-scale temporal modulation, which may be related to the main environmental drivers responsible for dynamics of CO_2 concentrations. In this context, the photosynthesis-respiration process has been considered, through the analysis of the vegetation indexes EVI and NDVI, and the variation of the Planetary Boundary Layer (PBL) height. The high correlation value measured between the monthly variations of these two indexes and the variation of H_s coefficient suggests that these phenomena played a primary role in defining the intra-day fractal properties of the CO_2. The results obtained are useful to the parametrization of sub-grid processes in atmospheric-climatic models, while providing a temporal evolution of the emission maps of the analyzed GHG tracers.

Chapter 1

Introduction

The Earth's climate system over the millennia has constantly changed, altering its balance. It manifests as a distribution of the set of meteorological conditions (pressure, temperature, humidity, etc.) that characterize it for long periods. This system is considered complex in physical terms and is in dynamic equilibrium determined by the interaction between the forcing that belongs to subsets, in this case the atmospheric, biological, hydrological etc., characterized by phenomena that develop on very different temporal and / or spatial scales, from molecular to continental oceanic and atmospheric circulations. These subsets interact with each other and involve feedback mechanisms that can reinforce (positive feedbacks) or inhibit (negative feedbacks) climate change. Thus, the equilibrium condition, in which the climate system is found, responds to variation in the forcing in a continuous way or by reaching a critical threshold beyond which abrupt changes can occur [1].

Among the subsets that interject and describe the Earth's climate system, the one that varies most in space and time is the atmospheric one. The processes that characterize the evolution of the atmosphere vary from the microscale (from a few Cm to a few Km), i.e., phenomena of the turbulent nature of the Planetary Boundary Layers (PBL), to large-scale phenomena ($> 1000\ Km$), i.e., continental and planetary scale processes. The atmosphere, in general is a mixture of gases characterized among which by the presence of nitrous oxide (N_2O), carbon dioxide (CO_2), methane (CH_4) and water vapour (H_2O), which are called greenhouse gases (GHG). The action of GHG is determined in the alteration of the energy balance of the atmosphere-Earth system through the variation of the ratio between incoming solar radiation and outgoing infrared radiation. According to the analysis of satellite observation conducted by Loeb et al. [2], the globally average value of outgoing, infrared radiation is 238.5

Wm^{-2}. Increasing concentrations of greenhouse gases results in increasing temperatures both in the lower atmosphere (troposphere) and at the earth's surface [3]. The change in gas concentrations is due to both natural-type phenomena (oceanic, volcanic emissions, etc.) and anthropogenic interference phenomena. Anthropogenic interference contributes unequivocally in the natural evolution of the climate system, and increasing GHG concentrations act as climate-altering agents.

The global monitoring of carbon dioxide (CO_2), methane (CH_4) and monoxide carbon (CO) in the atmosphere has been performed more and more actively during the past 10–30 years. The studies performed on GHG tracers concentrations are different in kind and ranging between the analysis of the intrinsic periodicity detected in the spatio-temporal measurements of the datasets. In particular on the seasonal periodicity of CO_2 detected by Keeling et al. [4] at Mauna Loa and subsequent further analyses elsewhere in other locations, mainly related to growth trend and cyclic patterns on different time scales[5],[6],[7]. In fact, from the studies conducted, it can be inferred that the cyclic pattern of GHG tracers have diurnal, seasonal and synoptic variations which are related to local or global physical phenomena that define their dynamics[5], [6]. In general, multiple studies have been conducted on spatio-temporal sampling of GHG tracers concentrations regarding correlation with global phenomena such as the index of the southern oscillation (SOI) and with El Niño occurrences [8], the impact of the Earth's biosphere on the CO_2 cycle [9], [10], the role of Planetary Boundary Layers in tracer transport models [11], or the atmospheric transport that plays the dominant role in controlling CH_4 variations at hourly, synoptic and monthly timescales [7]. As studied by Bacastow et al. [8] in fact, changes in atmospheric CO_2 have been observed in that corresponds to the El Niño's variations. Likewise, combining the satellite data with field data on soil respiration and a global map of net primary productivity, how it has been studied to Fung et al. [10], it was possible to obtain the seasonal exchange of CO_2 between the atmosphere and the terrestrial biosphere. On the other hand, as studied in McGrath-Spangler et al.[11] variation in PBl depth has a significant impact on tracer transport, specifically of CO_2 and CO. In fact, dilution of CO from biomass emissions from the depth of the PBL results in changes in surface concentrations. Although lower, for CO_2 changes, are measured in the temporal average and evident at high latitudes[11].

However, it is possible to carry out a quantitative analysis by analyzing the evolution of spatial-temporal fluctuations in the concentration data series in

such a way as to detect possible correlations with both global but also local phenomena so that it is possible to understand how these systems evolve at different spatial-temporal scales but also how they affect the climate and vice versa. In general, dynamical systems in nature, including GHG tracers and atmospheric quantities, i.e., systems that change with time, obey non-linear laws [12], which generate non-stationary appreciable from a well-determined trend-like behavior[13], as well as exhibiting non-linear fluctuations [14]. Unlike a data time series, that obeys the laws of randomness, where the factors affecting the time series, turn out to consist of a uniformly random distribution, a data series that does not obey regularity and behaves non-uniformly has stochastic characteristics that allow the data in the series to be analyses in detail, going into both graphic and analytical detail. Conventional mathematical and statistical theories focus on linear systems, and the identification of non-linear fluctuations was possible only after the studies conducted in the 70s by Mandelbrot [15] concerning the universal symmetry of self-similarity. i.e. the fractal geometry underlying irregular fluctuations in space and time[16].

Fractal geometry describes objects or processes, which may be non-integer dimension and are usually defined by recursive procedures and enjoy certain scaling properties. In general, a fractal object is related to the Hausdorff dimension, which is the statistical quantity that gives an indication of how complete a fractal appears to fill the space topological space. Representations of a fractal object at different scales exhibit structural similarities, i.e., by zoomed with an appropriate scale factor an however small portion of the object, structural features that reproduce those of the unzoomed object, are manifested. Hence, this property defines the self-similarity or scale invariance of fractals.

However, to identify a time series as a fractal means being able to establish information at different time scales, defining scaling properties. In general, many time series referred to measurements of physical processes, are not fractal only but multi-fractal in nature. In general, a fractal object is defined by a power law dependent on an exponent: the Hurst coefficient (H) [17]. A multifractational object is such that a single H coefficient is not sufficient to describe its dynamic, and thus the scaling properties on different time scale. On the other hand, it is necessary to define a set of H coefficients for a complete characterization of scaling properties[18].

Several studies have been conducted through fractal analysis, applying different methodologies, on the time series of GHG tracers concentrations [19], [20], [21], [22] in which the properties of self-similarity and persistence were high-

lighted, or in Varotsos et al. [23], which was seen to show that fluctuations in the concentrations of CO_2 recorder to Mauna Loa (MLO) exhibit strong long-range correlations which signifies that the fluctuations in CO_2 concentrations, from small time intervals to larger ones (up to 11 years) are positively correlated in a power-law fashion[23]. The presence of long-range correlations in air pollutant concentrations has been attributed to self-organized criticality [24], non-linear interactions and aggregation [25], multiplicative cascade process [26]. The self-organized pollutant concentration store, the material for some time and release it once a certain threshold or critical level is reached[27]. However, the complex dynamics of GHGs evolve depends on multiple factors that inevitably influence their fluctuations and hence their scaling properties. The simultaneous non-linear interaction between sinks and sources in the atmosphere means that the temporal distribution of concentrations are complex in nature, as they act in different ways over the course of seasons and years. An example is given by the temporal distribution of CO_2 which is governed both by anthropogenic phenomena, in which the constant increase of concentrations influences the climate system on regional and global scales, but also by natural phenomena including the photosynthesis-respiration process, the variation of PBL height [28] and by chemical reactions occurring in the atmosphere.

Analysing the distribution of GHG tracers involves then a careful analysis not only of fractal (or multifractal) type, but also concerning the link that exists between the scale properties and the environmental agents that drive the dynamics. However, in the scientific context of the application of fractal analysis on the study of scaling properties, it is intuitive to understand how analysing high frequency sampled time series is important to understand how certain characteristics evolve on an intra-day scale. Analysing and understanding what are the scaling properties of systems involving the atmosphere and thus the climate system in general is of fundamental importance as it helps in the development and implementation of new methodologies in climate-atmospheric models. The meteorological variables that influence pollutant concentrations, and in this case GHG tracers, they vary on all scales up to scales comparable with small fluid scales, that is, to the Kolmogorov microscale.[29]. Although the models involved in defining climate conditions over the years have been improved to have better and better spatio-temporal resolutions, however there are a set of transport-dependent processes, called sub-grid processes, that occur at scales smaller than the model resolution. Because these processes affect the composition of the atmosphere on a larger scale they must be parameterized, and these

parametrizations can be based on empirical information from atmospheric observations or simplified mathematical models[29]. Therefore, defining the scaling properties of pollutant concentrations on a small time scale, significantly improves the parametrization of these processes by improving the quality of future predictions.

This work is based on the analysis of intra-day scaling properties and multifractal dynamics of the temporal distributions of CO_2, CH_4, and CO recorders at the Monte Curcio Observatory (MCU). The characterization of the fast and slow components that constitute the daily sub-intervals of the GHG tracers is the basis of this work. Following the analysis of the variance of the individual Intrinsic mode functions (IMFs), extracted through the Empirical mode decomposition as a function of time periods, it is possible shows different behavior of variance as a function of the chosen time scale. The analysis of the two principal components was performed using various methodologies including Detrendend Flucutations Analysis (DFA) [30] or Structure function analysis [31] and through IMF scaling analysis [32]. This work is divided into an initial chapter in which the main methods of analysis applied on synthetic data are presented. In the second chapter a description of the data used will be made as well as a qualitative description of the periodicity of the diurnal, seasonal and synoptic cycles of the GHG tracers in addition to defining the EVI/NDVI indices, through the analysis of the maps provided by the MODIS satellite [33] and the PBL height from ERA5[34]. In the third and final chapter will be presented the results obtained, compared with those in literature, through the application of methodology used, in addition to defining the multifractal properties of GHG tracers. Also, in order to corroborate the analysis performed on MCU data, all the studies has been repeated on data collected to Mauna Loa observatory (MLO).

Chapter 2

Adaptive data analysis and signal decomposition techniques for complex datasets

In this section will be discussed the main methods used in this thesis work, namely the Empirical Mode Decomposition (EMD), Detrended Fluctuations Analysis (DFA) and Mutual information (MI) with the aim of defining their characteristics and why they are used in the study of the case in examination. In addition to the description alone, results obtained from the application of these methods on synthetic data will be presented.

2.1 Empirical mode decomposition

During the last decades several decomposition methodologies have been implemented, such as Fourier-based techniques, wavelet transforms [35] to investigate the scale variability of natural process. The implementation of these methods, which require a priori fixed decomposition basis, also satisfying the mathematical requirement of completeness, formed by linearly independent functions, or linear independent eigenvectors, allow to obtain oscillating modes of the analysed time series.

However, the non-linearity and non-stationarity of natural phenomena doesn't always succeed in guaranteeing these criteria. To reduce these mathematical requirements, an empirical method of analysis has been proposed, the Empirical mode decomposition (EMD), developed by N.E. Huang et al.[36] in order to analysed time series independently of their linearity and stationarity [37],[38].

Therefore, analysis using the EMD method, unlike of Fourier and Wavelet analysis which are associated with well-defined frequencies, allows the extraction of local information such as instantaneous frequency[36]. Through the use of local properties, in an adaptive decomposition process, this method allows to write a signal $x(t)$ as the sum of k empirical modes $\phi_j(t)$ with zero mean, so-called Intrinsic Mode Functions (IMFs), plus a residual $r(t)$ according to the following equation

$$x(t) = \sum_{j=1}^{k} \phi_j(t) + r(t). \tag{2.1}$$

where this set of IMFs forms a basis of decomposition with which all the mathematical requirements are empirically satisfied (i.e., completeness and orthogonality). In order for $\phi_j(t)$ to be considered an IMF of $x(t)$ two conditions must be satisfied:

- the number of relative extreme values (local maxima and minima) and the number of points where $\phi_j(t)$ takes on a null value are equal or at most differ by one unit;
- at each time point of $\phi_j(t)$ the mean value of the envelope defined by the local maximum points and the envelope defined by the local minimum points is zero.

The first condition is similar to the traditional narrow band requirements for a stationary Gaussian process. The second condition guarantees that the instantaneous frequency has no unwanted fluctuations induced by asymmetric waveforms. Moreover, for nonstationary data, the local average involves a local time scale that is impossible to define. Therefore, the local average of envelopes defined by local maxima and minima is used to force local symmetry [36] The basic steps of the EMD algorithm are described below [36]:

- the average of signal $x(t)$ is calculated is subtracted from it in such a way as to produce a zero mean signal $x_m(t) = x(t) - \langle x(t) \rangle$;
- Local maximum and local minimum points of the signal $x(t)$ are identified, where $x(t_0)$ is considered a local maximum point if its neighbouring points $x(t_0 + 1)$ and $x(t_0 - 1)$ are both smaller, whereas $x(t_0)$ is considered a local minimum if $x(t_0)$ considered a local minimum point if $x(t_0+1)$ and $x(t_0-1)$ are both larger;
- the maximum and minimum points are connected via a cubic spline to form the upper envelope $e_{max}(t)$, and the lower envelope $e_{min}(t)$;

- the mean envelope $e_1(t) = \frac{e_{max}(t)+e_{min}(t)}{2}$ is calculated which is subtracted from $x_m(t)$ to get $h_1(t) = x_m(t) - e_1(t)$;
- if the above two conditions are verified $h_1(t)$ is the first extrapolated IMF and the process is again performed on the new time series defined as $x_h(t) = x_m(t) - h_1(t)$ until a new IMF is obtained;
- in the case where $h_1(t)$ does not meet the two conditions the sifting process is repeated by considering $h_1(t)$ as a time series, and $h_{11}(t) = h_1(t) - e_{11}(t)$ is generated, where $e_{11}(t)$ is the average of the envelopes of $h_1(t)$;
- when the extrapolation process is over, i.e., when it is not possible to extract more IMFs from $x(t)$, the time series $x(t)$ can be written as eq.2.1, in which the residual $r(t)$ is a function that does not oscillate in time[36].

This sifting procedure is repeated m times until $h_{1m}(t)$ does not satisfy the conditions from before. Mathematically, the number of sifting process is stopped when the number of iterations $n \to \infty$, but numerically there are different stopping methodologies. One of the widely utilized criteria, which is the one used in this work, is the one based on 3 threshold parameters α, θ_1 and θ_2 set to $\alpha = 0.005$, $\theta_1 = 0.05$ and $\theta_2 = 10\theta_1$. Since the evaluation of how small the mean amplitude is must be carried out, with respect to the amplitude of the corresponding mode, in order not to recur in an over-iteration and over-decomposition, with this criterion small fluctuations of the average are guaranteed, taking into account large local variations [39]. Also, this criterion, allows the extraction of a finite number of modes which is equal to $log_2(N)+1$ where N is the length of the analysed signal. By defying a standard deviation $\sigma(t) = |\frac{2h_{1m}(t)}{e_{max}(t)-e_{min}(t)}|$, the sifting process is stopped when $\sigma(t) < \theta_1$ for a fraction $1-\alpha$ of the total duration and $\sigma(t) < \theta_2$ for the remaining fraction. The other criterion uses the standard deviation σ between two consecutive steps for the stop procedure, which is defined as

$$\sigma = \sum_{n=0}^{N} \frac{[h_{1(m-1)}(t_n) - h_{1m}(t_n)]}{h^2_{1(m-1)}(t_n)} \tag{2.2}$$

where the process stops when the σ is less than a typical value on the order of $\sigma_{thresh} \approx 0.2, 0.3$.[36].

The EMD method, as well as the advantage of being easy to apply on a wide type of signals of which neither linearity nor stationarity is required, also has some disadvantages as discussed and studied by Rato et al. [40]. One of the steps that is considered critical by Rato et al. [40] is the identification of the extremes

since most of the analysed signals are of a discrete nature. In fact, it is possible that some of the extremes of the continuous signal fall between two sampled points and thus are not correctly identified. The solution to this problem was proposed by Rilling et al. [39] that who proposes to oversample the signal.

In general the cubic spline is used to interpolated the extremes of the envelopes, because other types of interpolation (linear or polynomial) tend to increase the required number of sifting iterations and to "over-decompose" signals by spreading out their components over adjacent modes[39]. In addition to not being an unambiguous stopping procedure, as discussed above, another disadvantage is how the first and last points of the signal are considered. These in fact can either be considered at the same time both minimum and maximum points, and this forces all IMFs to have zero value in those points, or they can be considered maximum or minimum points depending on the relative position of the adjacent point.

But the main problem of the EMD method is the possible occurrence of " mode mixing", that is the mixing of portions of signals from two consecutive IMFs. This mixing of frequencies ω can be due both to the presence of noise and to the physical phenomenon of intermittence that characterizes some types of natural processes. This phenomenon involves an over decomposition of the signal that leads to the extraction of a greater number of IMFs from the signal than the real oscillatory modes that compose it. Thus, one or more oscillatory modes are shared among several IMFs, and this compromises reliability in EMD-based signal monitoring[41]. In the next section will be displayed how this problem affects the IMFs extracted from three different signal types.

2.2 EMD description of fractal time series

In order to better understand the principle of operation of the EMD method is useful to present an illustrative example on four different types of dataset as can be seen in Fig.2.1.

Time series generated by many complex systems in nature, such as air pollutant concentrations, show fluctuations on different time scales and/or wide distributions of values. These fluctuations generate periodic or quasi-periodic behaviours of time series, which, however, are generated by phenomena that have one or more characteristic frequencies or frequency bands. Then the fluctuations extend over different time scales so that the dynamics can be characterized by scaling laws which are valid in a given range of time scales or frequencies.

Such dynamics are usually denoted as *noises*, $fractal$ or $multifractal$. The $fractal$ concept was first introduced by Benoit B. Mandelbrot [42, 43], which included the approaches of H.E. Hurst regarding hydrological systems [17]. Fractals are generally considered to be self-similar objects, implying that the object is similar to one of its own zoomed parts. Mathematically given an object or in the specific case a time series $x(t)$, this is called self-similar if the scaling relation $x(t) \to a^H x(at)$ is valid for any arbitrary value H. Thus, the fractal properties, of a generic time series can be defined usually by a global, time-independent parameter H, know as Hurst exponent [17], which is linked to the level of fluctuations (amplitude of fluctuations) observed in the data. On the other hand, certain physical phenomena can not be described by such global parameter, therefore the local fractal properties are generally related to a time-dependent Hurst exponents [44], or to a probability parameter p [45] which is related to the emergence of the various local phenomena whose superposition define the macroscopic phenomena under study. Such particular kind of fractal objects are multi-fractal.

In fig.2.1 are reported four examples of the various fractal objects described above: a $Fractional\ Gaussian\ noise$ (Fgn) (first row left panel), for three different values of H, constructed by using circulant embedding [46], a $Fractional\ Brownian\ Motion$ (Fbm) (first row right panel), a $multifractal$ (second row left panel) generated through p-model[45] and a $Multifractional\ Brownian\ motion$ (Mbm) (second row right panel) generated with three different time-dependent Hurst $H(t)$ [47].

The fractional Brownian motions Fbm, which represents the most common fractal object, is defined as a continuous Gaussian process $X_H(t)$ with dependent increments with the following properties:

- has stationary increments $X_H(t) - X_H(s) \sim X_H(t-s)$;
- the expectation value $E[X_H(t)] = 0$;
- the covariance function is $E[X_H(t)X_H(s)] = \frac{1}{2}(|t|^{2H} + |s|^{2H} - |t-s|^{2H})$
- is self-similar $X_H(at) \sim |a|^H X_H(t)$.

An Fgn is defined as the increments of an Fbm, i.e. $X_k = X_H(k+1) - X_H(k)$, for which the increments are independent represented in fig.2.1.
For an fbm the coefficient H takes on values $1 < H < 0$, for which three different cases are distinguished:

- $H = \frac{1}{2}$ corresponds to the classic Brownian Motion;

- $H > 0.5$ indicates that increments are positively correlated;
- $H < 0.5$ indicates that increases are negatively correlated;

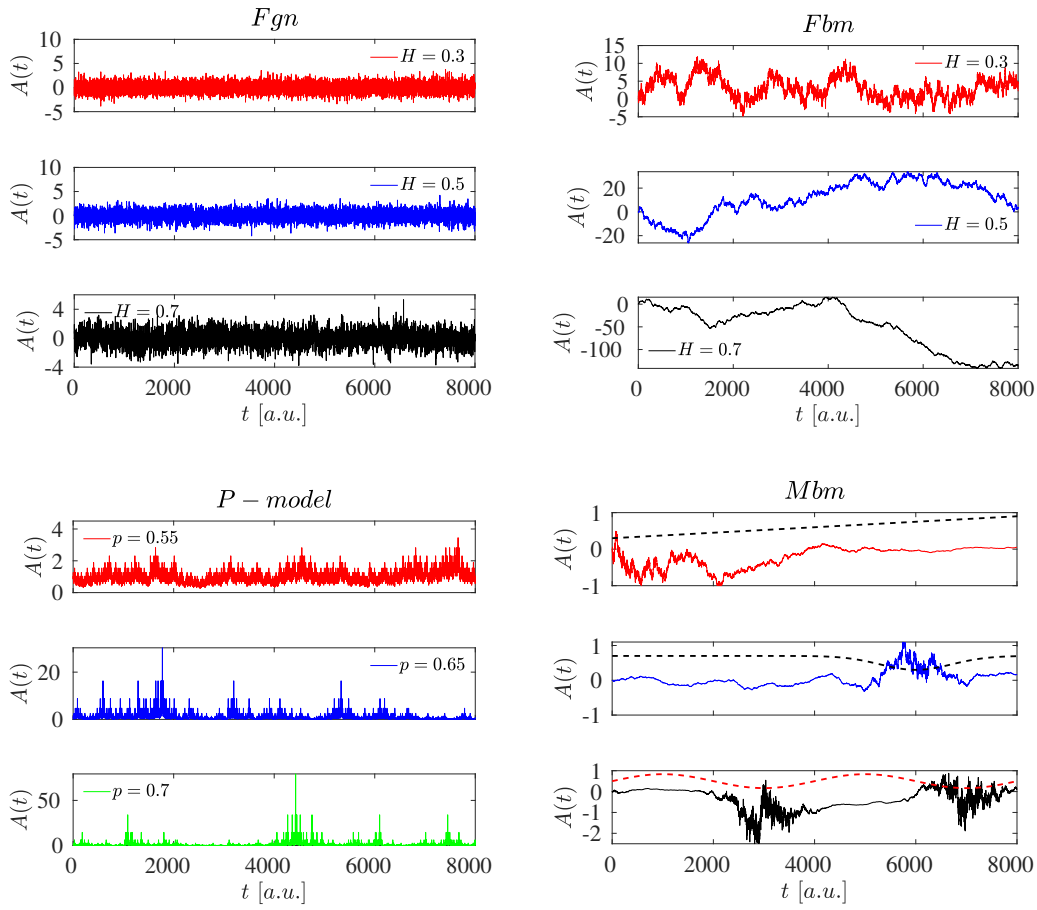

Figure 2.1:
First row: Fgn (left) and Fbm (right) time series generated with three different Hurst coefficient values $H = 0.3$ (red line), $H = 0.6$ (blue line) and $H = 0.7$ (green line) respectively. **Second row**: p-model (left) time series with probabilities values $p = 0.55$ (red line), $p = 0.6$ (blue line) and $p = 0.65$ (green line) respectively. Plot of Mbm generated with a linear $H(t)$ (red line), hyperbolic tangent $H(t)$ (blue line) and sinusoidal $H(t)$ (black line).

Multifractal Brownian motion (Mbm), introduced by Peltier and Lévy Véhel [44] is an extension of Fbm, in which the stationary nature of the process is dropped which allows the H coefficient to change over time. The Mbm represented in fig.2.1 (down right panel), are constructed considering three different time-dependent $H(t)$: linear $H(t)$, hyperbolic tangent $H(t)$ and sinusoidal $H(t)$.

The p-model depicts the energy cascading process in the inertial range of a fully developed turbulence for the dissipation field, which is based on the generalized two–scale Cantor set[45]. Energy distribution occurs at each subsequent

level (referred to as a generation) through binary fragmentation with probabilities p_1 and p_2, where in general p_2 = 1- p_1, among the fragments of length $l1$ and $l2$, or in other words, the energy distributed equally in the succeeding structures. The generation of time series through this methodology is intermittent in nature, which exhibit scale behaviours that cannot be defined by a single exponent.

Natural phenomena, given their non-stationarity, do not exhibit a single scaling behaviour. In fact, in many cases multiple scaling exponents are required for a complete description of the phenomena generating multifractal of multifractional object. Multifractality in the time series may be due to two different types of situations[48]. The first is given by a broad probability distribution for the values in the series, e.g., a Levy distribution. The second is due to different long-term correlations of small and large fluctuations [48], and in this case the probability density function of the values can be a regular distribution with finite moments, e.g., a Gaussian distribution[48].

The simplest type of multifractal analysis is based on the standard multifractal partition function formalism, which was developed for multifractal characterization of normalized and stationary time series[49],[50]. This formalism, however, when applied to non-stationary time series does not give correct results because they are affected by decreasing or increasing behaviour, or cannot be normalized[51]. Thus, an improved multifractal formalism, the wavelet transform modulus maxima (WTMM) method[52], was developed in the early 1990s. This method is based on wavelet analysis and consists of plotting the lines of maxima in the continuous wavelet transform on all scales. On the other hand, the singularity spectrum is directly determined from the scaling behaviour of partition functions that are defined from the wavelet transform modulus maxima[52]. It should be pointed that, in this work, however, an alternative method has been used in which the modulus maxima procedure is not required but which is based on a generalization of the DFA method that does not involve many programming changes of the conventional DFA method. This method is called Multifractal Detrended Fluctuation Analysis (MFDFA) whose ability is to detect long-term correlations in non-stationary time series.

Fig.2.2 shows the IMFs of the three datasets in Fig.2.1 analysed in which, for simplicity only two of the 13 IMFs extracted for in the previous section the number of IMFs extracted is equal to $log_2(N) + 1$ and being that the length of the datasets is 2^{13} the IMFs extracted are 14. The IMFs extracted in all three examples have a period that increases going from the first to the last IMFs, in which it is possible to see that the residual is zero.

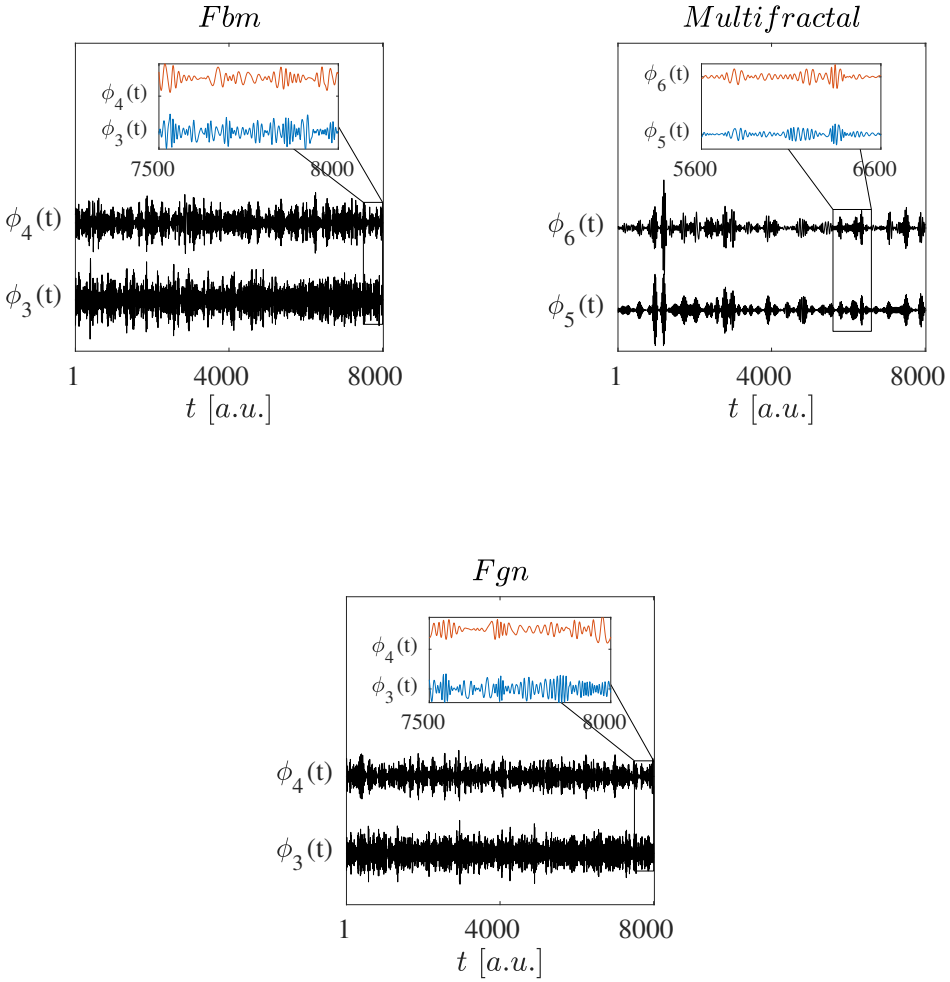

Figure 2.2:
IMFs extracts from the *Fbm* (left panel), $P-model$ (right panel) and *Fgn* (bottom panel) datasets respectively, in which only two consecutive IMFs are shown to improve readability. The graphs within each figure represent zoomed portions of the signal where the mode mixing problem is present.

However, as it is possible to see from the zooms made in the panels of Fig.2.2 there is the presence of the mode mixing problem previously presented where, in fact, there is mixing of frequencies in different temporal intervals between the two consecutive IMFs. The mode mixing is a problem that must be taken into account if you want to study independently the single IMFs. However, in this thesis work will not be taken into account, as will be seen later, will be considered a method for the construction of two components, fast and slow, of the datasets analysed in which the mode mixing does not create any problem

because the IMF extracted will be summed.

Another aspect of applying the EMD method is that if the analysed dataset has certain characteristics, such as fractal time series, fractional Gaussian noise, noise time series or others, it acts intrinsically as a dyadic filter bank [37, 53, 54]. Each IMF captures a narrow spectral band in frequency space [55],[56], [57] and their superposition behave as $M(w) \equiv Max[\phi_j(\omega)] \sim \omega^{-\beta}$ where β is the coefficient which defines the slope of power spectral density. This feature of the EMD method is shown in Fig.2.3, in which the spectra of the three datasets are compared with the spectra of the IMFs separately. As can be seen, the β values extrapolated through the application of the law described above fit the respective spectra of the three datasets well. Note that in the panels of Fig.2.3 only odd ϕ_j are shown to improve readability.

One feature which can be noticed by looking at the β values of the three datasets is that of the Fgn. In fact, one of the characteristics of this type of dataset is to have a spectrum with zero slope, i.e. with $\beta = 0$. This is related to the value of the Hurst coefficient H, which will be discussed in more detail in the next section. This coefficient can be calculated by different methodologies, including one methodology that uses specifically the EMD method and thus the IMFs. In fact, after the IMFs are extracted, the coefficient H can be obtained from the relation linking the variance V_j of the j-th ϕ_j with its characteristic period T_j [32],[58], i.e. via $V_j \propto T_j^{2H}$. In fig.2.4, log-plots of variance as a function of characteristic period T_j for Fng with ($H = 0.7$), Fbm ($H = 0.3$), Mbm and $p - model$ ($p = 0.6$) are shown. The decreasing behaviour of V_j indicates precisely that the signal is an Fgn [37], as does the increasing trend of V_j of the Fbm [32]. However, the behaviour of V_j of the first two modes extracted from the decomposition of the fbm is decreasing since, by construction, the first two EMD modes are mostly noise dominated. Since the Mbm is not defined by a single value of H the behaviour of V_j shows two different scaling ranges in which one can appreciate two different scaling laws (exponents). In particular, for such dataset an Heavyside temporal step of the form is: $H(t) = 0.3$ if $t \leq 4000$, and $H(t) = 0.6$ for $t > 4000$.

In the last panel the behaviour of V_j as a function of period T_j, for the $p - model$, presents a continuos modulation, with multiple scaling ranges, due to the vary local nature of the process.

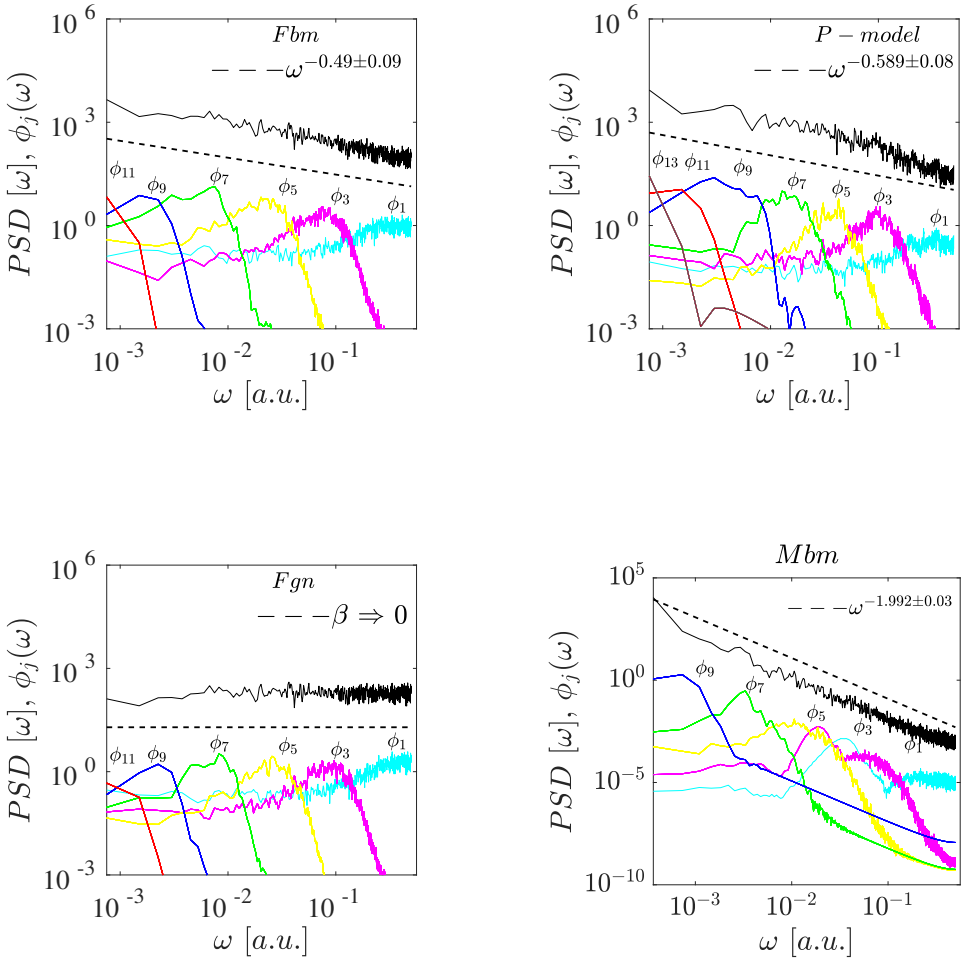

Figure 2.3:
Comparison of Fourier spectral density (**black lines**) for the Fbm (upper left panel), $p-model$ (upper right panel), Fgn (down left panel) and Mbm (down right panel) with the Fourier power spectrum of different ϕ_j, as a function of frequency ω. The dashed black lines indicated the relations $\omega^{-0.49\pm0.09}$, $\omega^{-0.589\pm0.08}$, $\beta = 0$ and $\omega^{-1,992\pm0.03}$, which fits the PSD.

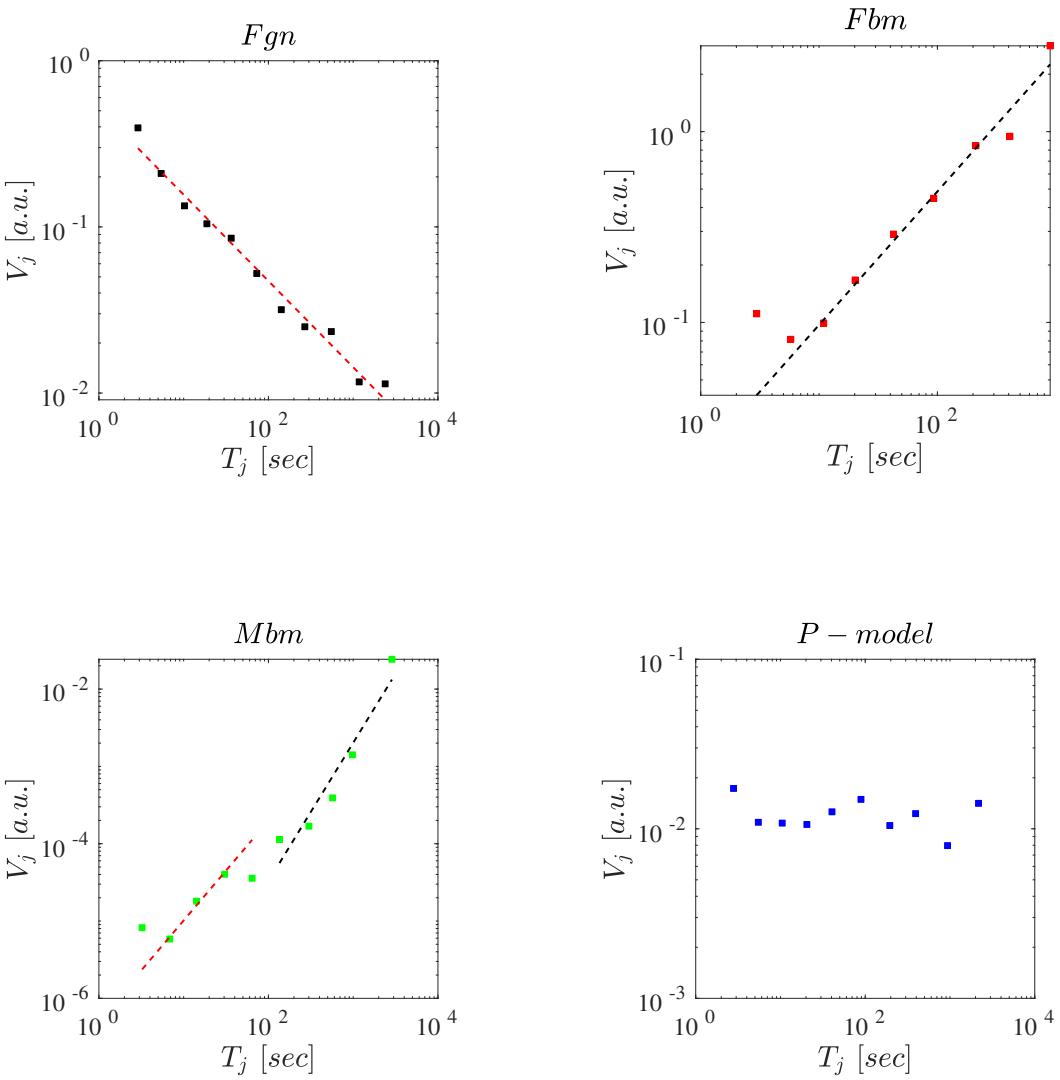

Figure 2.4:
Log-plots of variance V_j in function of T_j for Fgn (black), Fbm (red), Mbm (green) and $p-model$ (blue). For a Fgn the values of V_j are decreasing and are fit by the power law with slope:.... For Fbm the V_j as a function of T_j is increasing, except for the first two modes, and is fit by a power law with slope:.... The Mmb has two different ranges of scaling which are fit by a power law with slope:. For the $p-model$ we appreciate three ranges of scaling and the slope of dashed lines are:....

2.3 Detrended Fluctuation Analysis and multifractal extension

The Detrended fluctuations analysis (DFA) technique, developed by Peng et al.[30], is an important method to detect long-range correlations in time series.

The DFA method represents a evolution version of classical Fluctuation analysis (FA), where the difference is basically given by an additional detrending (linear, polynomial, cubic) term in DFA for applications to non-stationary time series.

In addition to the detection of long-range correlations, DFA has been widely used to determine fractal scaling properties, such as self-similarity and scale invariance in several hot spots of science and in particular in the study of the complex dynamics of pollutant concentrations in air [19],[23],[20], [59],[60],[61],[62].

As with the FA method, given a dataset $x(t)$, first the global profile is computed, i.e., the partial sum $y(j) = \sum_{t=1}^{j} x(t)$, and then the profile is divided into non-overlapping boxes of equal length ℓ. In each box the data is fitted by a polynomial trend y_{fit}^{m} by least-square fitting and then subtracted from the original profile. The degree of the polynomial y_{fit}^{m} can be varied in order to eliminate constant (m = 0), linear (m = 1), quadratic (m = 2) or higher order trends of the profile function [63]. The variance of the detrended profile in each box yields the mean square fluctuations according to the following relationship:

$$F(\ell) = \sqrt{\left(\frac{1}{N} \sum_{i=1}^{N} \left[y(i) - y_{fit}^{m}(i) \right]^2 \right)} \tag{2.3}$$

The calculation is repeated for all boxes size so as to obtain the relationship between $F(\ell)$ and ℓ. If the relation between $F(\ell)$ and ℓ is a power-law then this indicate a presence of scaling: $F(\ell) \sim \ell^{\gamma}$. The parameter γ is called scaling exponent or correlation exponent and represent the correlation properties of the signal and it is so called generalized Hurst exponent.

2.3.1 Multifractal detrended fluctuation analysis

As explained above, many natural phenomena do not present a simple single-fractal scaling that cannot be explained by a single scaling exponent γ. This behavior can be appreciated by the different scaling according to the chosen scale of fluctuation function $F(\ell)$. In these cases multiple scaling exponents are needed for a complete description of scaling behaviour, hence the need for multifractal time series analysis. The basic steps of the Multifractal detrended fluctuation analysis method are 5 of which the first 3 are identical to those of the DFA which for completeness in the description of the method are reported below.

Given a time series $x(t)$ of length N we have:

- **Step1**: the profile $Y(i)$ is defined, i.e. the average is first subtracted from $x(t)$ and then integrated

$$Y(i) = \sum_{j=1}^{i} [x_j(t) - \langle x(t) \rangle], \qquad i = 1, ..., N \tag{2.4}$$

- **Step2**: Since the length N of the series is often not a multiple of the considered time scale ℓ, a short part at the end of the profile may be disregarded. In order not to neglect this part, the same procedure is repeated starting from the opposite end obtaining overall $2N_\ell$ segments.

- **Step3**: Calculate the variance

$$V(\ell, \nu) \equiv \frac{1}{\ell} \sum_{i=1}^{\ell} \{Y[(\nu - 1)\ell + 1] - y_\nu(i)\}^2 \quad \nu = 1, .., N_\ell. \tag{2.5}$$

  and

$$V(\ell, \nu) \equiv \frac{1}{\ell} \sum_{i=1}^{s} \{Y[N - (\nu - N_\ell)\ell + i] - y_\nu(i)\}^2 \quad \nu = N_\ell + 1, .., 2N_\ell. \tag{2.6}$$

  $y_\nu(i)$ is the polynomial fitting in the different segments ν. Linear, quadratic, cubic or higher order polynomials can be used in the fitting procedure (conventionally called DFA1, DFA2, DFA3, . .)[30]. Because time series detrending is done by subtracting polynomial fits from the profile, DFAs of different order differ in their ability to detrend trends in the series. In (MF-)DFAm [$m-th$ order (MF-)DFA] trends of order m in the profile (or, equivalently, of order $m-1$ in the original series) are eliminated. Then a comparison of the results for different orders of DFA allows one to estimate the type of polynomial trend in the time series [64],[59].

- **Step4**: Average over all segments to obtain the q-th order fluctuation function, defined as:

$$F_q(\ell) = \left\{ \frac{1}{2N_\ell} \sum_{i=1}^{2N_\ell} [V(\ell, \nu)^{q/2}] \right\}^{1/q}, \tag{2.7}$$

  where the index q can take any real value except zero. For $q = 2$ the standard DFA procedure is retrieved. We are interested in how the generalized

q dependent fluctuation functions $F_q(\ell)$ depend on the time scale ℓ for different values of q. Hence, we must repeat steps 2 to 4 for several time scales ℓ. It is apparent that $F_q(\ell)$ will increase with increasing ℓ. Of course, $F_q(\ell)$ depends on the DFA order m. By construction, $F_q(\ell)$ is only defined for $\ell \geq m + 2$.

- **Step5**: Determine the scaling behaviour of the fluctuation functions by analysing log-log plots $F_q(\ell)$ versus ℓ. If the series $x(t)$ are long-range power-law correlated, $F_q(\ell)$ increases, for large values of ℓ, as a power-law,

$$F_q(\ell) \sim \ell^{H(q)}. \tag{2.8}$$

the exponent $H(q)$ may depend on q. For stationary time series, $H(q = 2)$ is identical to the well-known Hurst exponent H [65]. Thus, the function $H(q)$ is called generalized Hurst exponent.

However, the MF-DFA method can only determine positive generalized Hurst exponents $H(q)$, and it already becomes inaccurate for strongly anti-correlated signals when $H(q)$ is close to zero. In such cases, a modified MFDFA technique has to be used. The most simple way to analyse such data is to integrate the time series before the MFDFA procedure. Hence, by replicating the single summation in relation 2.7, which is describing the profile from the original data $x_j(t)$, by a double summation,

$$\tilde{Y}(i) = \sum_{k=1}^{i} [Y(k) - \langle Y \rangle]. \tag{2.9}$$

Following the same procedure described above it can possible determine the fluctuation function $\tilde{F}_q(\ell) \sim \ell^{\tilde{H}(q)} = \ell^{H(q)+1}$. Thus, the scaling behaviour can be accurately determined even for $H(q)$ which are smaller than zero (but larger than -1) for some values of q.

2.3.2 Relation to multifractal formalism

For a stationary, normalized series the multifractal scaling exponents $H(q)$ defined in relation 2.8 are directly related to the scaling exponents $\tau(q)$ defined by the standard partition function-based multifractal formalism as shown below. Now, suppose that the series $x_j(t)$ of length N is stationary and normalized, then the detrending procedure in step 3 of the MFDFA method is not required. Thus, the DFA can be replaced by the standard Fluctuation Analysis (FA),

which is identical to the DFA except for a simplified definition of the variance for each segment ν for $\nu = 1, .., N_\ell$. Step 3 now becomes

$$V_{FA}(\ell, \nu) \equiv [Y(\nu\ell) - Y((\nu - 1)\ell))]^2. \tag{2.10}$$

Inserting this simplified definition into relation (2.7) and using relation 2.8, and for simplicity assuming that the length N of the series is an integer multiple of the scale ℓ, obtaining $N_\ell = N/\ell$ and therefore

$$F_q(\ell) \sim \ell^{qH(q)-1}. \tag{2.11}$$

The term $Y(\nu\ell) - Y((\nu - 1)\ell))$ is nothing but the sum of the values of $x_j(t)$ within each segment ν of size ℓ. In the standard multifractal theory this sum is known as the box probability $p_\ell(\nu)$ of normalized series $x_j(t)$,

$$p_\ell(\nu) \equiv \sum_{j=(\nu-1)\ell+1}^{\nu\ell} x_j(t) = Y(\nu\ell) - Y((\nu - 1)\ell)). \tag{2.12}$$

The scaling exponent $\tau(q)$ is usually defined via the partition function $Z_q(\ell)$

$$Z_q(\ell) = \sum_{\nu=1}^{N/\ell} |p_\ell(\nu)|^q \sim \ell^{\tau(q)} \tag{2.13}$$

where q is a real number. Substituting 2.12 into 2.13 you get an analytic relation which can be compared with Eq(1.11) obtaining

$$\tau(q) = qH(q) - 1. \tag{2.14}$$

where τ_q is called a mass exponent that has a linear relationship with q. Thus, it can possible observe that $H(q)$ defined in relation 2.8 for the MFDFA is directly related to the classical multifractal scaling exponents $\tau(q)$, with $H(q) = qH(q) - 1$. However, the analysis of a multifractal series, besides being characterized by the parameters $\tau(q)$ and $H(q)$, is characterized by another parameter namely the singular spectrum $D_q(\alpha)$. This is related to $H(q)$ through a Legendre transform [64],

$$\alpha_q = \tau'(q) \qquad and \qquad D_q(\alpha) = q\alpha_q - \tau(q) \tag{2.15}$$

where, α_q is the singularity strength or Hölder exponent, while $D_q(\alpha)$ denotes the dimension of the subset of the series that is characterized by α_q. Using

relation 2.14, you can directly relate α_q and $D_q(\alpha)$ to $H(q)$,

$$\alpha_q = H(q) + qH'(q) \qquad and \qquad D_q(\alpha) = q[\alpha_q - H(q)] + 1. \tag{2.16}$$

A Hölder exponent denotes monofractality, while in the multifractal case, the different parts of the structure are characterized by different values of α_q, leading to the existence of the spectrum $D_q(\alpha)$. One of the fundamental aspects that characterizes MDFDA is the dependence of the quantities $H(q)$, $\tau(q)$ and then $D_q(\alpha)$ on q. The parameter q can assume both negative and positive values and this, according to the characteristics of the analysed datasets, characterizes the behaviour of the scales of the quantities of the parameters of MFDFA. Thus, if q is positive, the segments ν with variance $F^2(\ell, \nu)$ large dominate the average $F_q(\ell)$ indicating that for positive q $H(q)$ describes the scaling behaviour of segments with large fluctuations[51]. In contrast, for negative q it is the ν segments with small variance to dominate indicating a that $H(q)$ describes a scaling behaviour of segments with small fluctuation. If $H(q)$ defines constant scaling behaviour, i.e., if it is constant regardless of the values of q, then this indicates that the variance $F^2(\ell, \nu)$ is identical for each segment ν and there is no difference between in the scaling behaviour between segments with large and small fluctuation. This behaviour of $H(q)$ in different cases is obviously also reflected in the behaviour of $\tau(q)$ and $D(\alpha_q)$. In fact, if H_q is constant $\tau(q)$ will have a linear q-dependency on the contrary if $H(q)$ varies with q $\tau(q)$ will have a curved q-dependency. This trend of $\tau(q)$ then defines the trend of the spectrum $D_q(\alpha)$, where in the case where $\tau(q)$ é linear q-dependency α_q, defined as the derivative of $\tau(q)$, does not vary and the spectrum has a small arc. In contrast, the curved q-dependence of $\tau(q)$ defines different values of α_q resulting in a width of the spectrum greater. An illustrative example to understand how these definitions are applied to the study of generic datasets is given below.

2.3.3 Illustrative example

In order to understand the principle of functioning of the MFDFA method, it is useful to present an illustrative example applied to the time series in Fig.2.1. As can be seen from Fig.2.5, the trends of $H(q)$(left panel) and $\tau(q)$(right panel) as a function of q and $D_q(\alpha)$ (bottom panel) as a function of α_q are different for the time series considered. For the time series Fgn and Fbm there is no appreciable variation of the generalized Hurst coefficient $H(q)$ between negative and positive q and this indicates that the two time series do not have periods that are not

large or small fluctuations which results in a constant $H(q)$ independent of q.

In general, each coefficient $H(q)$ depends on $F_q(\ell)$ because it is calculated from the linear regression of the different $F_q(\ell)$. The fact that it is constant comes from its independents from q, and this can be seen from the fact that the $F_q(\ell)$ have the same distance to each other regardless of the distance of the scale ℓ. However, a different behaviour can be seen when considering the multifractal temporal series where the behaviour of $H(q)$ indicates how the distance between $F_q(\ell)$ decreases as q increases, being able therefore to differentiate the various structures of the temporal series according to the value of $H(q)$. The constant behaviour of $H(q)$ for the Fgn and Fbm time series implies a linear q-dependence of τ_q Fig.2.5(right panel) and a curved q-dependence for $p - model$ time series. This behaviour of τ_q leads to an almost constant value of α_q for the Fgn and Fbm time series and a decreasing slope for the $p - model$ time series. The resulting singularity spectra $D_q(\alpha)$ are shown in fig2.5(bottom panel) where, depending on the difference between the maximum and minimum values of α_q, the spectrum can be wider or narrower. Actually, considered that the $H(q = 2)$ values for the Fgn and $p-model$ time series are equal and using only the DFA method, it was not possible to define the differences.

The different width of the singularity spectra $D_q(\alpha)$ can then be used to define the multifractality or monofractality of the datasets. In fact, a larger width, which as mentioned above is related to the scaling behaviour of $H(q)$, defines greater multifractality. In contrast, a small $D_q(\alpha)$ width results from a constant behaviour of $H(q)$ as a function of q and this highlights the monofractality of the dataset. Moreover, the dependence on q of α_q is also and particularly manifest in the form of $D_q(\alpha)$ and hence on its symmetry. The singularity spectra $D_q(\alpha)$ can also have either a left or a right truncation that originates from a levelling of the q-order Hurst exponent for negative or positive q's. The singularity spectra $D_q(\alpha)$, especially for multifractal datasets, will have a long left tail when the time series have a multifractal structure that is insensitive to the local fluctuations with small magnitudes. In contrast, the $D_q(\alpha)$ will have a long right tail when the time series have a multifractal structure that is insensitive to the local fluctuations with large magnitudes.

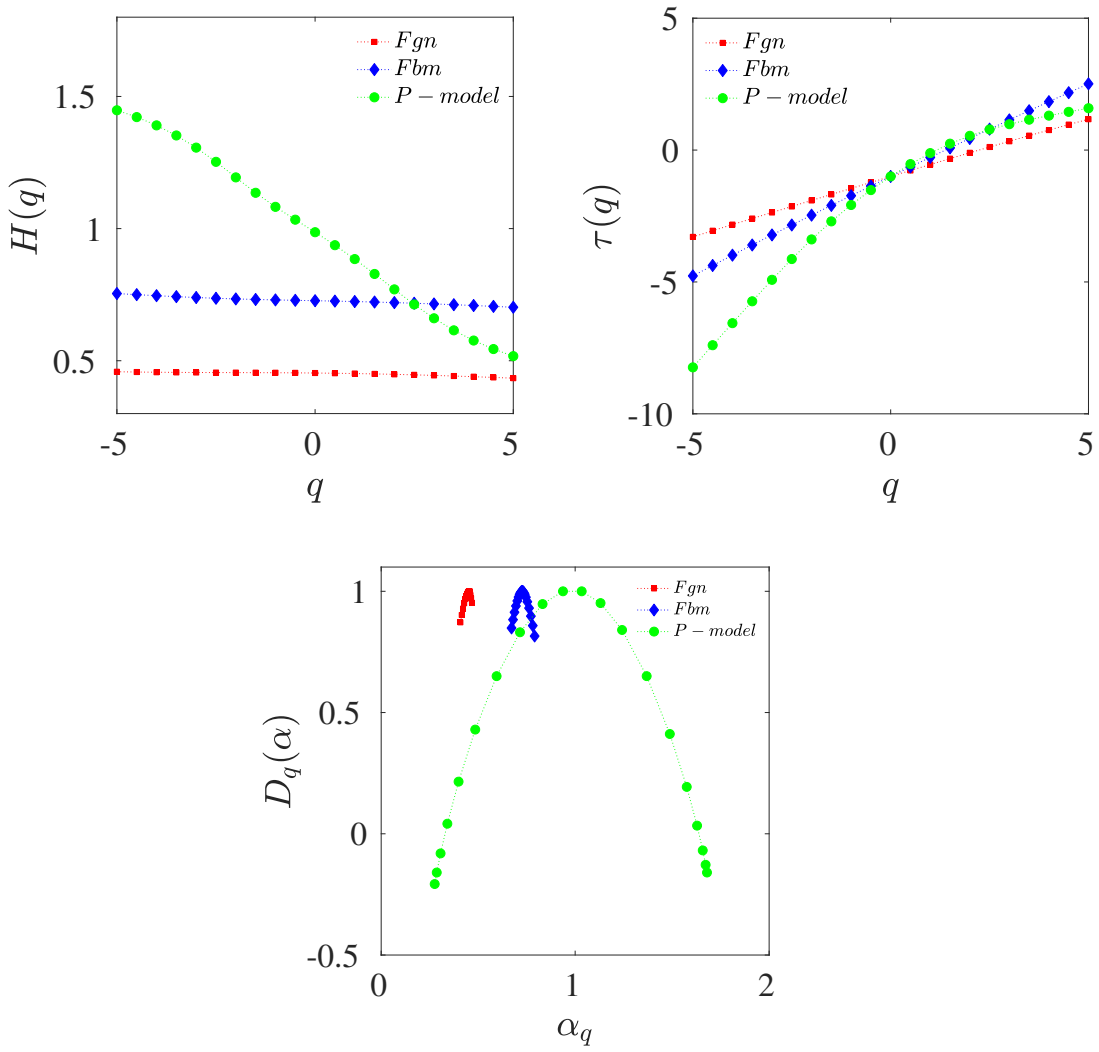

Figure 2.5:
Right panel: Variation of generalized Hurst coefficient $H(q)$ for Fgn(red), Fbm(blue) and $p-model$(green) in function of q. **Right panel**: Variation of q-mass coefficient $\tau(q)$ for Fgn(red), Fbm(blue) and $p-model$(green) in function of q. **Bottom panel**: Singularity spectra $D_q(\alpha)$ for Fgn(red), Fbm(blue) and $p-model$(green) in function of α_q.

2.4 Sharing of mutual information

The concept of Mutual Information was first introduced by Shannon [66] to quantify the information shared by two variables. This means that, taken two strictly independent random variables, the MI value between them will be zero because they do not share any information[67]. In general taken two variables

X and Y, the Mutual information between them is given by relation

$$I(X,Y) = \int_Y \int_X f_{X,Y} log \left(\frac{f_{X,Y}(x,y)}{f_X(x) f_Y(y)} \right) dx\, dy \tag{2.17}$$

where $f_{X,Y}(x,y)$ is the joint probability density function (PDF) for the variables X and Y and $f_X(x)$ and $f_Y(y)$ are the marginal PDF [68].
The application of this methodology in measured data situations requires an approximation of Eq.2.17 through a discretization of the estimator MI. This discretization is performed through three basic steps. In the first step a subdivision of the dataset into fixed-width discrete bins (cells) is made. Then a histogram is created considering the relative frequency of occurrence of samples at each bin [68], and finally is calculated the MI from the histogram. The main problem with this method of calculating the estimator is the limitation of partitioning the data into bins, which is carried out by dividing the data into bins of equal width producing an accumulated error [69].

In order to overcome this issue Darbellay and Vajda [70] considered a partition of the space of the data into a finite number of non-overlapping rectangular cells. This methodology is also the basis of the algorithm used in this thesis work. According to the authors, instead of partitioning the data into cells of fixed width. Initially, data must be organized into a one-cell partition. Then, the cell is partitioned into 2 equiprobable halves. Next, the two resultant subcells must be recursively partitioned. This algorithm estimate the mutual information (MI) by calculating relative frequencies on appropriate partitions formed in a way that conditional independence is achieved on the cells [70]. The advantage of the estimator of Darbellay and Vajda is that it is adaptive to the data and does not involve a parameter for the binning. It does however involve a parameter for the independence test that can affect the performance of the estimator. However, this estimator has a direct dependence on the length of the signal which determines the roughness of the partitioning. In the abundance of data, the AD estimator reaches a very fine partition that satisfies the independence condition in each cell, so that the total number of cells is very large, such a way the increase of length of time series implies a finer partition.

Chapter 3

Atmospheric greenhouse gases tracer

3.1 The CNR-IIA Atmospheric Climatic-Environmental Observatory

This work is focused on the analysis of the high-frequency time series of CO_2, CH_4 and CO collected during the period 2015 to 2017 at the CNR-IIA Atmospheric Climatic-Environmental Observatory located at Monte Curcio (39.2^o N 16.2^o E). The observatory is about 1780 m above sea level (a.s.l.) located in a strategic position within the Sila National Park in the Calabria region (Fig.3.1). The site is partner of the regional Global Atmosphere program within global atmospheric watch (GAW), established by the World Meteorological Organization (WMO) -a United Nations agency- aimed to systematic long-term monitoring of atmospheric chemical and physical parameters at global and regional scale [71]. The observatory, both due to its elevation and position in the Mediterranean basin far from anthropogenic sources, is particularly able to intercept the influence of adjacent regions and the effects of terrestrial biology.

In order to check and corroborate the results obtained trough the analysis performed on data collected at MCU, the study has been repeated on data collected at the Mauna Loa Observatory (MLO) (19.5^o N 155.6^o W) [72], on the island of Hawaii during the same period. MLO is one of baseline atmospheric monitoring stations operated by the Geophysical Monitoring for Climatic Change (GMCC) program of the National Oceanic and Atmospheric Administration (NOAA) (Fig.3.2). Continuous measurements of atmospheric CO_2, CH_4 and other concentrations have been made at Mauna Loa since 1958 by the Scripps

Institution of Oceanography (SIO) [73]. The long record of atmospheric CO_2 measurements at Mauna Loa is one of the most important data records for studies of the global carbon cycle and CO_2-induced climatic change.

Measurements of CO_2, CH_4 and CO at MCU were collected by using the Picarro model G2401 greenhouse gas concentration analyser that enables simultaneous measurements of CO_2, CH_4, CO with part-per-million (ppm) sensitivity and negligible drift over months of operation. The G2401 also features Picarro's unique algorithms to correct the dilution effect of H_2O vapour and to report dry gas mole fractions of CO_2, CH_4 and CO. The Picarro's measurement technique is based on the Cavity Ring-Down Spectroscopy (CRDS) technology, which is a time-based measurement able to quantify molecules in a cavity through the use of three mirrors. CRDS utilizes the unique infrared absorption spectrum of gas-phase molecules to quantify the concentration of CO_2, CH_4 and CO. Furthermore, Picarro uses a patented high-precision wavelength monitor to maintain the absolute spectral position for the best accuracy in quantifying the peak. The Picarro analyser was placed inside the building with the sampling head positioned at one meter above the station. The sample air is filtered in order to block dusts and insects. The instrument has been set up to collect data with a variable temporal resolution of $\Delta t \leq 1$ sec, due to the quality assurance/quality control (QA/QC) algorithm.

The study of datasets were averaged to a temporal resolution of $\Delta t = 1$ sec. The data collected over the 3 years were divided into monthly intervals and then further divided into daily sub-intervals of length $\mathcal{T}_W \approx 8.6 \times 10^4$ sec. In the first analysis a screening of each sub-intervals was performed. Sub-intervals, in which the gap of data exceeded 25% (approximately 6 hours), were not considered (approximately 1% of the entire dataset). In addition, datasets that had gaps shorter than 6 hours were considered from the first useful value. Finally, for all remaining sub-intervals (less than 6 hour), the gaps were filled by linear interpolation. For a more accurate analysis, the sub-intervals that presented many outliers (5% of total), i.e. and those that presented a standard deviation $\sigma > 5$, even if they were included in the first analysis, were also eliminated.

Figure 3.1: CNR-IIA Atmospheric Climatic-Environmental Observatory on Monte Curcio.

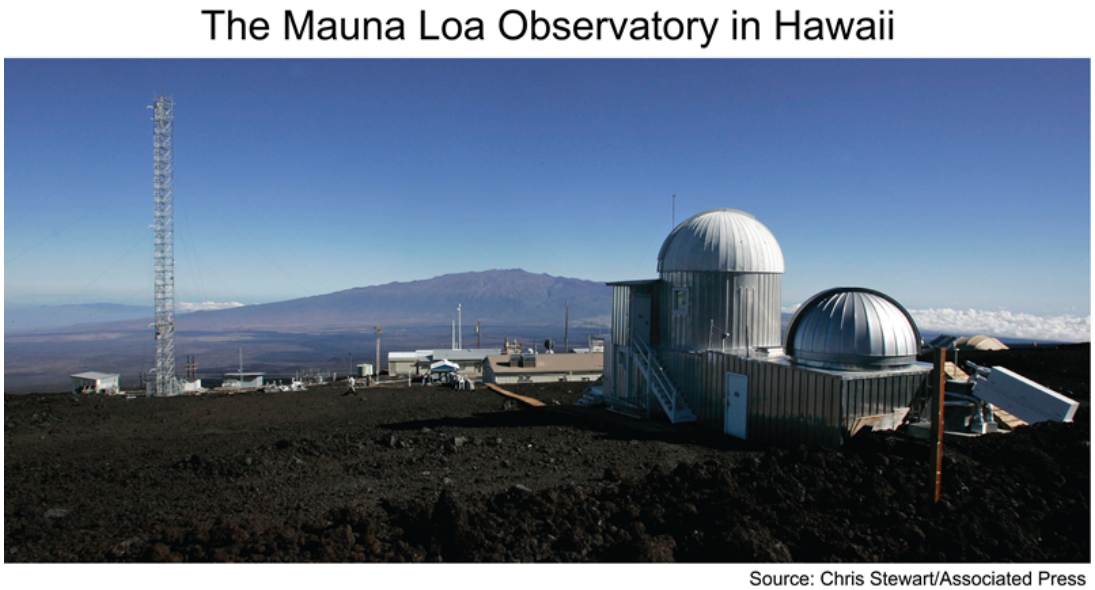

Figure 3.2: The Mauna Loa Observatory on the island of Hawaii.

3.2 Preliminary analysis

In first analysis, the annual averages are considered for a macroscopic description of the dynamics of GHG tracers. In fig.3.3 are reported the monthly mean concentrations for CO_2, CH_4 and CO recorded at Monte Curcio ($\Delta t = 1$ sec resolution). The annual averages and respective standard deviations are shown in Tab.3.1.

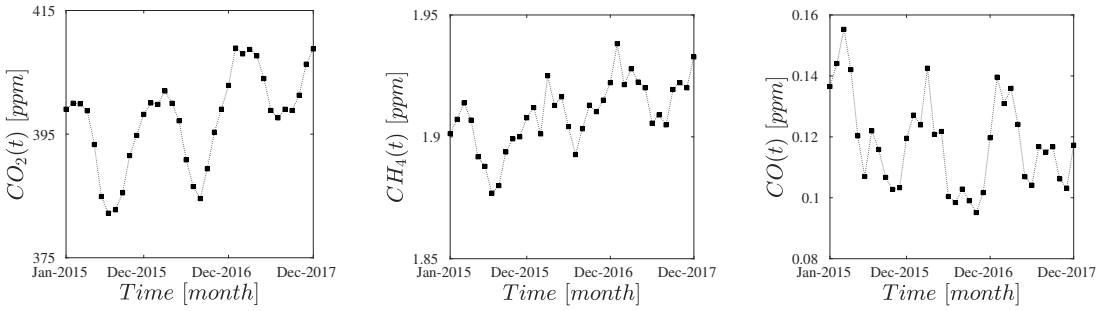

Figure 3.3:
Right panel: Monthly mean variation of CO_2 concentration recorder at Monte Curcio from 2015 to 2017. **Central panel**: Monthly mean variation of CH_4 concentration recorder at Monte Curcio from 2015 to 2017. **Left panel**: Monthly mean variation of CO concentration recorder at Monte Curcio from 2015 to 2017.

Table 3.1: Descriptive statistics of three pollutant concentrations (Unit: ppm).

Statistics	2015			2016			2017		
	CO2	CH4	CO	CO2	CH4	CO	CO2	CH4	CO
Mean	392.25	1.877	0.123	395.60	1.887	0.113	398.44	1.90	0.12
Standard deviation	7.55	0.024	0.027	6.95	0.024	0.02	7.20	0.025	0.04

As can be seen from the monthly variation of the CO_2 values shown in Fig.3.3 and from the annual average values reported in tab.3.1, the values of CO_2 had an increase of 0.7% (2016) and 2% (2017), respectively compared to 2015. An increment of the order of 0.5%, are also recorded for CH_4. As can be seen from fig.3.3 the levels of CO_2, CH_4 and CO are low in the Jun-Sep period and high in Dec-Feb and this defines a seasonal variation of the same. The data collected and presented in fig.3.3 show a temporal variation characterized by a seasonal modulation with a possible increasing behaviour for the CO_2 (left panel) and CH_4 (central panel) and a constant value for the CO (right panel). The increasing values of CO_2 and CH_4 concentrations (also evidence by the annual average values in tab.3.1), are in line with the increment measured at Mauna Loa (fig.3.4).

The fundamental difference in the temporal concentrations, measured at MCU (fig.3.3 left panel), and MLO (fig.3.3 left panel), is the different position (in time) for the monthly maxima and minima. For MCU Jan-Mar is the period of highest concentration of CO_2 and Jun-Aug the period of lowest concentration, on the other hand MLO represents Apr-Jun as the period of maximum concentration and Aug-Oct as the period of minimum concentration. This phase-shifted cycle between the temporal evolution of CO_2 concentrations between the two stations is probably due to the influence of local and global phenomena developing on different temporal and spatial scales, to which the dynamics of CO_2 is connected. In fact, for MLO it has been well demonstrated how the modulation of CO_2 is connected to the Southern Oscillation [8], or with local phenomena such as volcanic emission or from upslope or downslope airflows[74]. Affecting the dynamics of CO_2 are also the different altitude (1800 m.s.l.m MCU vs 4205 m.s.l.m MLO) and latitude and both to the different environment where the two observatories are located. On the other hand, CH_4 does not present any particular differences between MCU fig.3.3 and MLO fig.3.4 in concentration values nor the presence of phase-shifted cycle indicating that the dynamics and cyclicity are similar. This behaviour can be attributed to phenomena on a global scale that influence its dynamics. In fact, because methane has an average lifetime in the atmosphere of about 12 years [75], this implies that methane is nearly conserved during rapid transport from source regions, where dilution due to mixing is limited [76], thus favouring a same dynamic in the temporal evolution of it.
As can be seen in Tab.3.2, where mean and standard deviation are shown, the changes in percentages of CO_2 and CH_4 at MLO reflected those found at MCU.

Table 3.2: Descriptive statistics of CO_2 and CH_4 pollutant concentrations (Unit: ppm) at Mauna Loa

Statistics	2015		2016		2017	
	CO2	CH4	CO2	CH4	CO2	CH4
Mean	400.58	1.85	404.03	1.86	406.40	1.87
Standard deviation	2.24	0.18	2.42	0.19	2.23	0.19

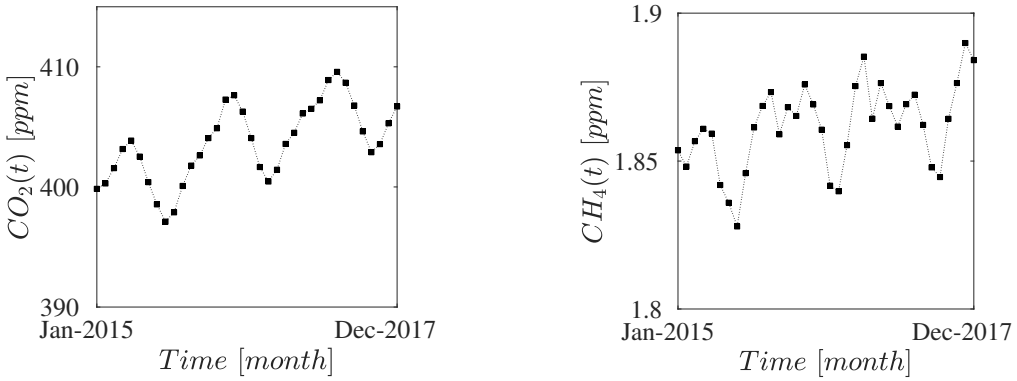

Figure 3.4:
Right panel: Monthly mean variation of CO_2 concentration recorder at Mauna Loa from 2015 to 2017. **Left panel**: Monthly mean variation of CH_4 concentration recorder at Mauna Loa from 2015 to 2017.

3.3 Diurnal and seasonal variations of CO_2, CH_4 and CO

Multiple processes regulate the fast and slow behaviour, seasonality and dynamics of GHG concentrations in the atmosphere: emissions from anthropogenic sources, biogenic (photosynthesis-respiration process [77]), non-biological (emission from volcanoes), chemical reactions, processes of transposition through the phenomenon of turbulent diffusion, transport due to wind flow, deposition, variation of the height of planetary boundary layer (PBL), are all complex processes that could non-linearly interact in affecting the temporal evolution of GHG tracers concentration. Understanding the nature of such variations, e.g. in terms of stochastic dynamic or fractal properties, is important in order to highlight their dependence with the principal atmospheric drivers. So that this information can later be used to improve sub-grid parametrization in atmospheric models.

All three GHG possess a temporal variation spanning diurnal, seasonal, and synoptic scale[78],[79], and these cycles are different among them, i.e difference in amplitude and in frequency, due to their different average lifetime in the atmosphere, and different sources and different sinks. In fig.3.5 are shown the temporal distribution of CO_2 (left panel), CH_4 (central panel) and CO (right panel) of Monte Curcio referred to 1-2 June 2016 depicting the classical diurnal cycle for the three GHG tracers.

The temporal behaviour of CO_2 concentrations is due to different process, which evolve on different time scales, such as anthropogenic activities, decomposition

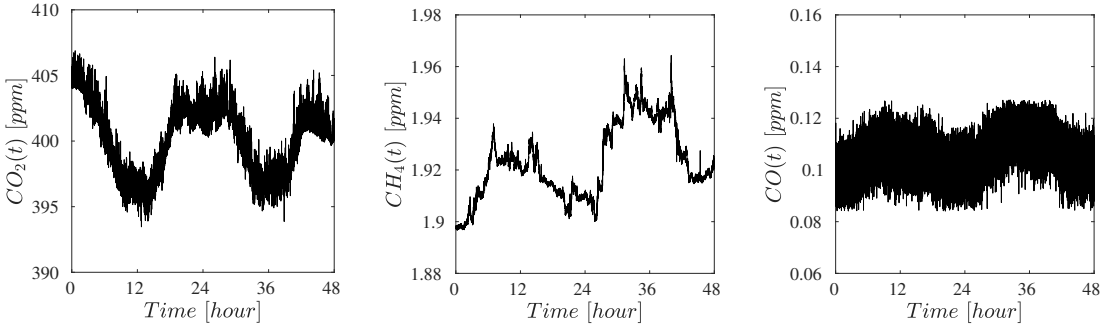

Figure 3.5:
Plot of diurnal concentrations on 1-2 June 2016 of CO_2 (left panel), CH_4 (central panel) and CO (right panel) measured at Monte Curcio.

of organic debris, ocean evaporation, variation of PBL height and even more important by the process of variation of GPP (gross primary production or photosynthetic uptake) and RE (ecosystem respiration) in the year[28],[77],[80], [81],[82]. This set of processes can interact and cause the diurnal variability that characterizes the CO_2 dynamics. During the day there is the presence of a double maximum respectively between 00:00-03:00 LT (local time) and between 21:00-24:00 LT and a minimum between 11:00-13:00 LT fig.3.5 (left panel). This, in fact, is closely related to the photosynthesis-respiration process, in which during the day the vegetation through the chemical reaction $6CO_2 + 12H_2O + E \rightarrow C_6H_{12}O_6 + 6O_2 + 6H_2O$, where E is solar energy, photosynthesises the CO_2 lowering its concentration in the atmosphere. As this reaction uses solar energy it is obvious that in the hours of greatest light exposure this process is more efficient and therefore more CO_2 is transformed forming the minimum of the diurnal cycle that is observed. In contrast, during the night and therefore in the hours of lower light exposure, the vegetation through the process of respiration, governed by the chemical relationship $C_6H_{12}O_6 + 6O_2 + 6H_2O \rightarrow 6CO_2 + 12H_2O + E_c$, where E_c is the chemical energy released, releases CO_2 in the atmosphere which increases the concentration forming the two maxima of the diurnal cycle that are observed.

This process is obviously present during the whole year, but it affects in a different way the CO_2 concentrations according to the months, because the duration of days and nights changes during the year and with it the duration of the process. In fig.3.6 (left panel) the diurnal mean cycle of CO_2 concentrations of the four different seasons is shown. As can be seen the amplitudes of the cycles are different where summer is characterized by a greater cycle amplitude than winter[83]. In fact in winter a marked diurnal cycle is not appreciable, probably

due both to a slightly increased respiration during the day and by an accumulation of CO_2 at the observatory transported by warm air masses coming from more sun-exposed areas. On the other hand, in spring, as expected, there is an increase of amplitude then in winter and a decrease of amplitude going from winter to autumn, always in accordance with the increase or decrease of the amount of radiation that arrives on the Earth's surface. This result is coherent with results obtained at other sites in the northern hemisphere and in sites of similar latitudes [84],[83].

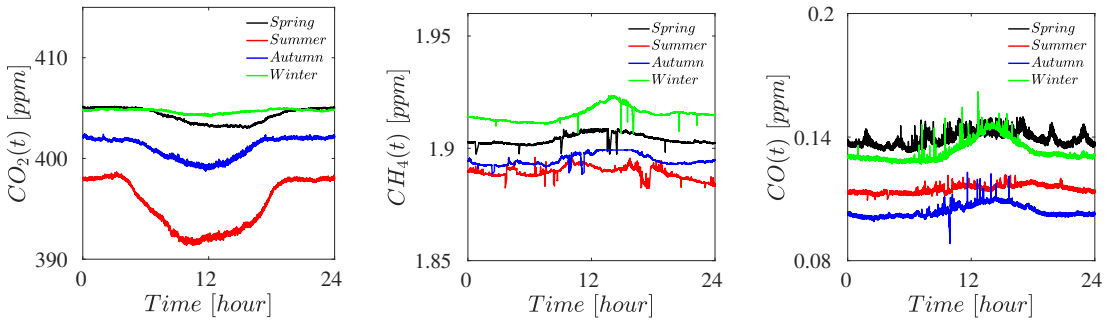

Figure 3.6:
Plot of the diurnal mean cycles of Spring (black), Summer (red) Autumn (blue) and Winter (green) seasons of CO_2 (left panel), CH_4 (central panel) and CO (right panel),

Atmospheric methane has an estimated average lifetime of 12.5 years [75], and this long lifetime implies that methane is nearly conserved during rapid transport from source regions, where dilution due to mixing is limited [76]. The atmospheric distribution of CH_4 is also uniform vertically and exhibits a slight gradient in latitude in the troposphere, where in the mid-latitude troposphere is well mixed with CH_4 both vertically and horizontally[85] (fig.3.7). The records of the temporal variation of CH_4 shown in fig.3.3 (MCU) and in fig.3.4 (MLO), shows a weak seasonal cycle in which the maximum is observed during the winter periods and the minimum during summer periods. The production of CH_4 is mostly produced by anthropogenic activity and bacteria whose activity is strongly dependent on temperature [86],[87]. However, it is possible that a number of sources have seasonal variations that are out of phase with each other so that only small fluctuations of some physical processes can be in phase[85].

The concentration of CH_4 in the atmosphere is governed by the balance between surface emissions of various kinds (anthropogenic and natural) and destruction by OH. The oxidation process, involving the CH_4 with the OH radical is greater in the summer months as water vapour, ozone and solar radiation

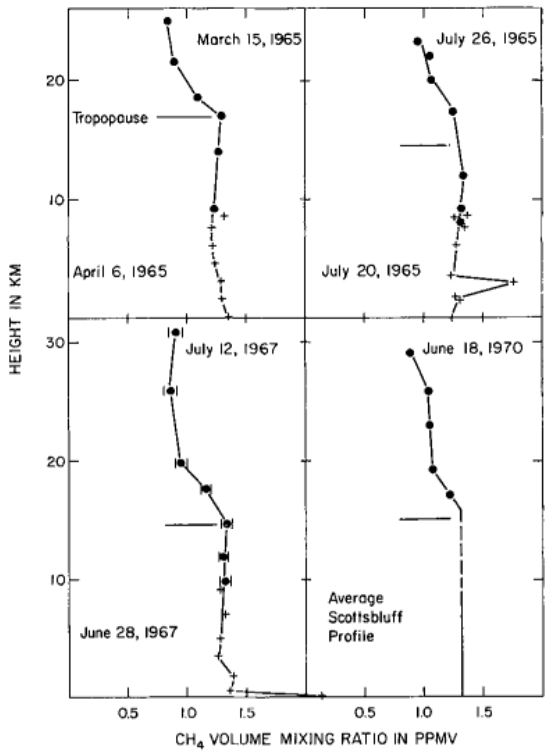

Figure 3.7:
Vertical profiles of the distributions of CH_4, samples from aircraft flights on the date indicated in the lower left corner. The figure was taken from Ehhalt et al.[85].

flux and lead to a higher concentration of OH that balances the higher emission rate of the CH_4[85], [87]. The diurnal cycle of CH_4, fig.3.5 (central panel), is phase-shifted by 12 hours compared to that of CO_2. Maximum values are recorded between 9:00 LT MCU and 15:00 LT MCU with the presence of a double maximum, and the minimum values in the night-time. This feature can also be observed from the diurnal mean cycle in Fig.3.6(central panel). The concentration of CH_4 is higher in winter and lower in summer, the amplitude of cycles and the different values between winter and summer is two orders of magnitude smaller than that of CO_2. The average diurnal cycle, that is evident in winter, can be explained considering that the lower presence of OH in the atmosphere compared to the summer [88] involves a decrease in photochemical reactions with a consequent lower destruction of CH_4 and this explains the higher value compared to summer. In addition, the increase in solar radiation followed by an increase in biological and anthropogenic activities results in a greater release of CH_4 during daytime. In fact, the increase in OH radicals destroys larger amounts of CH_4 resulting in a low temporal gradient.

Concerning the co-dynamic, as shown in fig.3.3, higher concentration of CO

are measured between late winter and early spring, and finally minima in summer. The CO cycle presents gradual increasing between autumn to winter and a rapid decrease in spring. The causes of this seasonal variation in CO are associated with the seasonal cycle of OH and by the timing, location, and distribution of its sources. In case of absence of anthropogenic activity, the concentration of CO is governed by the balance between photochemical production and destruction through the OH reaction [89],[90], in fact CO is the major sink of OH on a global scale [91].

On the diurnal timescales the CO increases from 9:00 LT in autumn and winter while in spring and summer presents an almost constant behaviour with slight peaks in the central hours of the day fig.3.6 (right panel). In all seasons is observed a maximum value in central hours of the days (11:00-17:00 LTO MCU) with a consequent nocturnal decrease [90]. In addition, the mean diurnal amplitude of CO is greater in winter and less in summer which is consistent with other work done on other background sites [91], [92], such phenomenon is attributed to the mixing and vertical transport of the air of the valley to the top of the mountain during daytime.

3.3.1 Multicomponent description and Synoptic scale variations of GHG tracers

In order to capture the synoptic-scale differences in the temporal behaviour of GHG tracers, it is possible to extrapolate specific components embedded in the data [93] given a series of observations $X(t)$ of meteorological and/or atmospheric data, such datasets can be subdivided as follows [94]:

$$X(t) = r(t) + S(t) + W(t) + T(t) + E(t) \tag{3.1}$$

where $r(t)$ represents the trend, $S(t)$ the seasonal cycle, $W(t)$ the slow meso-synoptic scale variations, $T(t)$ the fast turbulent component, and $E(t)$ the instrument errors. In order to characterize and extrapolate the individual components several methods have been proposed including the Zurbenko method (KZ)[95], which is a low-pass filter that uses an iterated moving average and it is based on the application of a filter $KZ_{m,k}$. The $KZ_{m,k}$ filter application is characterized by two parameters, the length of the moving average window, m, and the number of iterations, k, which determine the shape of the energy transfer function [93] that characterize the KZ method. The filtered time series contain low-frequency fluctuations while the difference between the original time series and the filtered

time series includes the high frequency variation of the signal. In this case, to extrapolate from the series the slow meso-synoptic components, it is possible to filter the series through the application of the filter $KZ_{15,5}$, where $m = 15$ in days with $k = 5$ iterations[93], which corresponds to remove all cycles of less than 33 days. The resulting output should then be subtracted from the original time series.

By applying this methodology, it is possible to analyses the annual mean diurnal $W(t)$ of GHG tracers reported in fig.3.8. The overlapping behaviour of

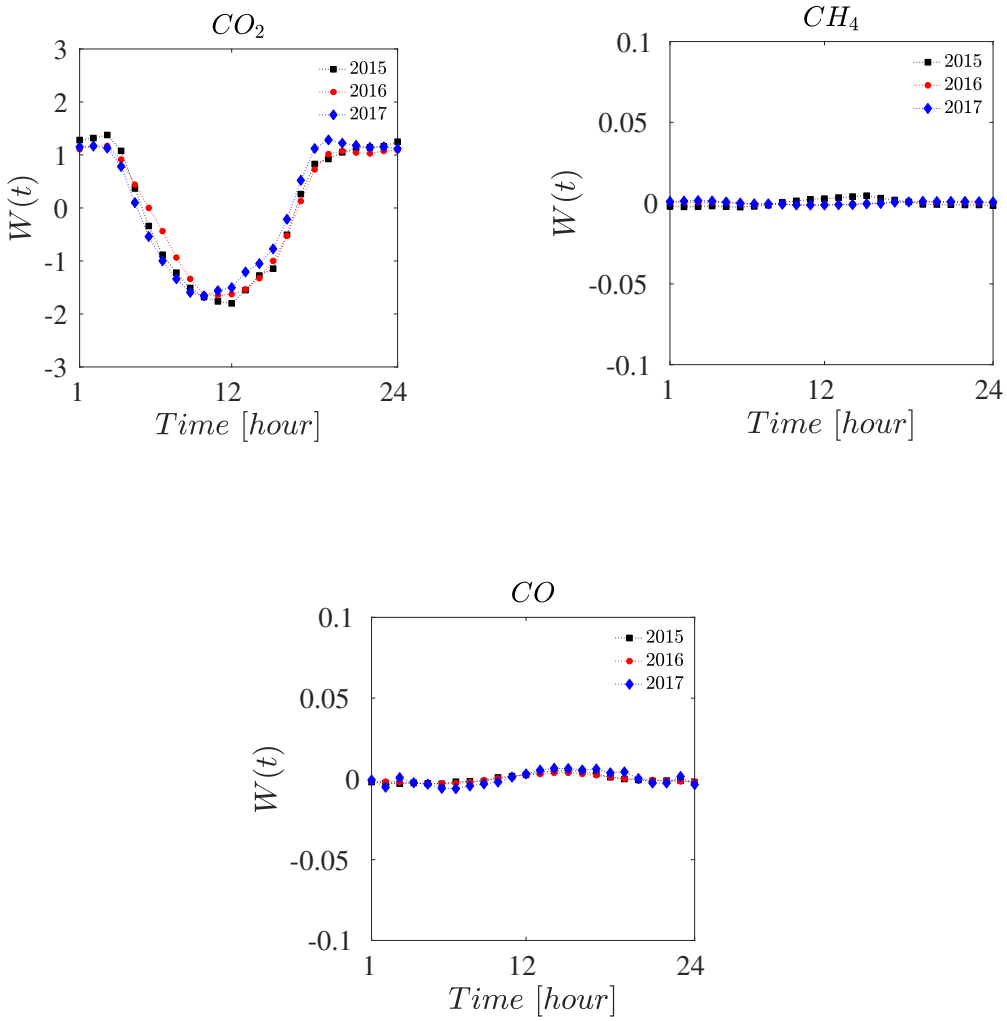

Figure 3.8:
Diurnal mean synoptic-meso components variations of CO_2 (left panel), CH_4 (right panel) and CO (bottom panel) for 2015 (black squares), 2016(red dots) and 2017 (blue diamonds).

$W(t)$ could indicate an equal dynamic of the datasets of annual mean concentrations of GHG tracers. In order to compare and define if there are significant differences between the temporal time patterns of the various $W(t)$ components, it is possible to perform analysis of variance through the ANOVA test with the aim of assessing the different effects in the temporal dynamics between the three different years. The ANOVA test, involves testing the validity of the null hypothesis by comparing two or more data sets that have the same origin, that is, the same stochastic distribution [96]. Verifying if the temporal behaviour of the $W(t)$ in the three years differs, either by ANOVA test or the mean itself, it is important in order to understand how (in terms of coupling strength) variations in meteorological conditions, either anthropogenic or natural in nature, such as forest fires, could influence or not these components. However, applying the ANOVA test to the $W(t)$ of GHG tracers results in $p - values$ equal to 0.99 0.8 0.97 for CO_2, CH_4 and CO respectively. Despite the larger number of forest fire that occurred in 2017 around MCU, especially during the summer season, the dynamics on a synoptic scale of GHG tracers seems unaffected. So that a comparison of the scaling properties of the three different years can be done.

3.4 Environmental drivers for the GHG dynamics

The dynamics of CO_2, CH_4 and CO on an intra-day scale is defined by the combination of some effects referred to environmental drivers.it is of fundamental importance to understand how both the height of the PBL varies, and to define the variation of the photosynthesis-respiration process through the analysis of the EVI and NDVI indices.

For the analysis of EVI (Enhanced vegetation index) and NDVI (Normalized Difference Vegetation Index) the following values were analysed values produced by the MODIS satellite [33]. In fig.3.9 is reported an example of the maps of EVI index (first row) for a double data files, and for NDVI in the same data. The data produced by the MODIS satellite have a time interval of 16 days which have been subsequently monthly averaged and in which each map has a resolution of 0.005*0.005 deg corresponding to about 5km*5km per cell. In addition to considering the seasonal variation of the two indices in the cell centred in the coordinates of the site, the prime cells near the site were also considered, i.e., a 3*3 matrix in which the site represents the central cell. The monthly average variation of EVI (left panel) and NDVI(right panel) is shown in fig.3.10. Both NDVI and EVI are indices that quantify vegetation through

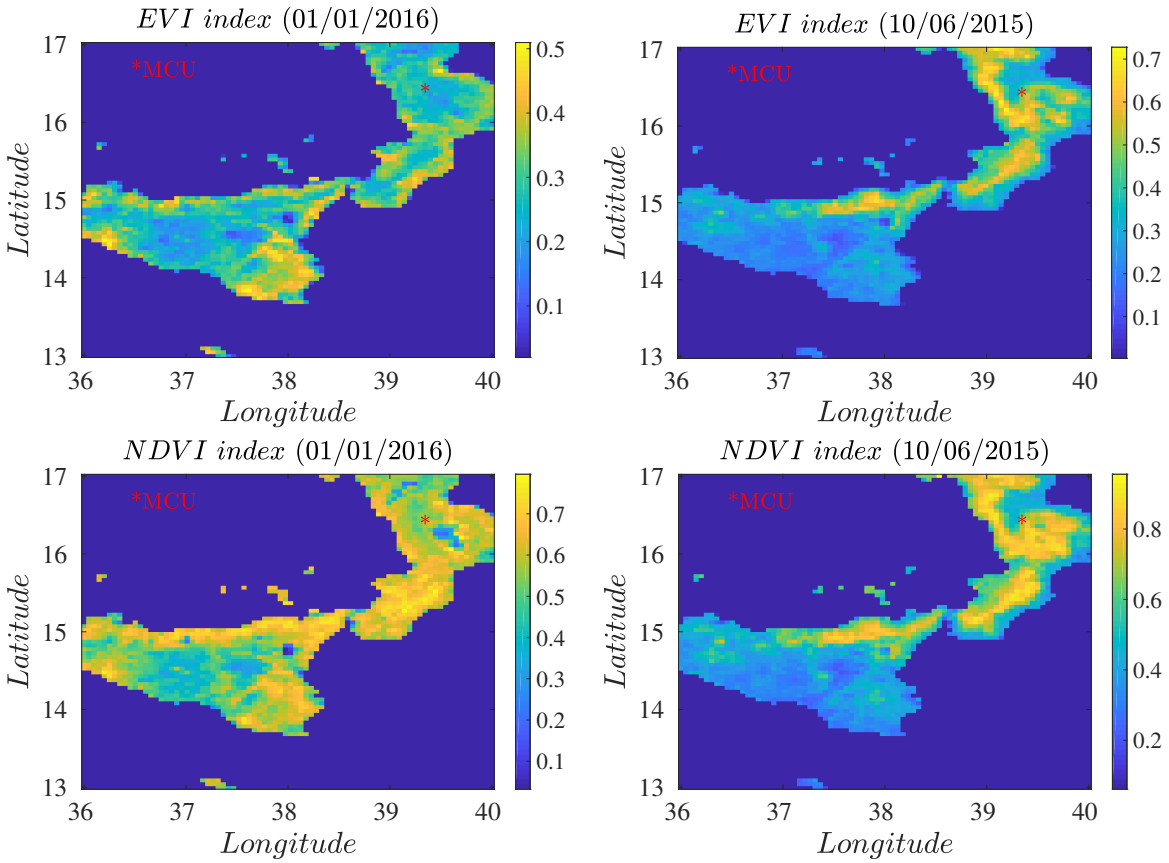

Figure 3.9:
Plot of maps of 16-day 0.05-deg MOD13C1 EVI index product where red star represents Monte Curcio observatory, for four different days. The colorbar on the right indicates the values of the EVI index in each cell, which varies from 0 to 1.

the analysis of spectral reflectance in the infrared (NIR) and visible (VIS) of vegetation. NDVI is defined as

$$NDVI = \frac{NIR - VIS}{NIR + VIS}. \tag{3.2}$$

Thus, as shown in fig.3.11 in which an example of how NDVI is defined is depicted. Vegetation absorbs solar radiation in the different bands of the electromagnetic spectrum and re-emits a different percentage of it in each band. The percentage of re-emitted radiation indicates the state of health of the vegetation, or in other words the condition of vegetation cover. Thus, dense and vigorous vegetation in a cell corresponds to a greater reflection of near-infrared radiation compared with visible radiation and resulting in a large NDVI index. On the contrary a leafy vegetation, which corresponds to the phase between autumn and

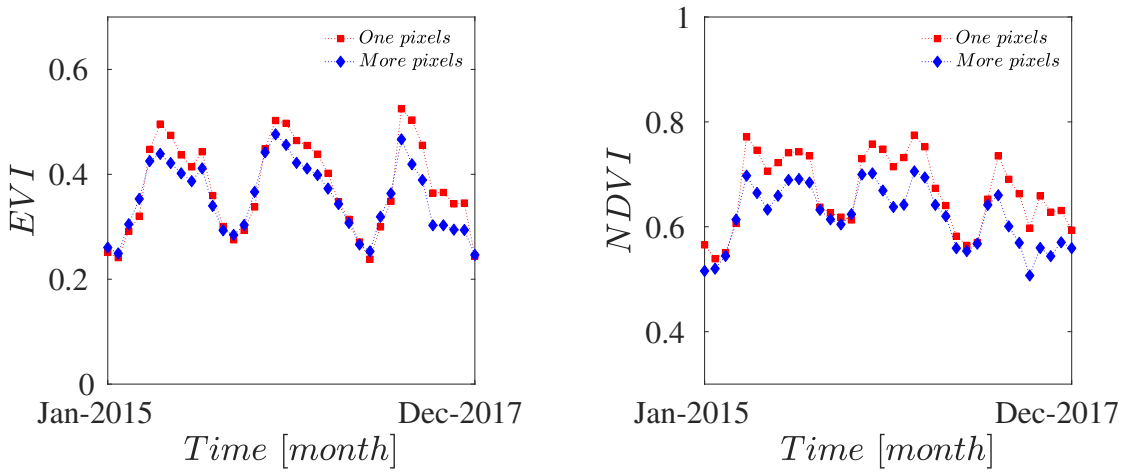

Figure 3.10:
Left panel: Plot of the monthly variation between 2015 and 2017 of the EVI index at MCU, where the red squares represent the monthly variation of an area of $9Km^2$ and blue diamonds an area of $25Km^2$. **Right panel**: Plot of the monthly variation between 2015 and 2017 of the NDVI index at MCU, where the red squares represent the monthly variation of an area of $9Km^2$ and blue diamonds an area of $25Km^2$

early spring, will have a higher radiation in the visible compared to the infrared, decreasing the NDVI value.

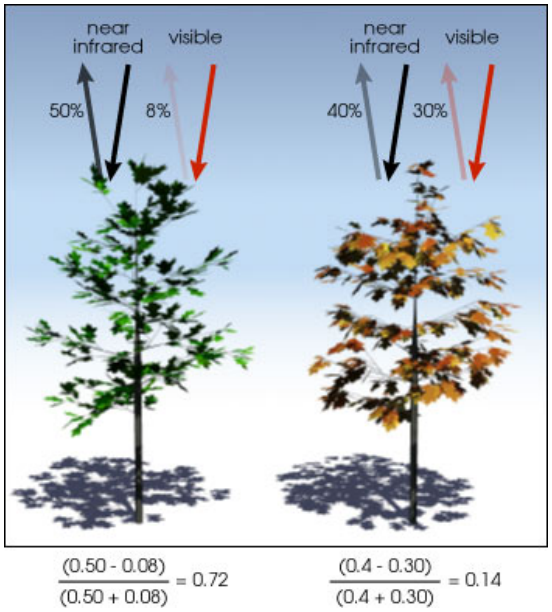

Figure 3.11:
Example of how the NDVI index is calculated and how it relates to the increase and/or decrease in vegetation cover in each cell. Image taken from NASA earth observatory.

Like the NDVI, the EVI is also constructed in a similar way but with more consideration. In fact, NDVI is not precise enough where one wants to estimate vegetation in dense regions of space. Therefore, EVI is introduced to limit the effects of background canopy and atmosphere as well as to better define regions where a lot of biomass is present [97],[98].

However, it is not only this process described so far that drives and defines the intra-day dynamics of CO_2, but it is also and above all the variation of the BL that plays a role of primary importance. The variation of the BL height produces a dilution or a concentration of the pollutants in the sampling region and in the particular case of CO_2, acting significantly on the fluctuations. Since in summer the BL height is deeper, the CO_2 produced is strongly mixed vertically with a transport from low to high troposphere due to convective motions [99]. In contrast, in winter the BL depth is reduced and the signal of respiration is trapped in a smaller region of space increasing the local concentration of CO_2. Therefore, as done for the photosynthesis-respiration process, the BL height data at MCU were also considered here.

To understand how BL height varies, hourly data from ERA5[34], i.e. the fifth generation ECMWF reanalysis, have been considered. The data have a resolution 0.25*0.25 deg in the atmosphere, i.e. each cell is about 11*11 km, which therefore have a lower resolution than the EVI and/or NDVI index data. In fig.3.12 is shown the hourly variation of the BL height for an area of 30*30km obtained by averaging the values of the single cell, where MCU is located at the centre.

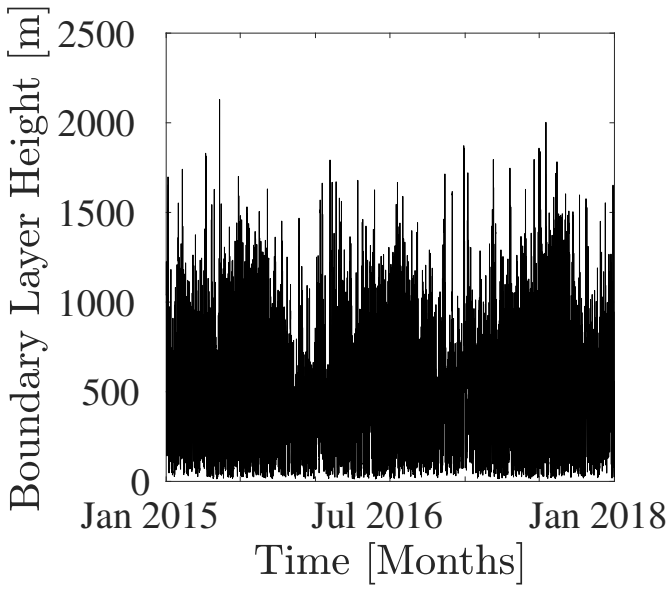

Figure 3.12:
Hourly variation of Boundary layer height for an area of 30*30km obtained by averaging the values of the single cell, where MCU is located at the center.

Chapter 4

Experimental results

This chapter will presents the results obtained from applying the methods discussed in previous chapters on multiple data sets of GHG tracers (CO_2, CH_4 and CO). The main idea of this work is to disentangling and characterize the multiple components embedded in the datasets: fast component, $f(t)$, and a slow component, $s(t)$. This procedure allows to extrapolate statistical information, i.e. scaling and multifractal properties, and link them to the main drivers that affects the dynamics of the concentrations of CO_2, CH_4 and CO.

4.1 Single parameter characterization of slow and fast components of CO_2, CH_4 and CO

4.1.1 Hurst exponent measurement via EMD method

The EMD method was applied on the three years of continuous records (measurements) of CO_2, CH_4 and CO at Monte Curcio. Each dataset is then divided into daily sub-intervals of length $\mathcal{T}_W \approx 8.6 \times 10^4$ sec. The various IMFs $\phi_j(t)$ obtained applying the EMD on the three GHG tracers are in fig.4.1 for CO_2, and in fig.4.2 for CH_4 (first row) and CO (second row) where the residuals $r(t)$ are constant for all three datasets. Note that, in order not to lose readability, the extracted IMFs for the three GHG tracers were divided between even and odd in two different panels.

The "mode mixing" problem, as discussed and analysed in the first chapter, is visible here in all datasets. An example of mode mixing can be appreciated by looking at the $\phi_5(t)$ and $\phi_7(t)$ of CO_2 dataset at time t =4 hour. However, such phenomenon doesn't cause any kind of problem because, as explained before,

IMFs will be combined in partial sum, in order to obtain two new signals: a fast ($f(t)$) component and slow ($s(t)$) component.

The last $\phi_j(t)$ (which is intended as the last IMFs and not the residual $r(t)$) extracted from all three datasets, presents the same modulation discussed for the diurnal cycle. In fact, the behaviour of $\phi_{17}(t)$ of the CO_2 in fig.4.1 (left panel) presents the characteristic double maximum and minimum, observed for the records of the summer season for CO_2 temporal distribution (fig.3.6(left panel)). As for CO_2, the last IMF extracted $\phi_{16}(t)$ fig.4.2(right panel) from the CH_4 dataset has the same behaviour of time distribution of CH_4 fig.4.2 (central panel). However, the behaviour of the last IMFs do not always have these characteristics, since the GHG dynamic varies with the change of days and seasons also the extracted IMFs change behaviour. Finally for CO, the nearly absence of modulation of the last IMF $\phi_{16}(t)$ fig.4.2, in which the maxima and minima are slightly pronounced, is similar with the behaviour seen in fig.3.6(right panel).

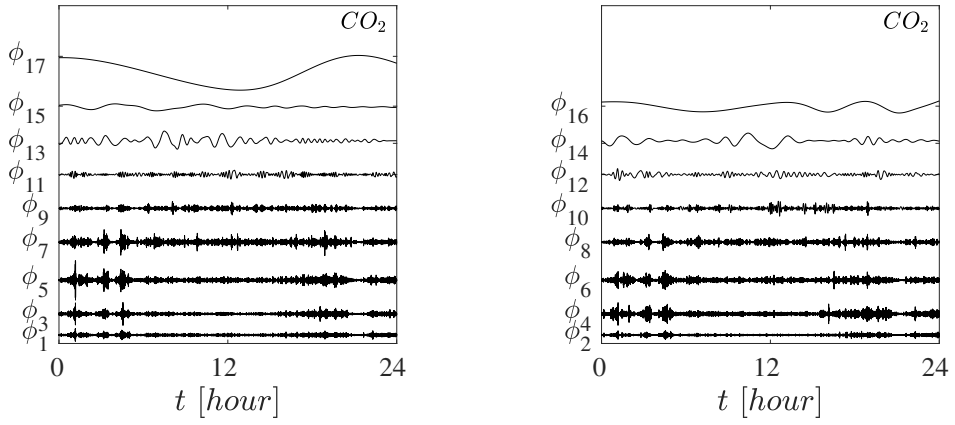

Figure 4.1:
IMFs extracted through the EMD for the sub-interval of duration $\mathcal{T}_W \approx 8.6 \times 10^4 sec$ (one day) for the CO_2. In the left panel are represents the odd IMFs and in the right panel the even IMFS. The residuals $r(t)$ are constant.

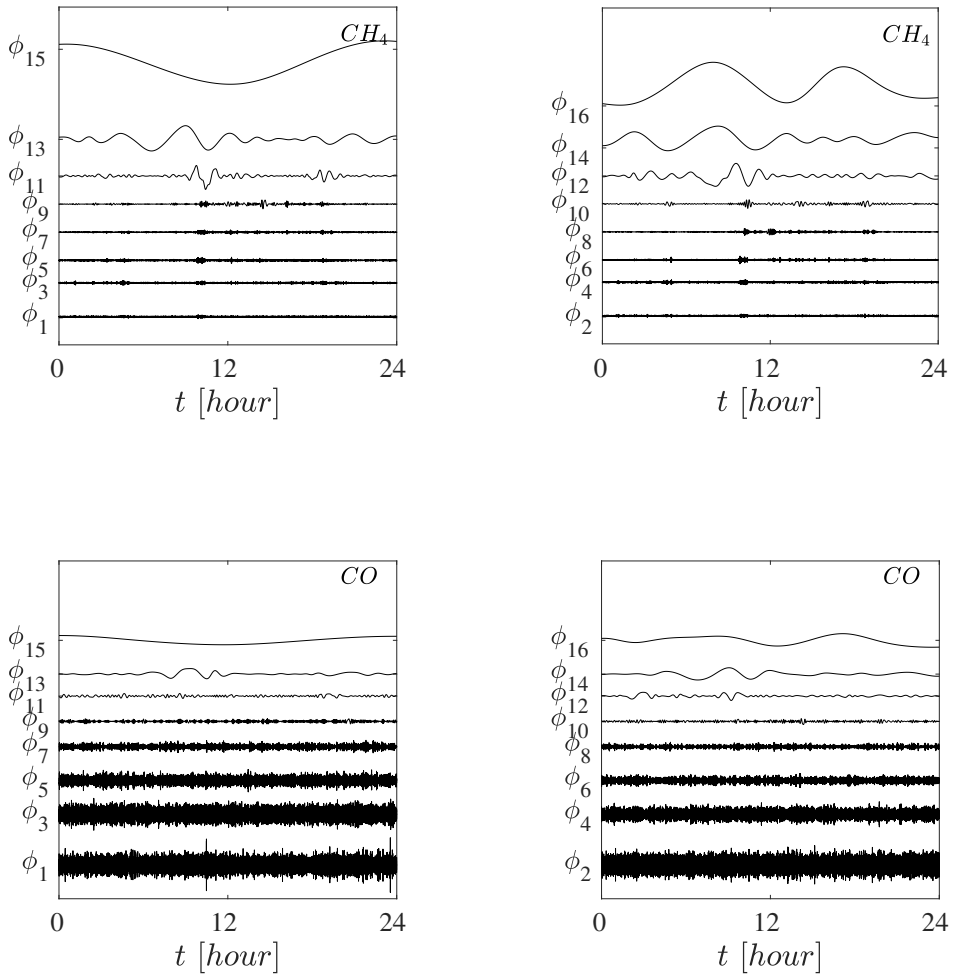

Figure 4.2:
IMFs extracted through the EMD for the sub-interval of duration $\mathcal{T}_W \approx 8.6 \times 10^4 sec$ (one day) for the CH_4 (first row), and CO (second row). In the left panels are represents the odd IMFs and in the right panels the even IMFS The residuals $r(t)$ are constant for all three datasets.

It is possible to extrapolate the scaling properties in terms of the Hurst exponent (empirical estimation), by analysing the energy-based empirical variance, V, in function of number of IMFs, defined as[100]:

$$V_j = \frac{1}{N} \sum_{t=1}^{N} (\phi_j(t))^2 \tag{4.1}$$

where j and N represent the j-th mode and length of $\phi_j(t)$ ($N\Delta t = 86400$ sec). In fig.4.3 (left column) is reported the $log_{10}(V_j)$ as a function of the number of

mode number j for CO_2, CH_4 and CO, respectively. The maximum energy is often in a coherent (slow) modes [101],[100],[102]. For both CO_2 and CH_4 in fact the last $\phi_j(t)$ is the most correlated with the original signals, and possess the highest energy concentration. In other words, in these $\phi_j(t)$ contain most of the information useful to characterize the signal dynamics. For CO the situation is different. In fact the second IMF $\phi_2(t)$ has the highest concentration of energy, almost equal to the last (slow, $\phi_{15}(t)$) indicating that the information necessary for the description of the signal is on two different scales.

Therefore, the characterization of the dynamics should be done according to the chosen scale, and this feature can be evidenced by analysing the correlation that exists between the undecomposed signal with each of its extracted IMFs. In fact, as reported in fig.4.4 for the CO_2 (left panel), the higher value of $\hat{C} = 0.86$ at lag 0 between CO_2 and last IMF ($\phi_{17}(t)$) indicates the maximum correlation, compared to the other two IMFs considered. Same for CH_4 (right panel) in which the last IMF is the one most correlated with the original signal and contains the maximum energy. Referring to the CO (bottom panel), however, having more than one mode that characterizes the dynamics, it is confirmed by the fact that the maximum correlation is with the $\phi_2(t)$ and also with the last IMF although smaller.

The other important feature which be can extrapolated from the IMFs $\phi_j(t)$, is their characteristic period. The behaviour of the mean frequency $\tilde{f}$, calculated as the inverse of the characteristic periods, gives information about how the EMD method performs on the signals under analysis. If the behaviour of $\tilde{f}$ is of the type $\tilde{f} = f_o \rho^{-j}$, where f_0 and ρ are constants and j are IMF number with $\rho = 2$, EMD method acts as a dyadic filter bank in the frequency domain [101]. Furthermore, if $\tilde{f}$ scales as a power law and so if the EMD method is dyadic then the observed phenomenon is multi-scale[37].
In fig.4.3(right column) are represented the behaviours of $log_{10}(\tilde{f})$ for CO_2, CH_4 and CO respectively. The values of ρ are 2.08 ± 0.1, 2.05 ± 0.08 and 2.06 ± 0.1 respectively.

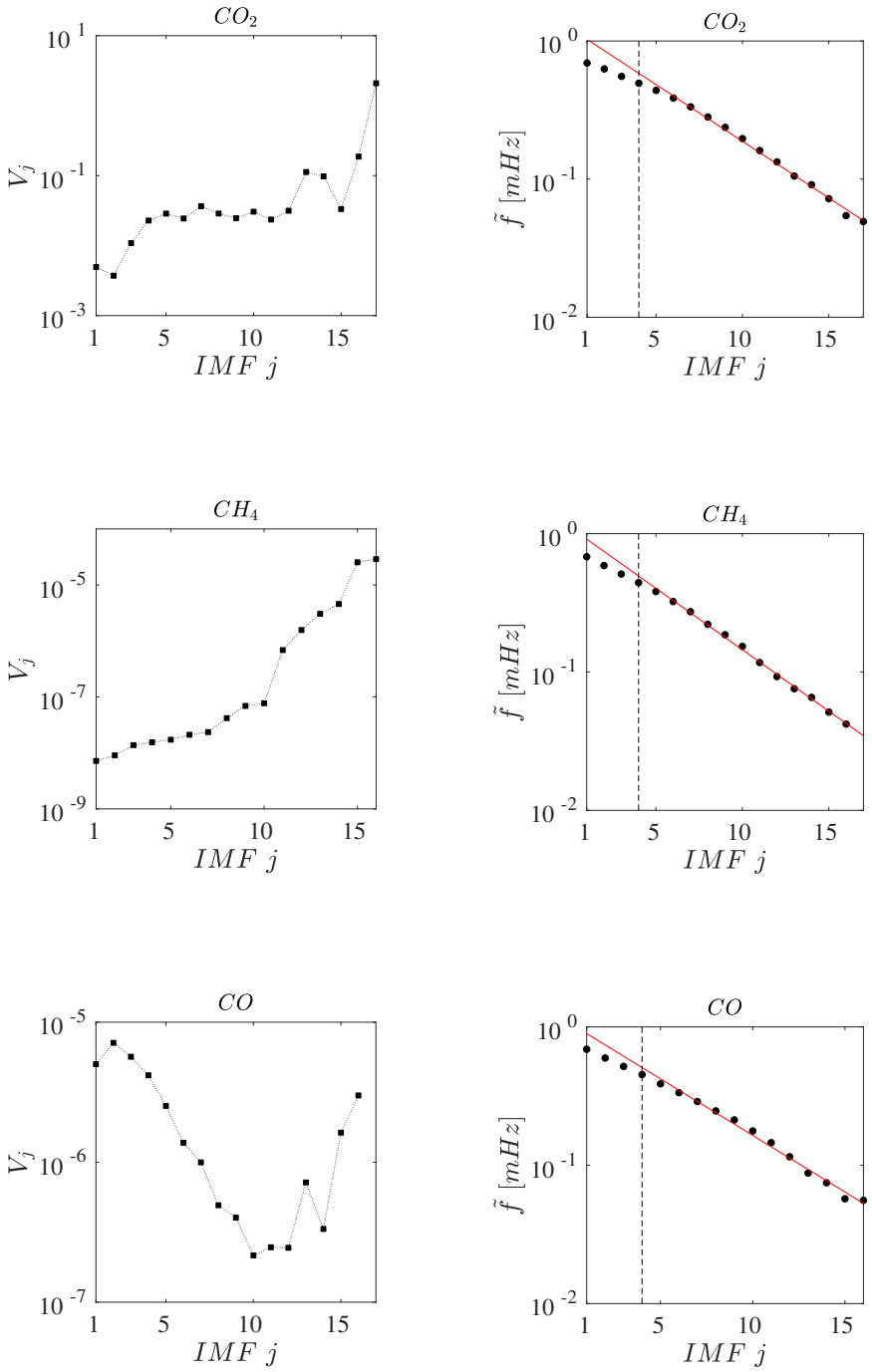

Figure 4.3:
Left column: Log-plot of the variance as a function of the number of IMFs for CO_2, CH_4 and CO. **Right column:** Log-plot of mean frequency for CO_2, CH_4 and CO in function of the number of IMFs. The red lines represent the fit of $\tilde{f}$ where the slope value ρ are 2.08 ± 0.1, 2.05 ± 0.08 and 2.06 ± 0.1 respectively. Vertical dotted line is centred at ϕ_4.

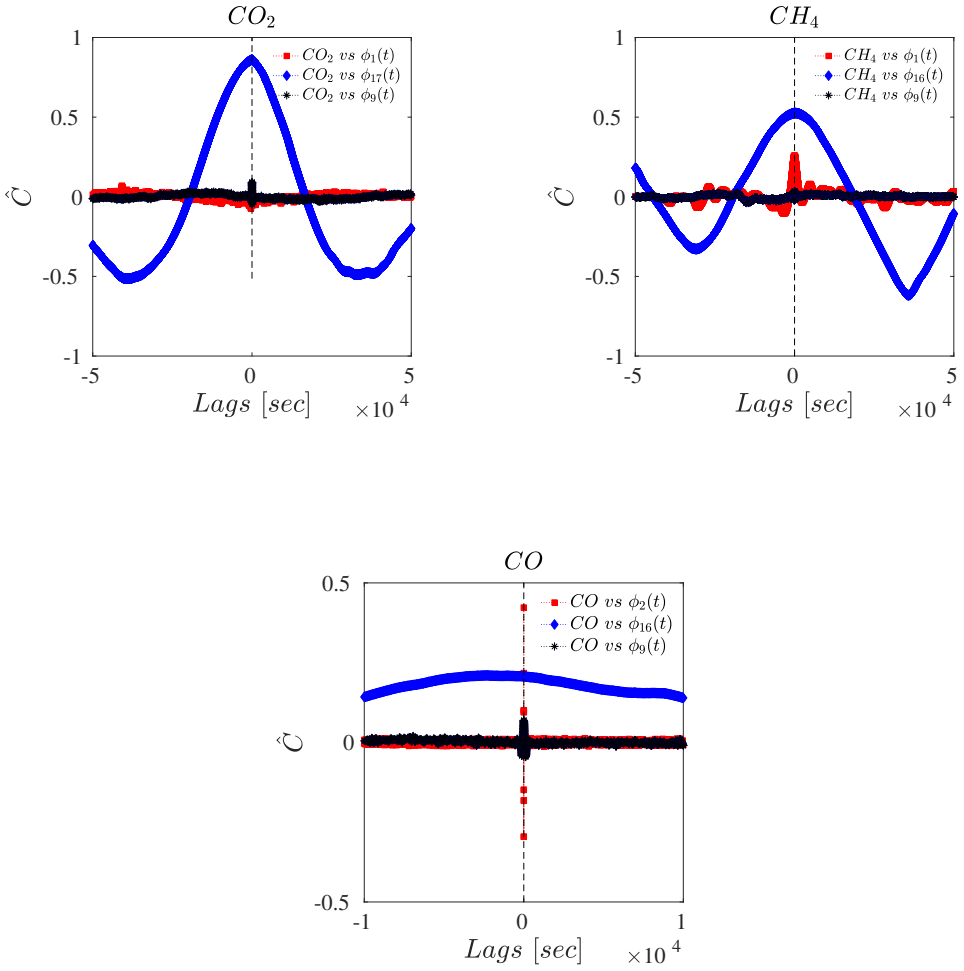

Figure 4.4:
Left panel: Cross correlation between CO_2 sub-interval with the $\phi_1(t)$, $\phi_9(t)$ and $\phi_{17}(t)$ respectively. **Right panel**: Cross correlation between CH_4 sub-interval with the $\phi_1(t)$, $\phi_9(t)$ and $\phi_{16}(t)$ respectively. **Bottom panel**: Cross correlation between CO sub-interval with the $\phi_2(t)$, $\phi_9(t)$ and $\phi_{16}(t)$ respectively. Vertical dotted lines represents $lag = 0$ in all panel.

Empirical estimation of Hurst Exponent from IMF scaling relation

An empirical estimation of Hurst exponents, H_f and H_s respectively for small and large scale, can be obtained by relating the variance value V of the extracted j-th IMF to its characteristic period T_j (or frequency $\tilde{f}$) [32], through the relation

$$V_j \propto T_j^{2H} \tag{4.2}$$

where, the mean period T_j of the j-th IMF is defined as the mean value between the various ΔT_j^+ and ΔT_j^-, which are the differences between consecutive maxima and minima respectively. An example (on the IMF $\phi_{13}(t)$ of CO_2) is shown in fig.4.5. In other words, the average period T_j is computed considering the mean value between the peak, $\Delta \hat{T}_j^+$, of distribution of ΔT_j^+ and the peak, $\Delta \hat{T}_j^-$ of distribution of ΔT_j^-. In fig.4.6 are shown the distribution of ΔT_j^+ of $\phi_5(t)$ for CO_2, CH_4 and CO, in which the dashed lines represents the peak $\Delta \hat{T}_j^+$ where is fitted through a log-normal function, empirically chosen because it minimized the χ^2 and maximized the log-likelihood. The log-likelihood function is joint probability (a measure of the goodness of fit for a model. The higher of the value of the log-likelihood the better a model fits distribution [103]) of the observed data viewed as a function of the parameters of the chosen statistical model[103]

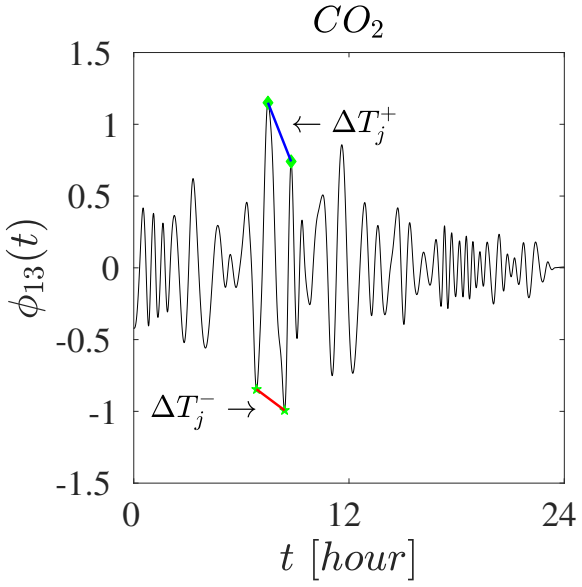

Figure 4.5:
Representation of ΔT_j^+ and ΔT_j^- used to calculate the average period T_j.

In fig.4.7 is reported the log-linear plots of T_j, referring to the datasets shown in fig.4.2, as a function of the IMFs number j. The modes $j \in [5, 15]$, approximately

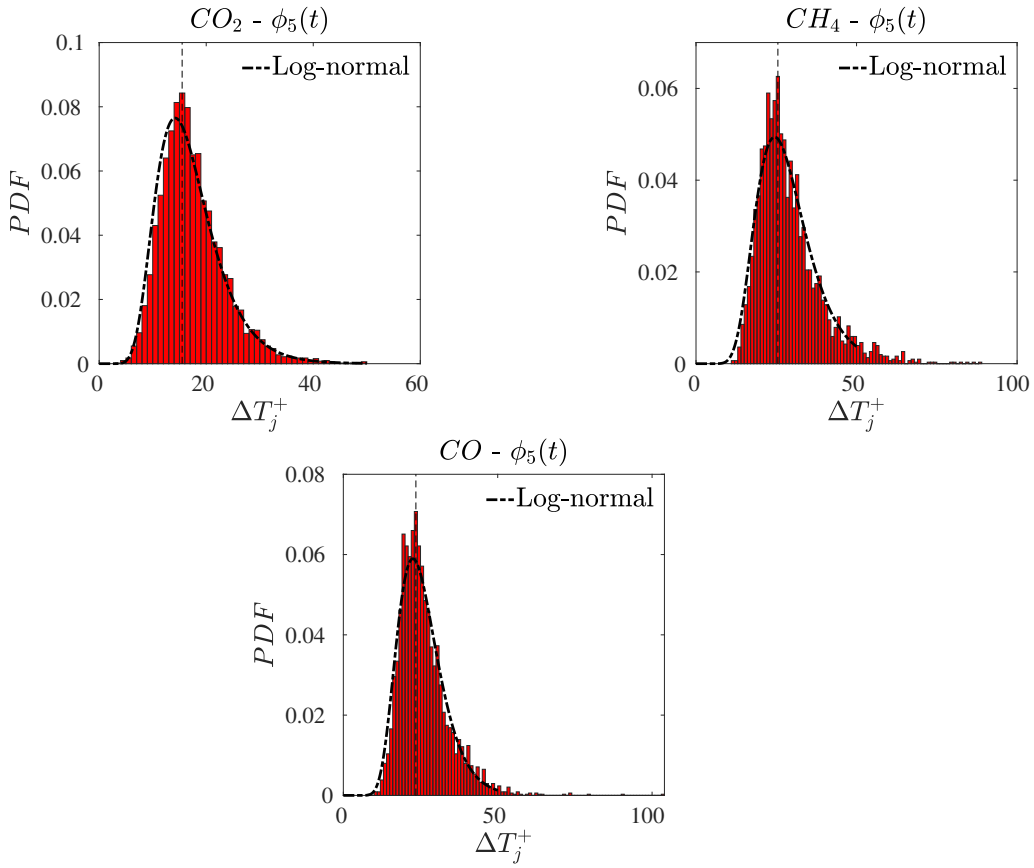

Figure 4.6:
PDFs of ΔT^+ for $\phi_5(t)$ of CO_2 (left panel), CH_4 (right panel) and CO (bottom panel), where the black lines represents the log-normal fit of PDFs.

from $T \approx 100$ sec to $T \approx 6$ hours, follow the exponential law:

$$T_j = T_0 \rho^j \tag{4.3}$$

where $T_0 = 10$ and $\rho = 1.9 \pm 0.03$ for CO_2, $T_0 = 10$ and $\rho = 2.03 \pm 0.02$ for CH_4 and $T_0 = 10$ and $\rho = 1.98 \pm 0.05$ for CO which are obtained via a least squares fitting algorithm. ($\rho \sim 2$, dyadic filter bank [58],[53],[57]).

The value of the coefficient H for each sub-interval is possible estimating the relation (4.2) via a linear fitting of the log-plot of the variance V_j as a function of the period T_j. In fig.4.8 (left column) are shown the log-plots of the V_j for the CO_2 (first row), CH_4 (second row) and CO (third row) in the four different seasons. The first important feature that can be noted is the different scaling observed in the different seasons. Moreover it is possible to define two scaling behaviour on two different range $T_j \in [10, 100]$ sec and $T_j \in [200, 21600]$ sec. The values of V_j for CO_2 and CH_4, regardless of the value assumed by the

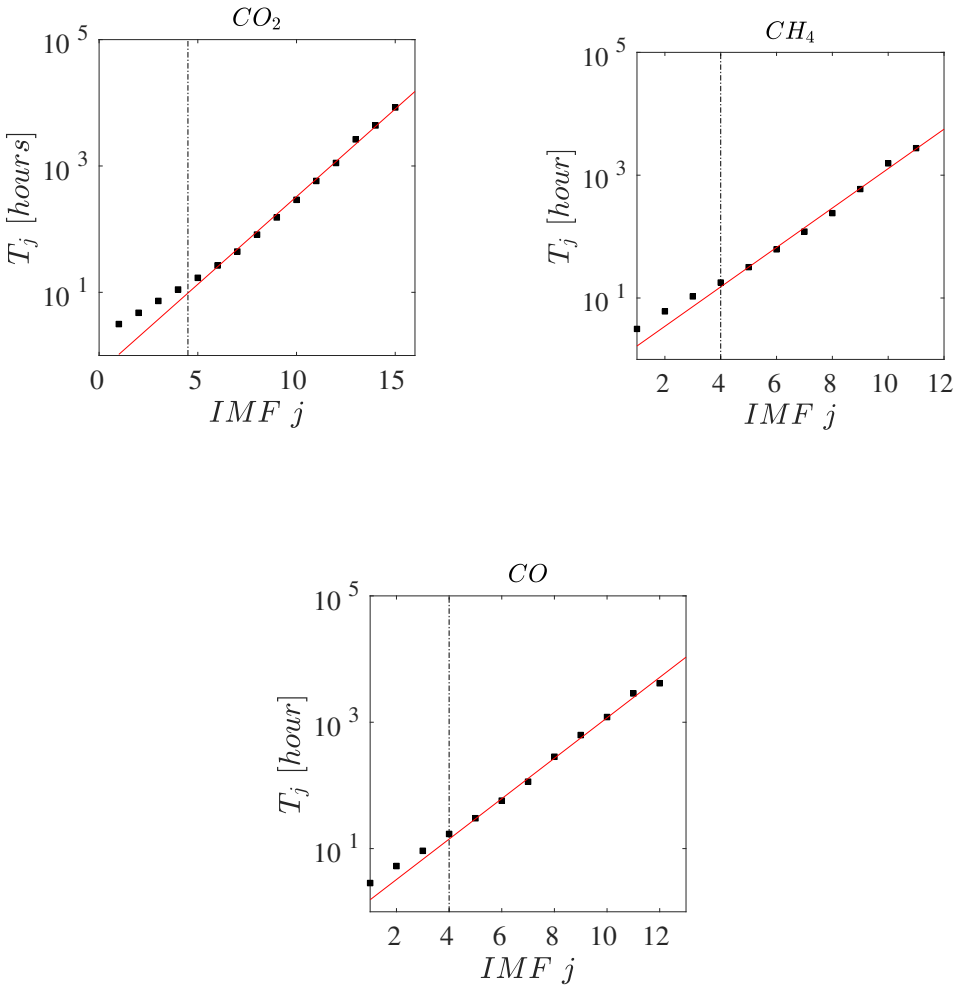

Figure 4.7:
Log-linear plot of the average IMF period as a function of the mode j for CO_2, CH_4 and CO; The red lines represent the relation 4.3, with $\gamma = 1.9 \pm 0.03$ for CO_2, $\gamma = 2.03 \pm 0.02$ for CH_4 and $\gamma = 1.98 \pm 0.05$ for CO.

coefficient H, increasing in contrast to those of CO in the first range of scales. The log relationship between V_j and the mean period T_j is indicative of the fact that the time series of CO_2 and CH_4 are of the type Brownian [32], in contrast to CO which in the small-scale range is a Gaussian noise (Fgn) [37], and a Brownian at large-scale. The first modes of T_j have a different behaviour than the others indicating, in fact, that they are more affected by noise. The value of H can vary day by day due to different climatic and meteorological conditions, anthropogenic activities, forest fires and other factors, so a monthly average has

been chosen to show the variation of their seasonal pattern. In fig.4.8 (right column) are reported the variations of H in the large scale range $\in [200, 21600]$ sec for CO_2 (first row), CH_4 (second row) and CO (third row) respectively.

Given the presence of implicit periodicities within the daily sub-intervals, the ranges in which H values are calculated through the fit, may vary. This is most visible in the calculation of H at small time scales, where the range does not always reach the decade of minimum values in which it is calculated.

For the CO_2 it is interesting to note the periodicity with which the H_s varies, minimums in winter months and maximums in the summer months with an excursion between 0.46 and 0.58. For CH_4 there is also a periodicity but less evident, but for CO there are no appreciable periodicity in the evolution of H_s. However, for $H > 0.5$, long-range correlations are expected. As known from the turbulent scale invariance theory [104], a value of H different from H=0.56 (which represent, the classical passive scalar transport phenomena) is an empirical indication of the abundance of the chemical species depending on whether or not there is a sink or source[104], [105]. For CH_4, being H >0.56, this points out a presence of continuous sink; on the other hand for CO_2 it is observed a seasonal modulation of sink-source. In fact in the winter/autumn H <0.56, while H >0.56 during spring/summer months. Therefore, it could be a link between the modulation of the H of the $s(t)$ component of CO_2 and phenomena that have dissipative behaviour (sink) and others that could behave like a productive organization (source). On the other hand for CO, no trend is appreciable except H >0.56 in the winter months. This it is the evidence of presence of sink and in all other months H <0.56 as predicted by turbulent scale invariance theory [104].

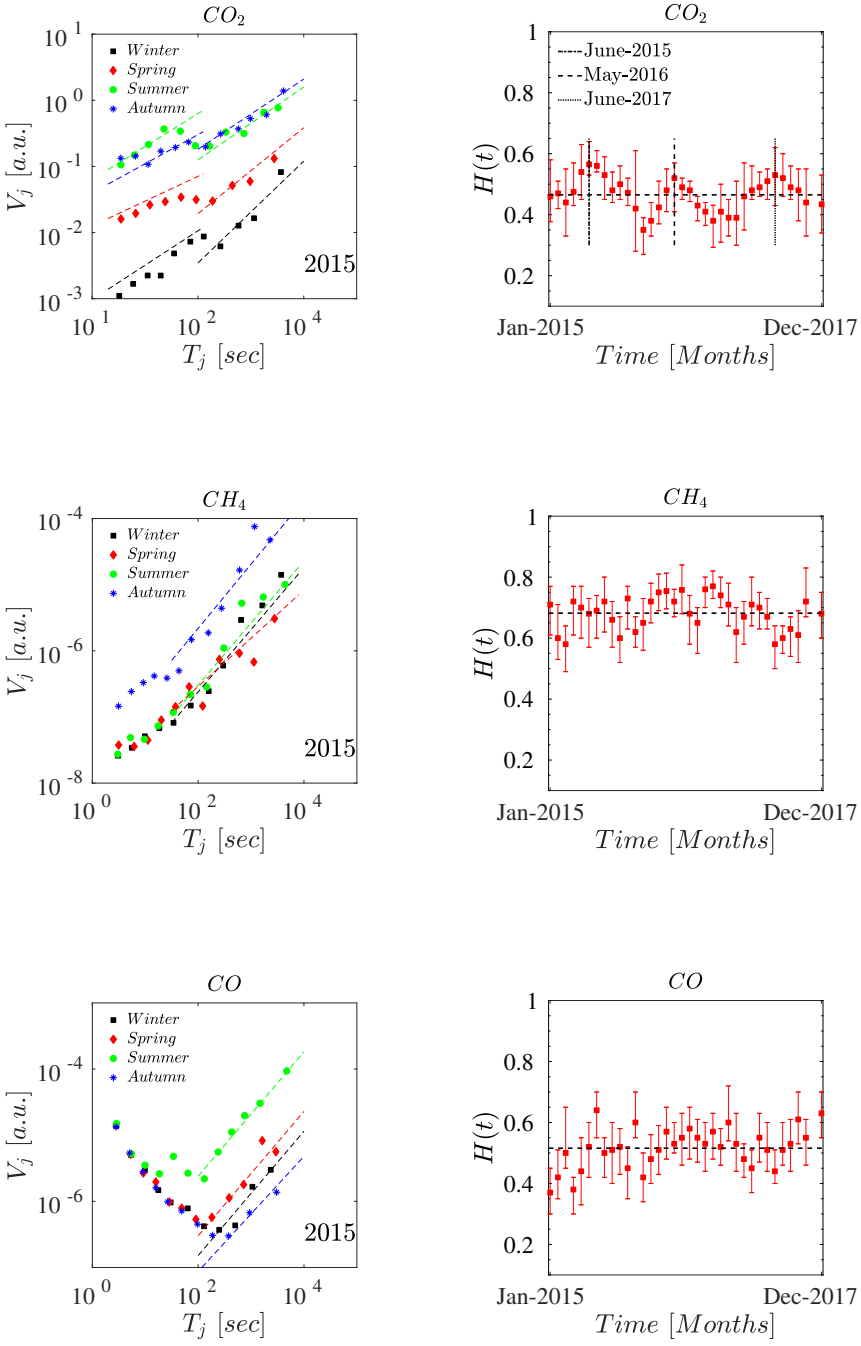

Figure 4.8:
Left column: Log-plot of the variance V_j as a function of the number j of IMFs for CO_2, CH_4 and CO of 2015, where each function is the average of three months in the season. The dotted lines represents the fit, where in all panels is appreciable two scaling range. **Right column:** Monthly variation of H_s at large scale for CO_2, CH_4 and CO, where dotted lines are the mean value H 0.56, 0.65 and 0.52 respectively.

4.1.2 Mutual information exchange approach

To analysing the behaviour in the two different scales range, original datasets are decomposed in a fast component, $f(t)$, and a slow component, $s(t)$. This allows to study their scaling behaviour separately. The components $f(t)$ and $s(t)$, were reconstructed with the method proposed by Rios et al. [69] via Mutual information exchange of IMF phase spectra, allowing the detection of behaviour modifications in consecutive IMFs [69],[106]. The main advantage of this method is that IMF with low frequency presents phase spectra with more similar information.
So, by applying Fourier transform $\mathcal{F}(\cdot)$ on each $\phi_j(t)$ it is possible to obtain a set of complex Fourier coefficients $C_j(\omega) = \mathcal{F}(\phi_j(t))$ in the space of frequencies, $C_j(\omega) = [c_{j,1}, c_{j,2}, ..., c_{j,T}]$ given by

$$c_{j,\omega} = \sum_{t=1}^{T} \phi_j(t) e^{\frac{-i2\pi\omega t}{T}} \tag{4.4}$$

where $w \in \{1, 2, ..., \frac{T}{2} - 1\}$, T is the length of $\phi_j(t)$ where the last point is $\frac{T}{2} - 1$ in agreement with the Nyquist-Shannon theorem [107].
After computing the Fourier coefficients for each individual $\phi_j(t)$ the phase spectrum of each component is defined as

$$\Theta_j = \tan^{-1}\left(\frac{\Im(C_j(\omega))}{\Re(C_j(\omega))}\right) \qquad \forall j \in \{1, 2, ..., T\}. \tag{4.5}$$

where $\Im(\cdot)$ and $\Re(\cdot)$ are the imaginary and real part of $C_j(\omega)$. Finally the Mutual information is computed between two consecutive phase vectors belonging to two adjacent IMF as $v_j = I(\Theta_j, \Theta_{j+1})$.

Then, comparing two consecutive $\phi_j(t)$ through their v_j value, the obtained Mutual Information for the first IMFs is expected to be close to zero, since the correlation between them is low[69]. However, since they are considered IMF with progressively smaller frequency the Mutual Information obtained between IMF successes produces a v_j value that is progressively larger[69]. Calculating the average of these v_j, called cut-off point v_z, it is possible to define a limit between the IMFs that exchanges more o less informations. Considering the index z like maximum index for which IMF with a lower index, it represents the fast component of the signal with those a higher index representing the slow part of the signal. This idea, along with the $I(\Theta_j, \Theta_{j+1})$ values computed for the analysed datasets, is reported in fig.4.9 where the Mi values for CO_2

are represented in log-plot. However, considering the log-plot it is possible to extrapolate additional information inherent in the high-frequency modes and thus the fast component. In fact, it can be seen that there is an additional jump between the values of $I(\Theta_j, \Theta_{j+1})$ for the first two modes compared to the others. In fig.4.9 are reported the Mi values for CO_2 (left panel), CH_4 (right panel) and

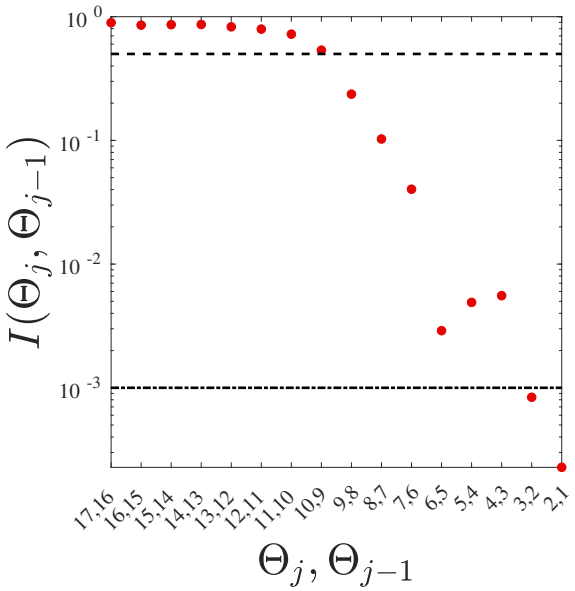

Figure 4.9:
Semi-log plot of mutual information performed for CO_2 in which the two dashed lines represent the cut-off point where the MI change. Down dotted line represent the point that divided the noise to fast component, and upper dotted line the point that divide the fast and slow component.

CO (bottom panel) respectively. As reported in fig.4.10, for all three GHG tracers present a increasing value of $I(\Theta_j, \Theta_{j-1})$ as the period T_j increases. In fact IMF approaches the value $I \sim 1$ at large temporal scales. On the contrary, high frequency ω have $I(\Theta_j, \Theta_{j-1})$ close to zero. In all cases a significant gap is observed when I approach the value $I \sim 0.5$ which is just the value of the cut-off point v_z.
The two components of the signal, the $f(t)$ and the $s(t)$, are then reconstructed as

$$f(t) = \sum_{j=3}^{z} \phi_j(t) \qquad s(t) = \sum_{j=z+1}^{N} \phi_j(t). \tag{4.6}$$

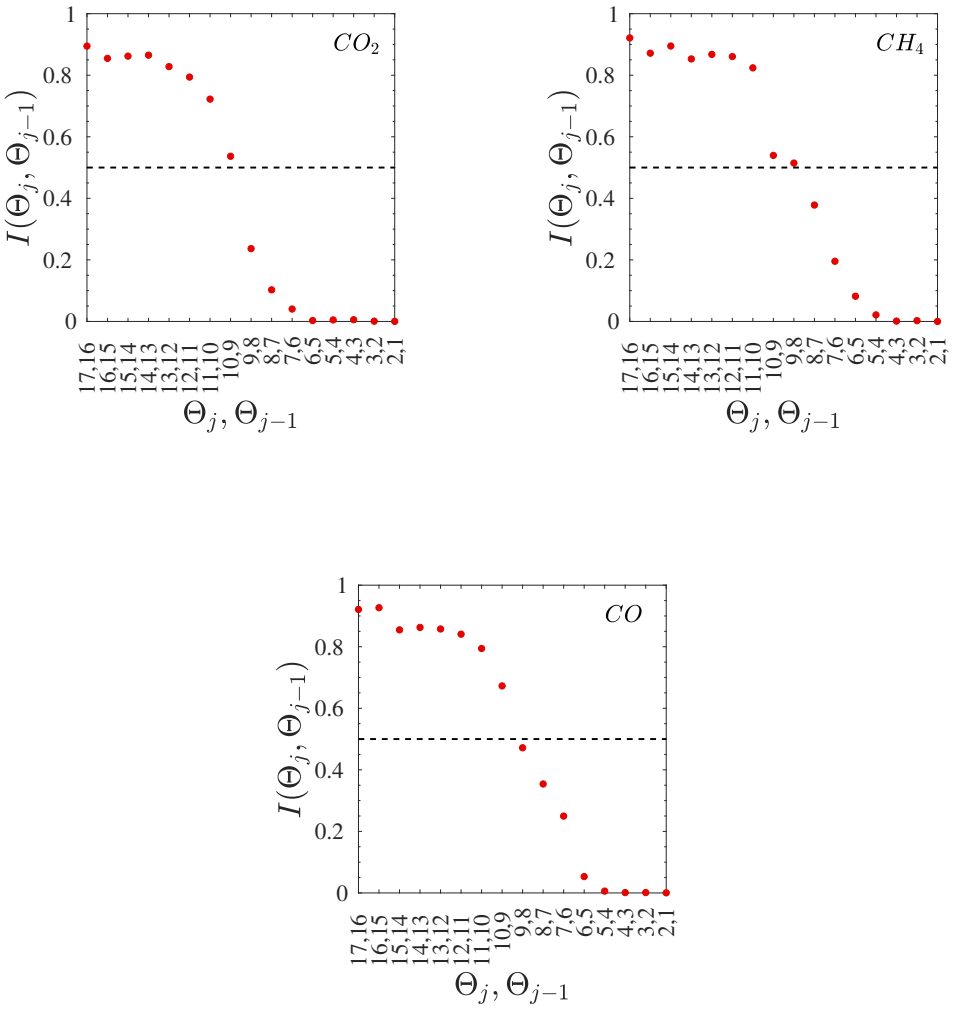

Figure 4.10:
Mutual information method performed for CO_2 (left panel), CH_4 (right panel) and CO (bottom panel) of datasets in fig.3.5. The dashed lines represent the value of cut-off points that in all three cases is 0.5 since, being that the MI method produces values included between 0 and 1, and having been subsequently normalized produce such average value.

So the sum of every $\phi_j(t)\ \forall j \in \{3, ..., z\}$ represents the fast component $f(t)$ and the sum of $\phi_j(t)\ \forall j \in \{z+1, z+2, ..., N\}$ the slow component $s(t)$. The first two IMFs as shown in fig.4.9 are distinguished by having almost zero information exchange, having as value $I < 10^{-3}$. In the decomposition performed these two IMFs are considered noise $E(t)$ in the datasets. Is important to observe that no approximation is involved in this procedure in which the original time series $x(t)$ is obtained by summing $x(t) = f(t) + s(t) + r(t) + E(t)$.

4.1.3 Significance test for intrinsic mode functions

The $\phi_j(t)$ extracted through the EMD method are of empirical nature. It may happen, however, that some IMFs do not contain useful statistical information and thus are not physically meaningful. For this reason, a test based on the IMFs energy content and their average period was introduced to check whether the IMFs extracted during the sifting process are meaningful or not[53]. On the other hand, since one wants to quantify the information exchanged only by the meaningful modes the test is applied to the IMFs of the datasets of GHG tracers GHG tracers, discarding the unnecessary IMFs. For instance, if the imf ϕ_4 and ϕ_6 are physically meaningful and ϕ_5 does not contain useful statistical information, the mutual information is computed only between modes ϕ_4 and ϕ_6. So, it is possible to estimate the energy density E_j contained in each IMF mode as a function of the mean period T_j through the relation[108],[109]:

$$Log_{10}(E_j) + Log_{10}(T_j) = const. \tag{4.7}$$

For a normalized white noise series, there is no loss of generality by assuming the constant equals 0 [108],[109].
The theoretical behaviour of the relationship written above for a normalized white noise series is shown in fig.4.11, where the theoretical line, represented by the 90% (red line) and 95% (blue line) significance levels, respectively, for white noise. The behaviour of energy importance of the IMFs, provided both inherent indication of the statistical importance of the information contained in them compared to the theoretical line and to the series whether they are noise-like, or not. The fact that every level lies below the theoretical line is an indication that little useful statistical information is contained in all the IMFs, that corresponds unperceivable physical processes[108]. Similarly, one can check how the energy significance of the IMFs of the sub-intervals of CO_2, CH_4, and CO behave, which are shown in fig.4.12. The first feature observed is the different behaviour of energy density E_j from the theoretical line, represented by the 90% (red line) and 95% (blue line) significance levels, respectively, of white noise in all three panels. For CO_2 (left panel) and CH_4 (right panel) all IMFs have a different trend from the theoretical line as well as having values above them indicating that these IMFS are all significant containing importance information in describing the physical processes that characterize them. On the other hand for CO, the behaviour of the early IMFs follows the theoretical line and then diverges from it; although each individual IMF contains statistical information for describing

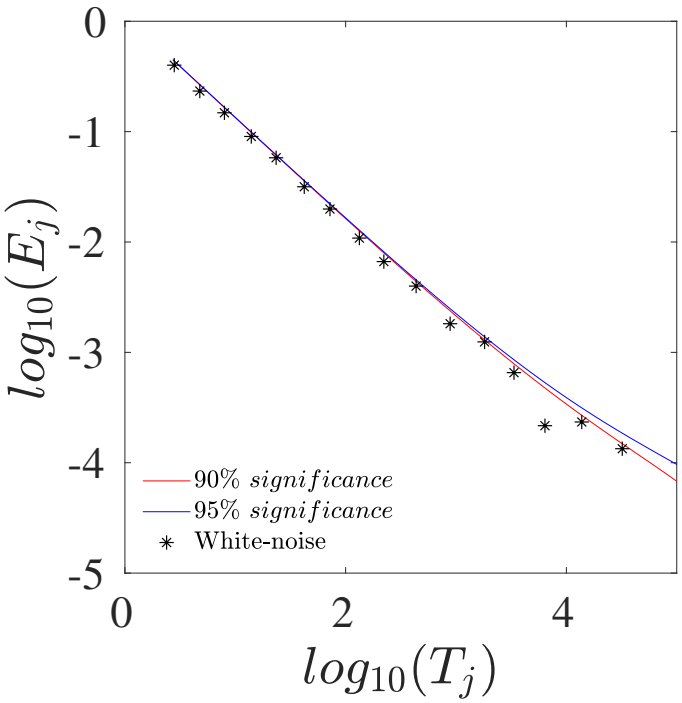

Figure 4.11:
Log-log plot of energy density E_j versus averaged time T_j of IMFs of white noise series of length 10^5 points(black stars). Red and blue lines correspond respectively to 90% and 95% significance confidence intervals.

the time dynamics of the series. This indicates two different behaviours of the CO series according to the time-scale range considered.

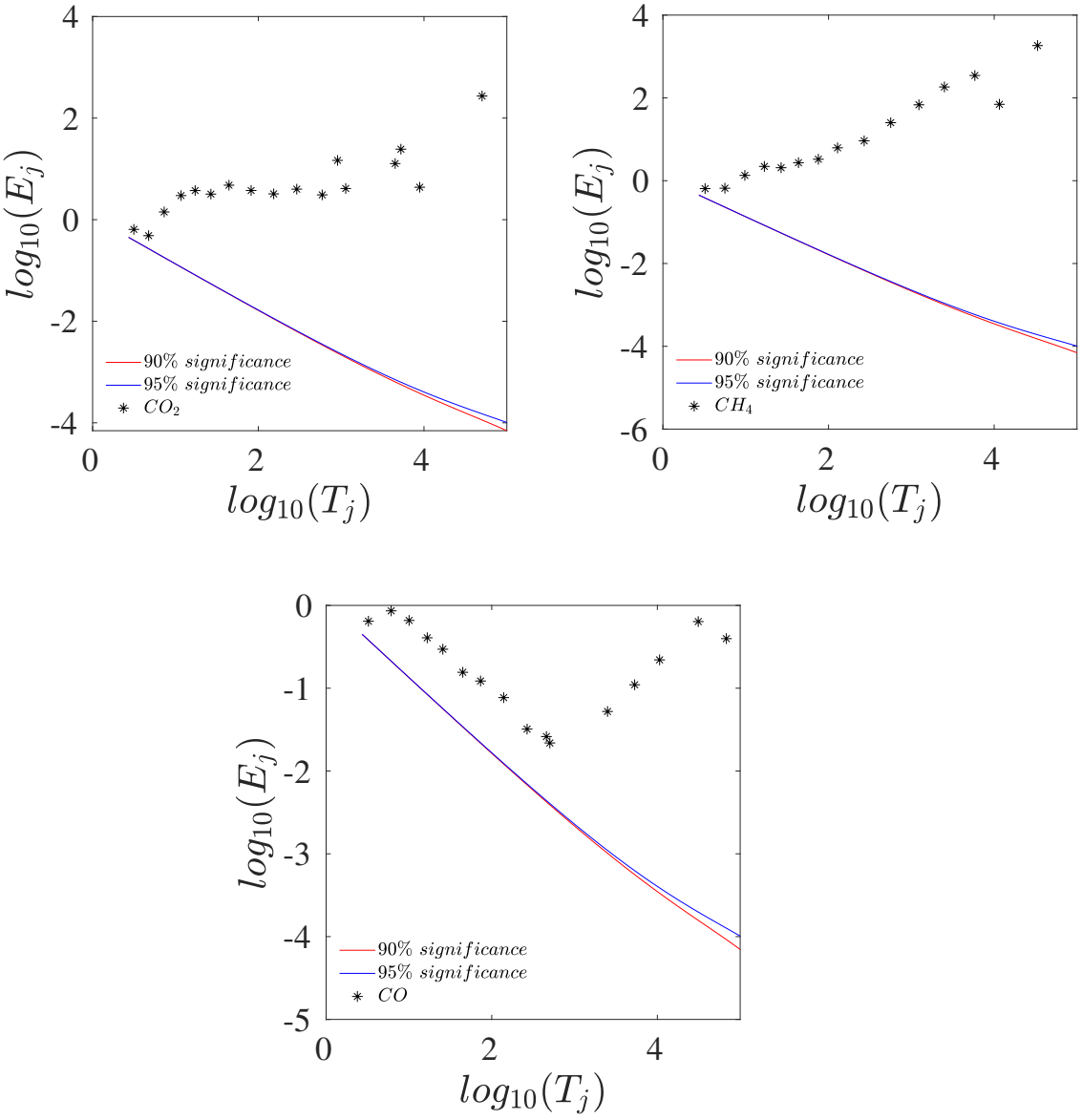

Figure 4.12:
Log-log plot of E_j for IMFs for sub-intervals of CO_2 (left panel), CH_4 (right panel) and CO (bottom panel) respectively. Red and blue lines correspond respectively to 90% and 95% significance confidence intervals in all three panels.

4.1.4 Multicomponent identification

Through the study presented in Section 3.3.1, it is possible to analyse GHG datasets through extracted IMFs. The advantage here is that there is no need to apply any kind of filtering or moving average windows, because the construction of the various components $E(t)$, $f(t)$ and $s(t)$ can be obtained simply by exploit-

ing the properties of the EMD through partial sums of the various IMFs. The components $E(t)$ ($\sum_{j=1}^{2}\phi_j(t)$), $f(t)$ ($\sum_{j=3}^{9}\phi_j(t)$) and $s(t)$ ($\sum_{j=10}^{16}\phi_j(t)$) derived from fig.3.5 are shown in fig.4.13. However, it should be noted that the partial sum is not always done among the same indexes of modes, but depends on both the number of modes extracted and the value of Mutual information through the method described above.
The first, second and third rows represents the components $E(t)$, $f(t)$ and $s(t)$ respectively for CO_2, CH_4 and CO. The $E(t)$ and $f(t)$ components of all three GHG traces are zero-mean by definition[110]. On the other hand, the components $s(t)$ are also zero-mean. The residual $r(t)$ was not considered because being flat it has the sole function of being an offset. In the analysis carried out, it was seen that the addition of the residual $r(t)$ in any case does not change the results obtained, let alone the behavior of the components.

Moreover, in the components $s(t)$ are captured the characteristic diurnal modulation cycle that is recorded in the original dataset. Consistent with what is seen in the second chapter, the $s(t)$ component has the same behaviour of the $W(t)$ component which, for 2016 alone, is reported in fig.4.13 (bottom row) for all three GHGs. Through the decomposition it is possible to assert that the component $f(t)$ could be considered as the turbulent component $T(t)$ described by Rao et al.[94], because this component evolves on the typical timescales of the atmospheric turbulence and can be compared. Therefore, the study and analysis of the scaling properties of $f(t)$ can be related to the scaling properties of the turbulence.

The corresponding probability density functions of $f(t)$ and $s(t)$ components are shown in fig.4.14. Since the two components are zero mean the PDFs are centred at zero, but it is interesting to note that those of CO_2 and CH_4 have two maxima. This is related to the presents of diurnal periodicity where maxima and minima alternate over time where the concentrations are different. However, even if CO is affected by diurnal cycle in the PDF of $s(t)$ of CO the double maxima are not appreciable, since they are only closer than the other two GHGs.

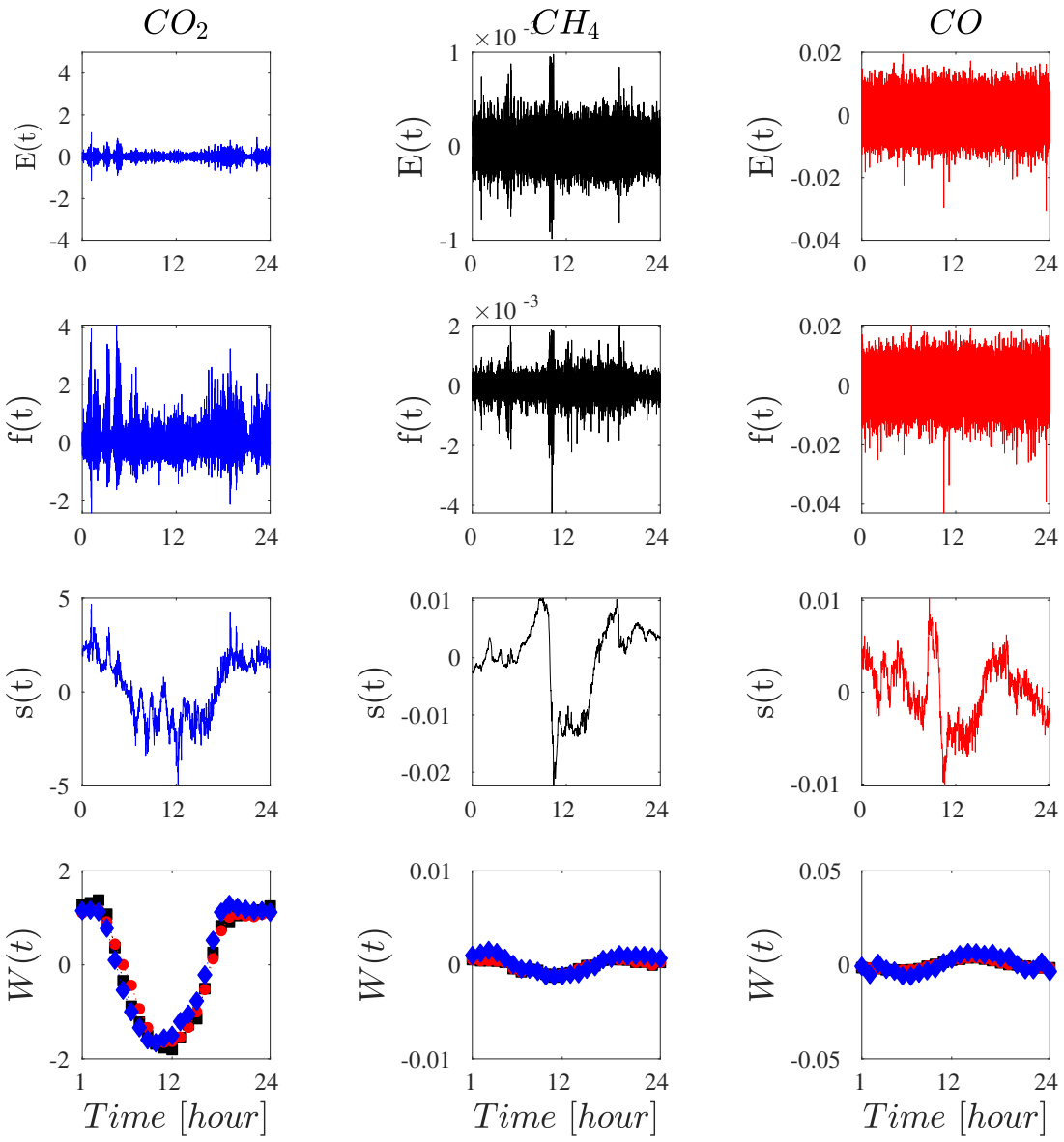

Figure 4.13:
First row: Plot of $E(t)$ of 01-06-2016 daily intervals for CO_2, CH_4 and CO. **Second row**: Plot of $f(t)$ 01-06-2016 daily intervals for CO_2, CH_4 and CO. **Third row**: Plot of $s(t)$ 01-06-2016 daily intervals for CO_2, CH_4 and CO. **Fourth row**: Plot of $W(t)$ for CO_2, CH_4 and CO of 2015 (black square) 2016 (blue diamond), and 2017 (red diamond).

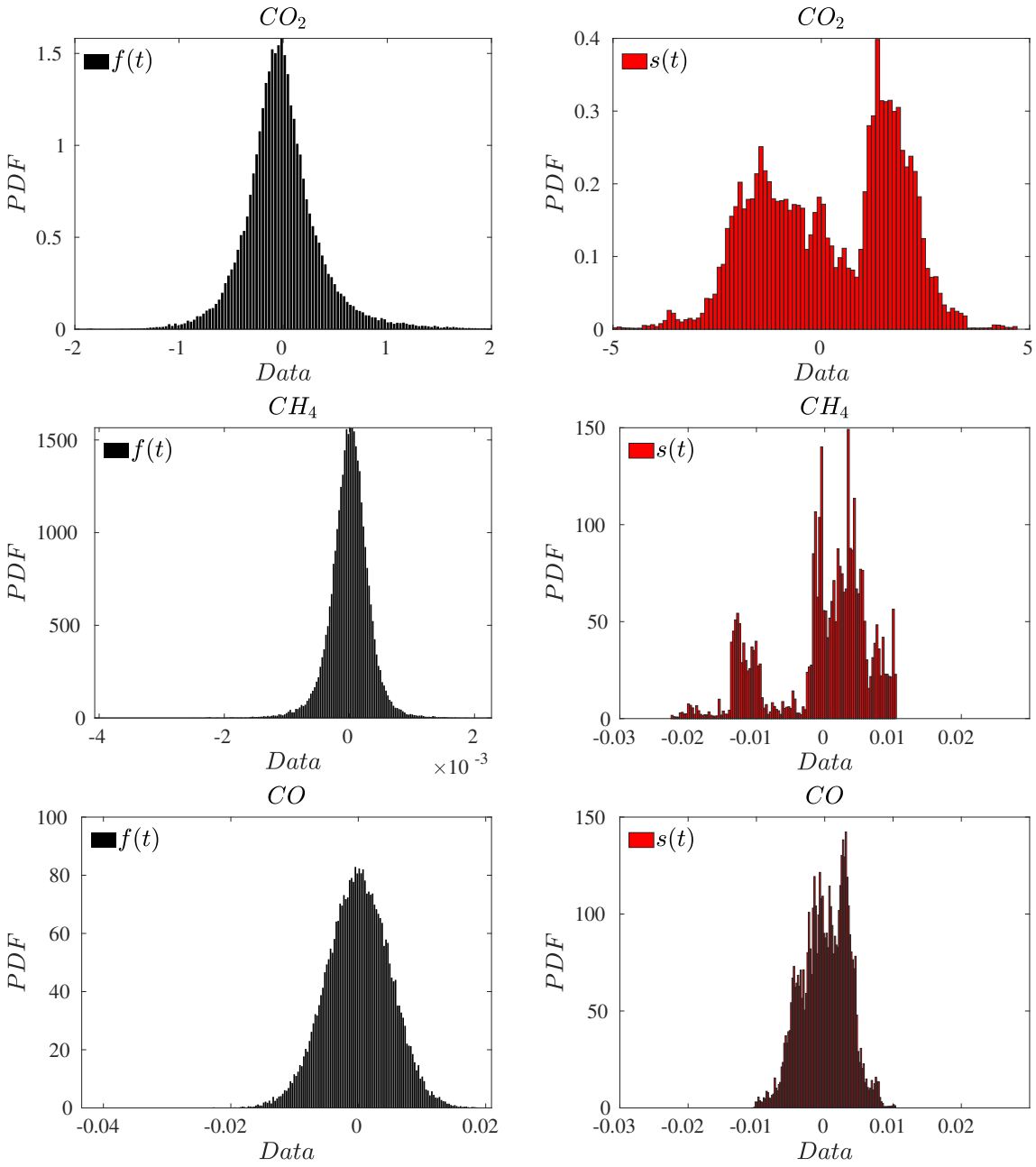

Figure 4.14:
Left column: PDFs of $f(t)$ component for CO_2 (first panel), CH_4 (central panel) and CO (bottom panel). **Right column**: PDFs of $s(t)$ component for CO_2 (first panel), CH_4 (central panel) and CO (bottom panel).

Analysing these two components in frequency domain allows to obtained information about the value of the coefficient H given by the relation $\beta = 2H + 1$ [31], where β is the slope of PSD. Fig.4.15 shows the PSD of the $s(t)$ and $f(t)$ for CO_2 (left panel), CH_4 (right panel) and CO (bottom panel). The extrapolation of the slope β is performed on 2 different range scales. For CO_2 the value of β

(dashed lines in fig.4.15, are 1.744 and 1.91 respectively for $f(t)$ and $s(t)$. This values are calculated through a least square linear fitting. Regarding CH_4 β values have been founded, where 1.73 and 1.71 are for $s(t)$ and $f(t)$ respectively. For CO, in according with the analysis previously conducted, the slope $\beta = 0.14$ of the spectrum is a confirmation that $f(t)$ is a similar noise, specifically an Fgn. Calculating the spectra of each daily sub-interval and then the values of the H_s and H_f coefficients, the monthly mean variations can be defined, as shown in fig.1.94.16 for CO_2.

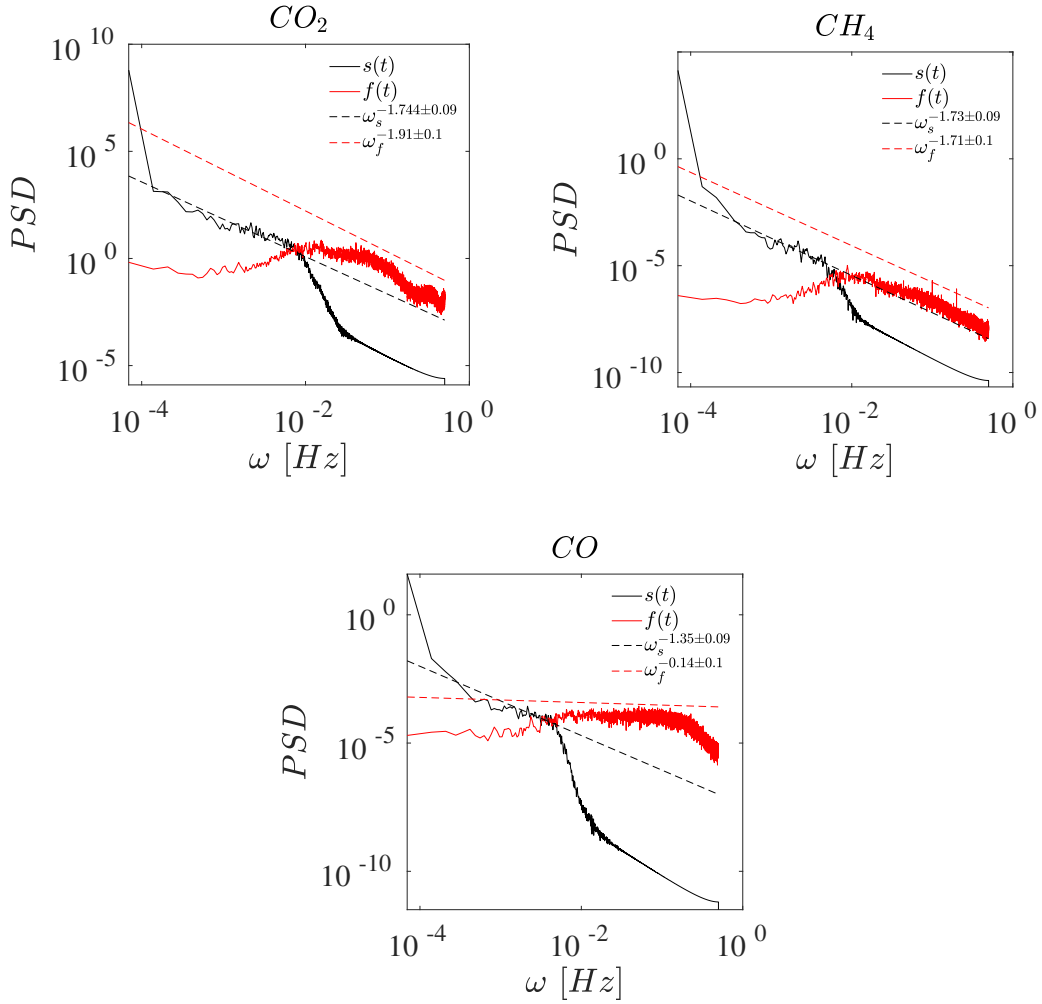

Figure 4.15:
Plot of power spectral density of $s(t)$ (black) and $f(t)$ (red) component for CO_2 (left panel), CH_4 (right panel) and CO (bottom panel) in function of frequency ω. The dashed lines represents the value of function that fits the spectra. So, for the $s(t)$ component of CO_2 the value of β is 1.744 and for $f(t)$ is 1.91. For CH_4 the values of β are 1.71 and 1.74 for $s(t)$ and $f(t)$ respectively, and finally for CO are 0.14 and 1.35.

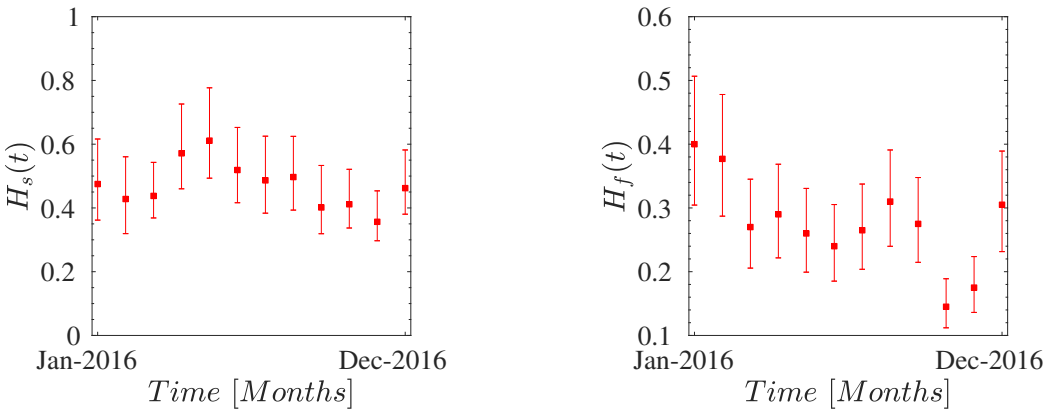

Figure 4.16:
Monthly variation of H_s coefficient (left panel) and for H_f (right panel) of CO_2 obtained from PSD slope $\beta = 2H - 1$.

The H_s and H_f values in each sub-interval were calculated, also, through the classical bootstrap method[111]. The bootstrap method is a computer-based technique that mimics the core concept of random sampling from a set of numbers. Thereby they estimates the sampling distribution of any virtually computed statistic from the sample. The bootstrap allows to estimate the precision of sample statistics, such as medians, variances, percentiles, or, as in this case the value of the slope of PSD in the two different time scales. This is made to through a linear fit, drawing randomly with replacement from an available datasets. Each points represent the 50^{th}-percentiles of each daily distributions interval. The error bar on these measures turns out to be large as bootstrap prediction intervals considered, which provides a distribution of values at the range of a 97% prediction interval. It is important to note that, although the error bar is large, the particular modulation pattern of H_s found above is also present using this calculation methodology, as it is the almost constant trend of the H_f coefficient.

4.2 Intermittency effects in GHG tracers

The structure function analysis is the standard method used to identify scale dependent properties in physical phenomena [31]. The general q-th order structure function is defined as $S_q = \langle |x(t+l) - x(t)|^q \rangle \propto l^{\zeta_q}$ where q defines the moments and l is the scale on which the fluctuation is calculated. The parameter ζ_q is the

scaling exponent and the relation to the exponent H, in classical Kolmogorov theory (e.g. Brownian motion with $H = 1/3$) [31], is $\zeta_q = qH$, when small scale intermittency effects are not taken into account[112]. The moments q define fundamental parameters of the physical phenomena under investigation: q=1, $\zeta_1 \equiv H$ and for n=2 the scaling exponent is directly related to slope of power spectral density (PSD) through the relation $2H + 1 = \beta - 1$, where β defines the slope of the PSD, and $2H = \zeta_2$. The structure functions for $f(t)$ components for CO_2 (left panel), CH_4 (right panel) and CO (bottom panel) of $q = 1 \rightarrow 5$ for 01-Jan-2016 are reported in fig.4.17.
A potential power law in the small scale range $t \in [10, 80]$ sec is observed in all samples. This methodology applied on each sub-interval allows the extrapolation of the daily average exponents ζ_1 in order to define a seasonal pattern. Exponents ζ_1 for CO_2 $f(t)$ (left panel) and CH_4 $f(t)$ (right panel) are reported in fig.4.18. The average value of ζ_1, which is equivalent by definition to H, is reported as dashed line in fig.4.18. The values observed are 0.34 ± 0.07 for CO_2, 0.28 ± 0.05 for CH_4 and 0.59 ± 0.03 for CO. The behaviour of ζ_q as a function of moments q for $f(t)$ component obtained for CO_2 (left panel), CH_4 (right panel) and CO (bottom panel), is reported in fig.4.19. The discrepancy of exponents from the classical K41 prediction[31], increases as q increase for both CO_2 and CH_4, indicating a non-linear dependence on moments q.

A linear (monofractal) scaling exponents ζ_q correspond to a self-similar structure [31], but the non-linearity of ζ_q indicates multifractal behaviour which can be defined by quantifying the deviation from K41 law. For CO_2 and CO is observed a stronger discrepancy depending on period of the year. In fact, for CO_2, November is the month that presents stronger deviation due to large fluctuation concentrations. A similar behaviour is observed for CO where spring/summer months are the most intermittent.
However, the fact that ζ_q is non-linear indicates that intermittency exists in the datasets[113]. In order to quantify the level of intermittency, it is possible to fit the exponents ζ_q as a function of q with the relation

$$\zeta_q = qH - \frac{\mu}{2}(q^2 - q). \tag{4.8}$$

where μ represents the intermittency parameter obtained from a simple log-normal cascade model[114]. In other words, quantifying the deviation from K41, by calculating the intermittency parameter μ, corresponds to define how much a dataset is more or less intermittent (in a Kolmogorov sense). Therefore, a high

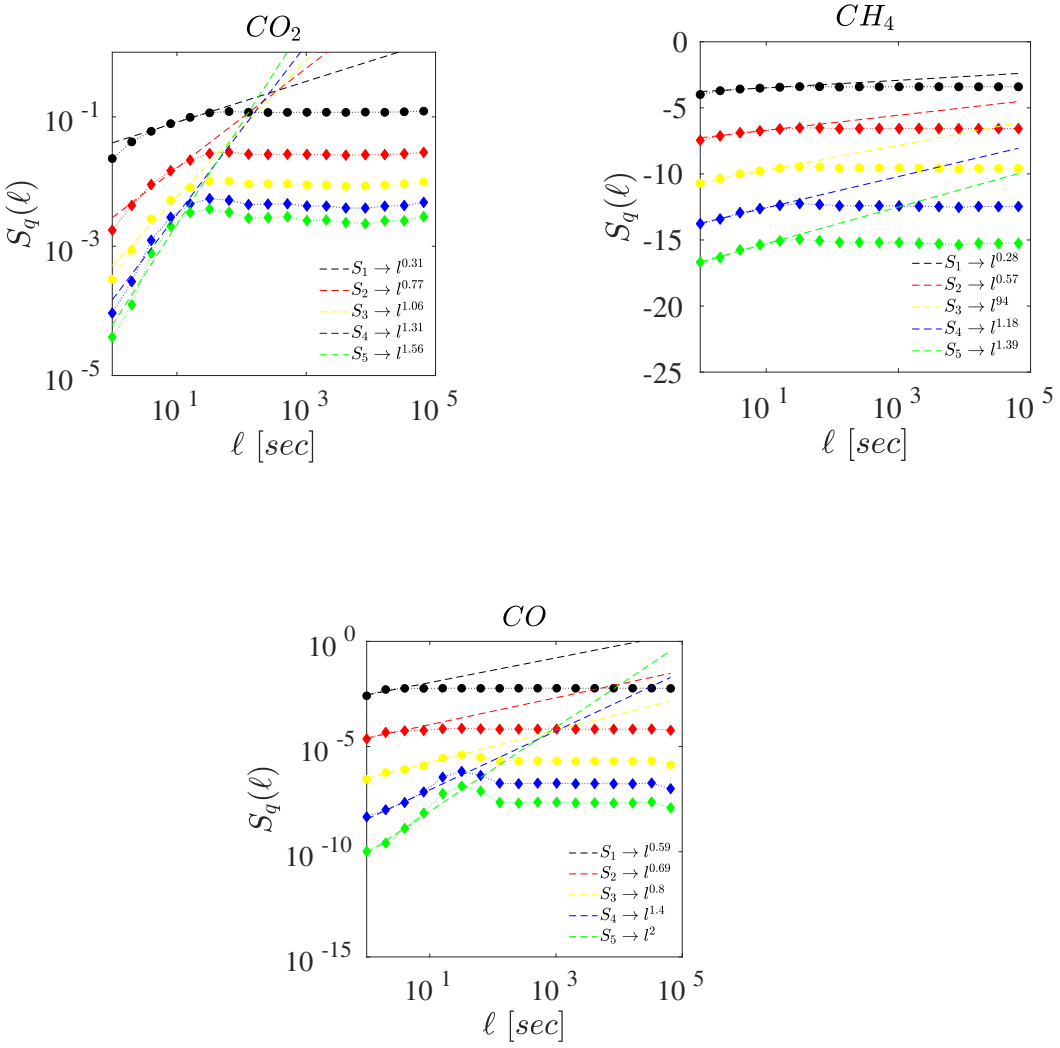

Figure 4.17:
Plot of structure function of $f(t)$ component for CO_2 (left panel), CH_4 (right panel) and CO (bottom panel). The all dotted lines represent the fit of various S_q in a small scale range.

value of μ corresponds to a higher degree of intermittency. Fig.4.20 shows the values of μ_f for $f(t)$ component of CO_2 (left panel) , CH_4 and CO, where it can be seen that the effects of intermittency are present in all three cases and differ from month to month. The mean values of μ_f, for all three cases, are comparable with the value found in fluid turbulence [52],[115],[58], where the mean value μ_f is slightly higher than that of the isotropic case $\mu \approx 0.02$.

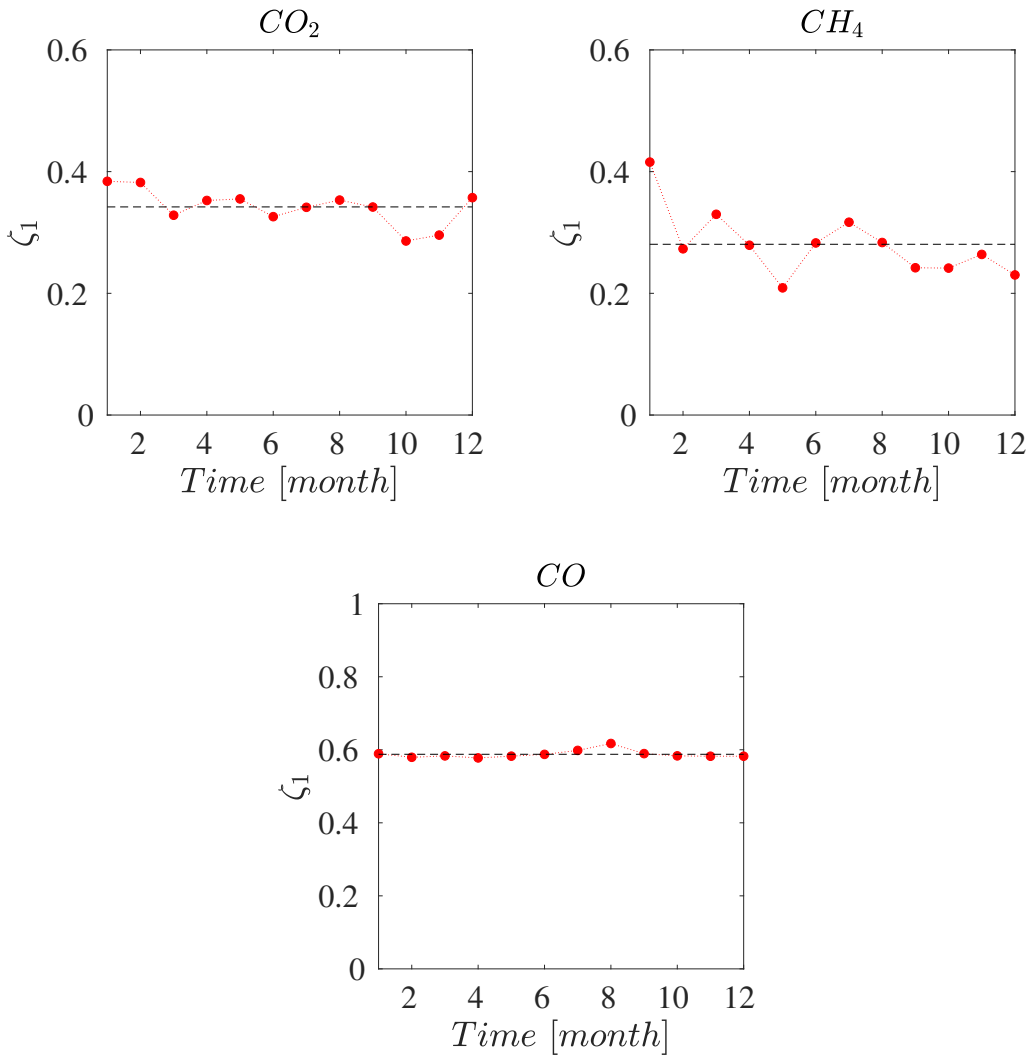

Figure 4.18:
Monthly variation of ζ_1 of $f(t)$ component for CO_2 (left panel), CH_4 (right panel) and CO (bottom panel). Dotted lines represent the $\langle\zeta_1\rangle$ 0.34 ± 0.07, 0.28 ± 0.05 and 0.59 ± 0.03 respectively.

In fig.4.21 are shown the structure functions for the $s(t)$ component. Also in this case a power law of S_q, in function of l over a larger range of scales $t \in [200, 21600]$ sec is observed. The values of ζ_1 are shown in Fig.4.22, where the mean values are 0.38 ± 0.03, 0.48 ± 0.02 and 0.28 ± 0.01 for CO_2 (left panel), CH_4 (right panel) and CO (bottom panel), respectively.

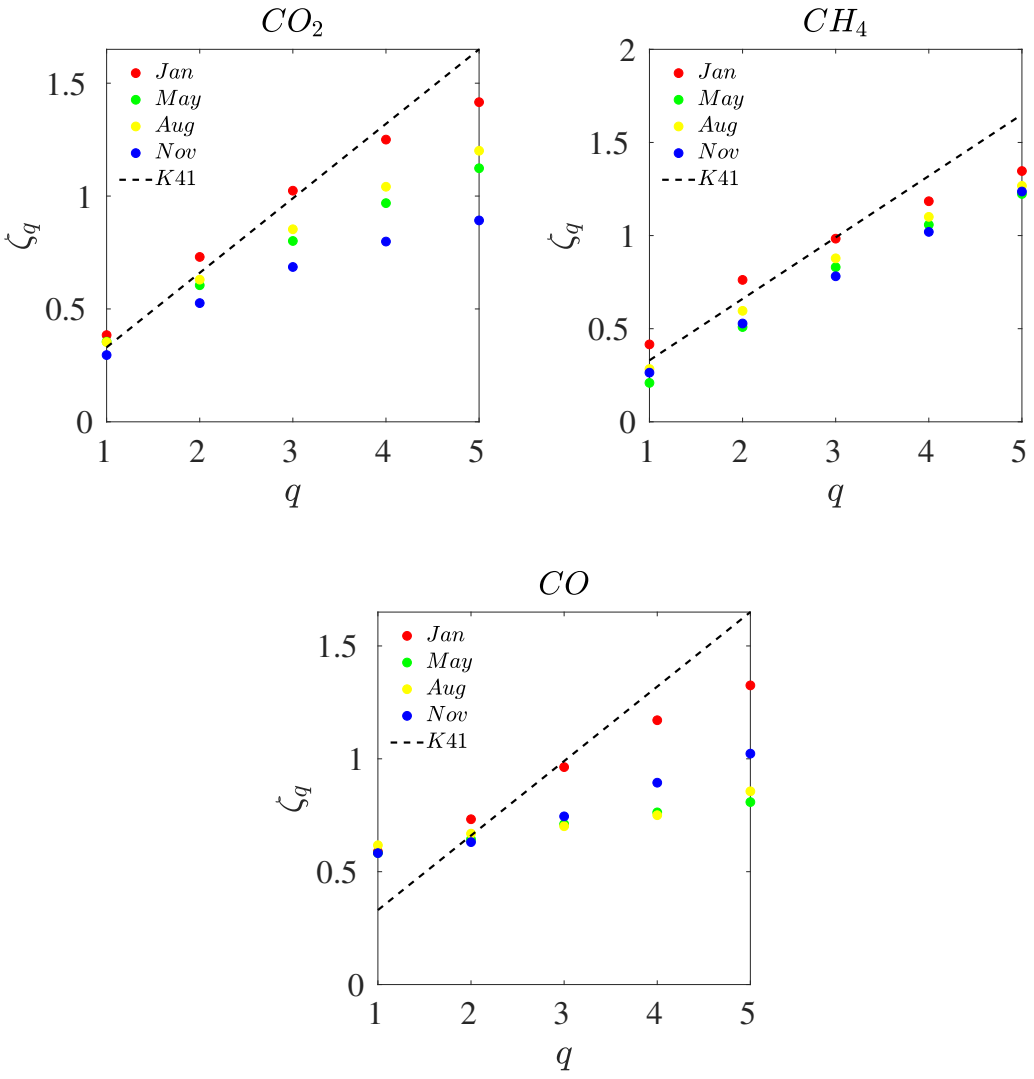

Figure 4.19:
Behaviour of scaling exponents ζ_q of $f(t)$ component for CO_2 (left panel), CH_4 (right panel) and CO (bottom panel) for January (red dots), May (green dots), August (yellow dots) and November (blue) datasets. Dotted lines represent the K41 law.

Also in this case, as already seen, the exponent H_s for CO_2 presents a temporal evolution in which the maximum is in spring and the minimum in winter. On the other hand CH_4 and CO present a constant temporal evolution. The mean values of H_f and $H_s(t)$ for CO_2 are almost equal within error limits, where they are equal to 0.34 ± 0.06 and 0.38 ± 0.08, respectively. However, even if the average is similar to the slow temporal distribution of H_s and highlights the multi-scale nature of phenomenon. The exponents of ζ_q, as a function of moment for $s(t)$ are shown in fig.4.23 for CO_2 (left panel), CH_4 (right panel) and CO (bottom

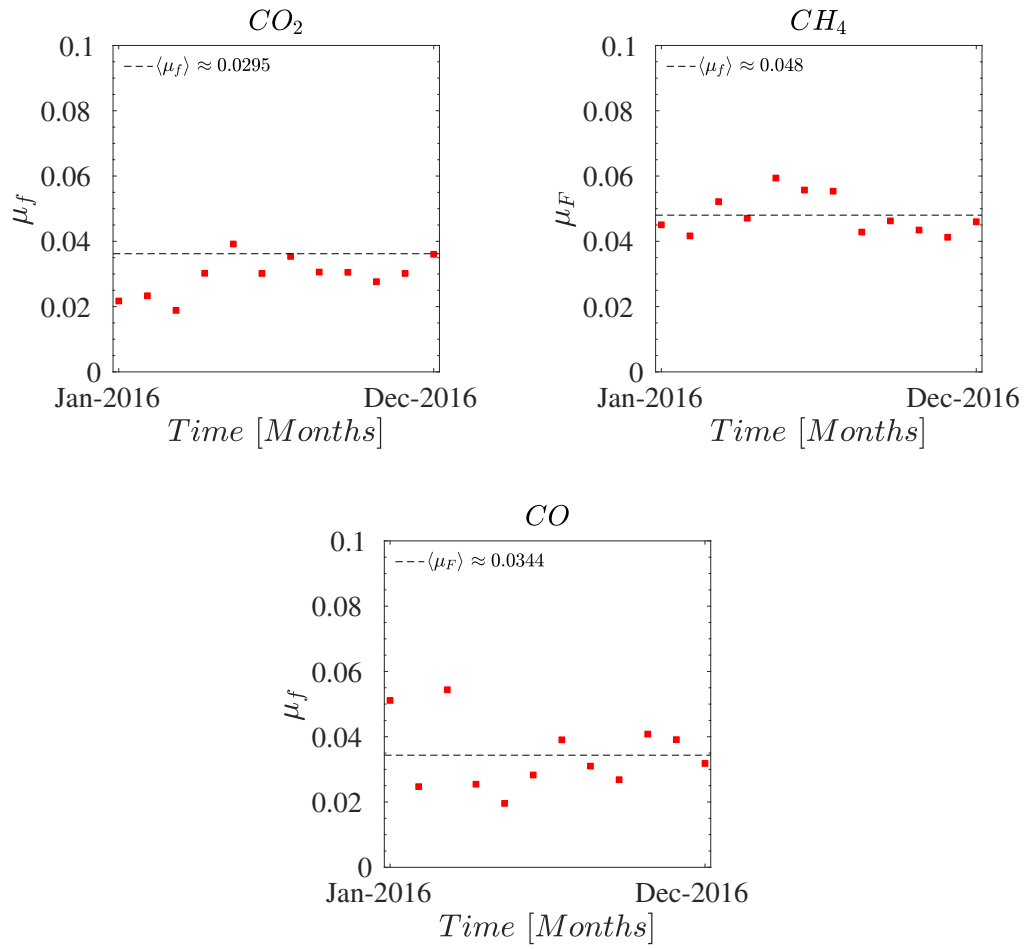

Figure 4.20:
Intermittency parameters estimated via the log-normal model for $f(t)$ components. The dashed lines represents the mean value $\langle \mu_f \rangle$ that is equal to 0.0295, 0.048 and 0.0344 for CO_2, CH_4 and CO respectively.

panel).

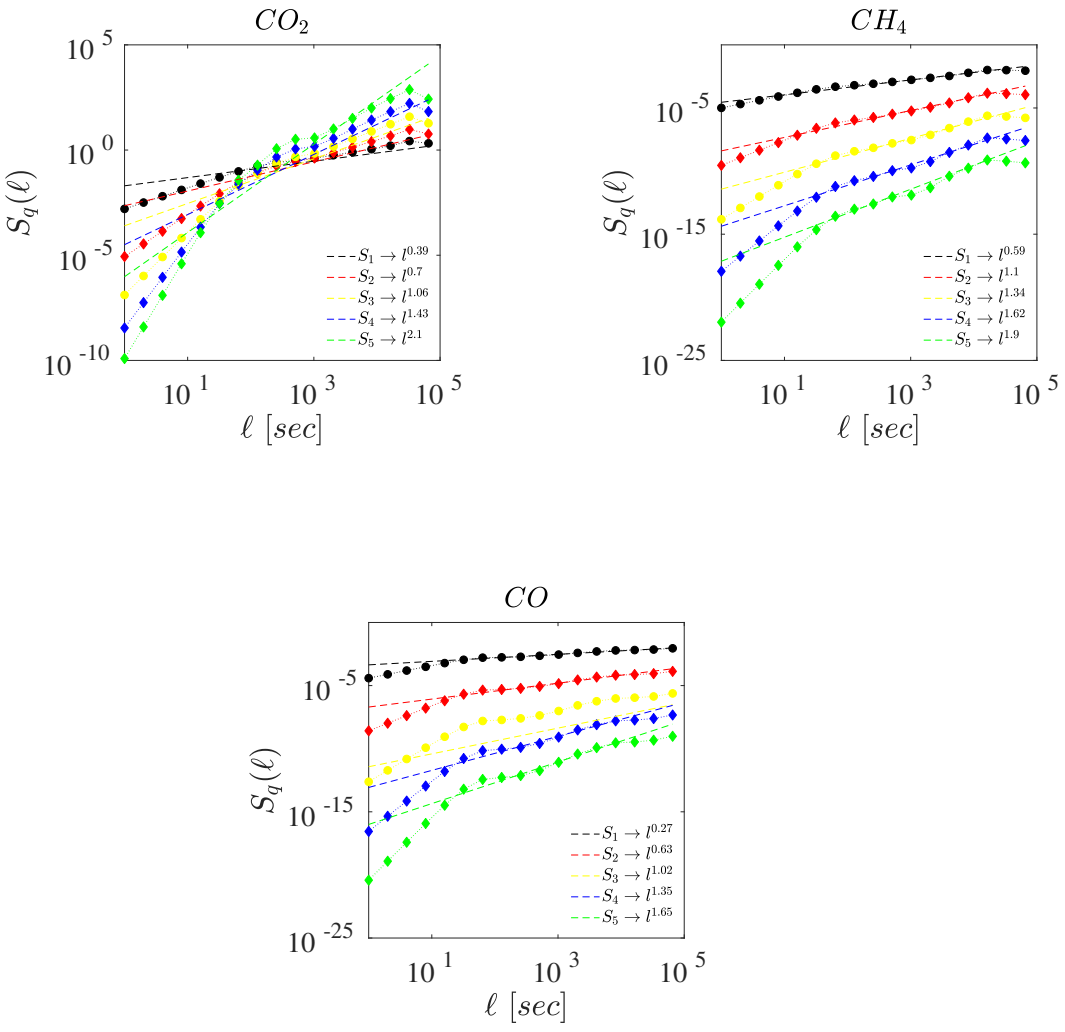

Figure 4.21:
Plot of structure function of $f(t)$ component for CO_2 (left panel), CH_4 (right panel) and CO (bottom panel). The all dotted lines represent the fit of various S_q in a large scale range.

As for the $f(t)$ component, the behaviour of ζ_q deviate from the K41 in all cases. Moreover the discrepancy is again seasonal dependent The behaviour of the intermittency parameters μ for the three cases are shown in fig.4.24, where the intermittency effects are comparable with the isotropic case $\mu_s \approx 0.02$.

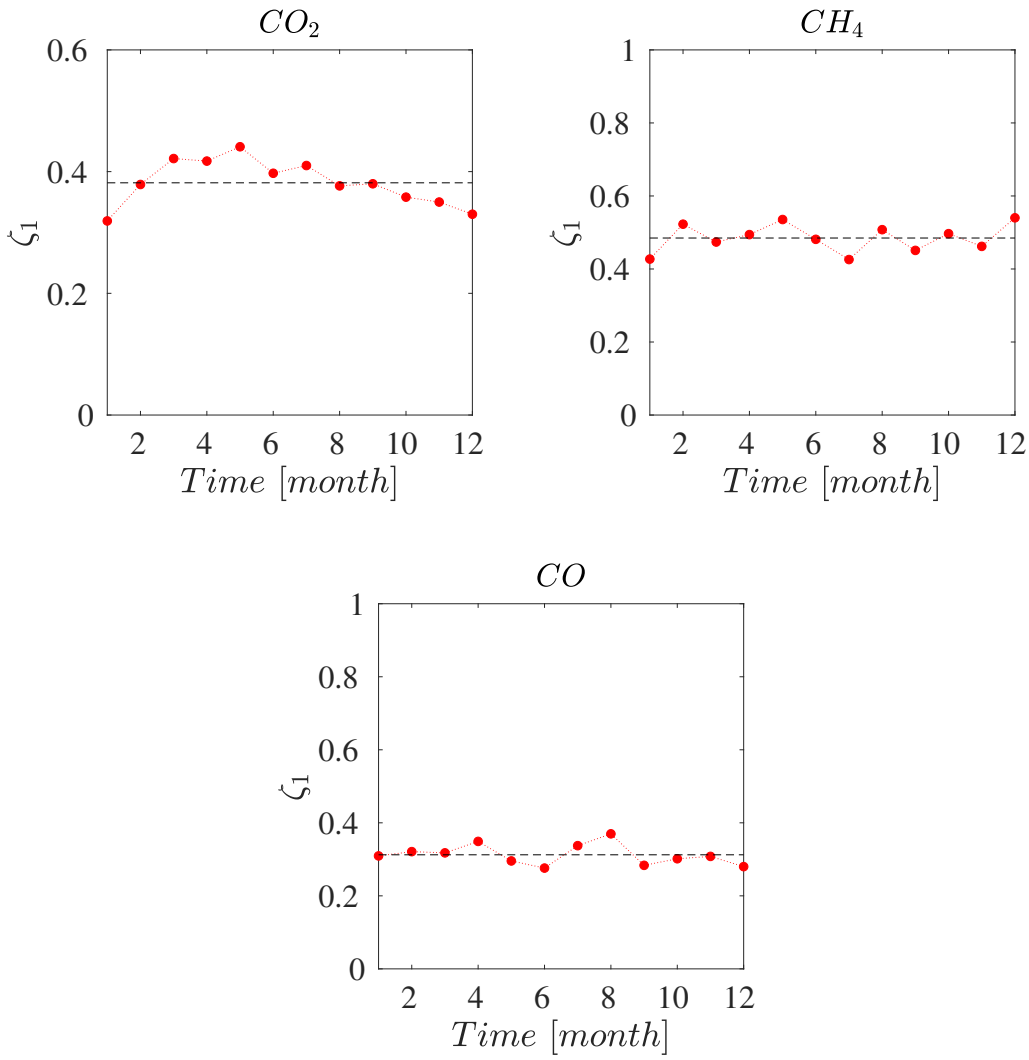

Figure 4.22:
Monthly variation of ζ_1 of $s(t)$ component for CO_2 (left panel), CH_4 (right panel) and CO (bottom panel). Dotted lines represent the $\langle\zeta_1\rangle$ that are 0.38 ± 0.03, 0.48 ± 0.02 and 0.28 ± 0.01 respectively.

To confirm the fact that the $f(t)$ component of CO_2 and CH_4 is related to atmospheric turbulence phenomena, it is possible to compare the annual average values of ζ_q with those found in the literature, concerning atmospheric turbulence in a turbulent boundary layer[116], [117]. In tab.4.1 are reported the classical values of ζ_q and the annual average of the GHG tracers. ζ_q values of $f(t)$ for CO_2 and CH_4, of the first q moments, are comparable with the classical ones. However, the higher orders differ significantly, and is an indication that these datasets are much more intermittent. Different discussion for the $s(t)$

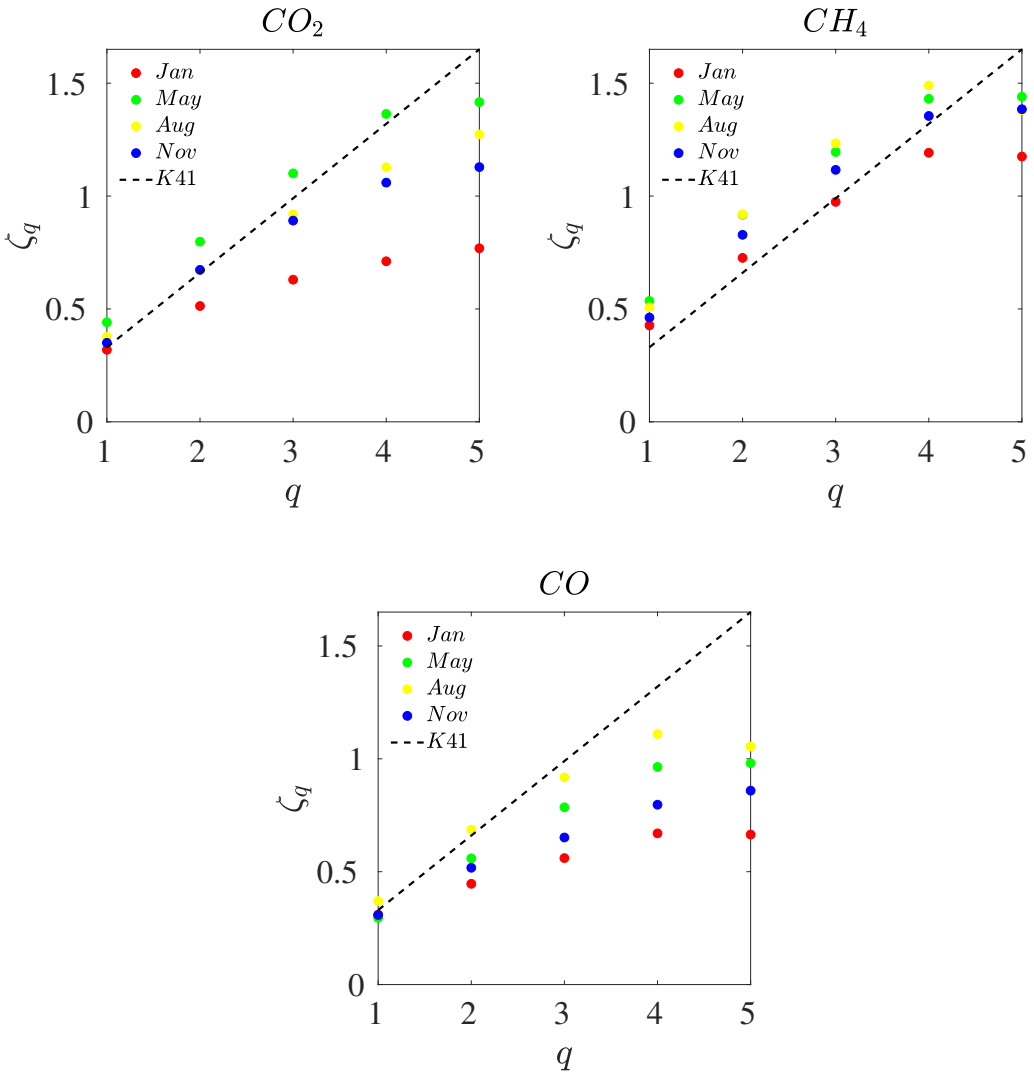

Figure 4.23:
Behaviour of scaling exponents ζ_q of $s(t)$ component for CO_2 (left panel), CH_4 (right panel) and CO (bottom panel) for January (red dots), May (green dots), August (yellow dots) and November (blue) datasets. Dotted lines represent the K41 law.

component, in which ζ_q are slightly different respect both $f(t)$ and the classic ζ_q, indicating that the dynamics of the $s(t)$ are a different nature respect the $f(t)$ component. The small difference between the mean annual values to the classical values of turbulence ζ_q is due to the fact that, on average, the most common effects are those related to turbulent fluid motion. On the other hand, the two dynamics temporal evolution are different.

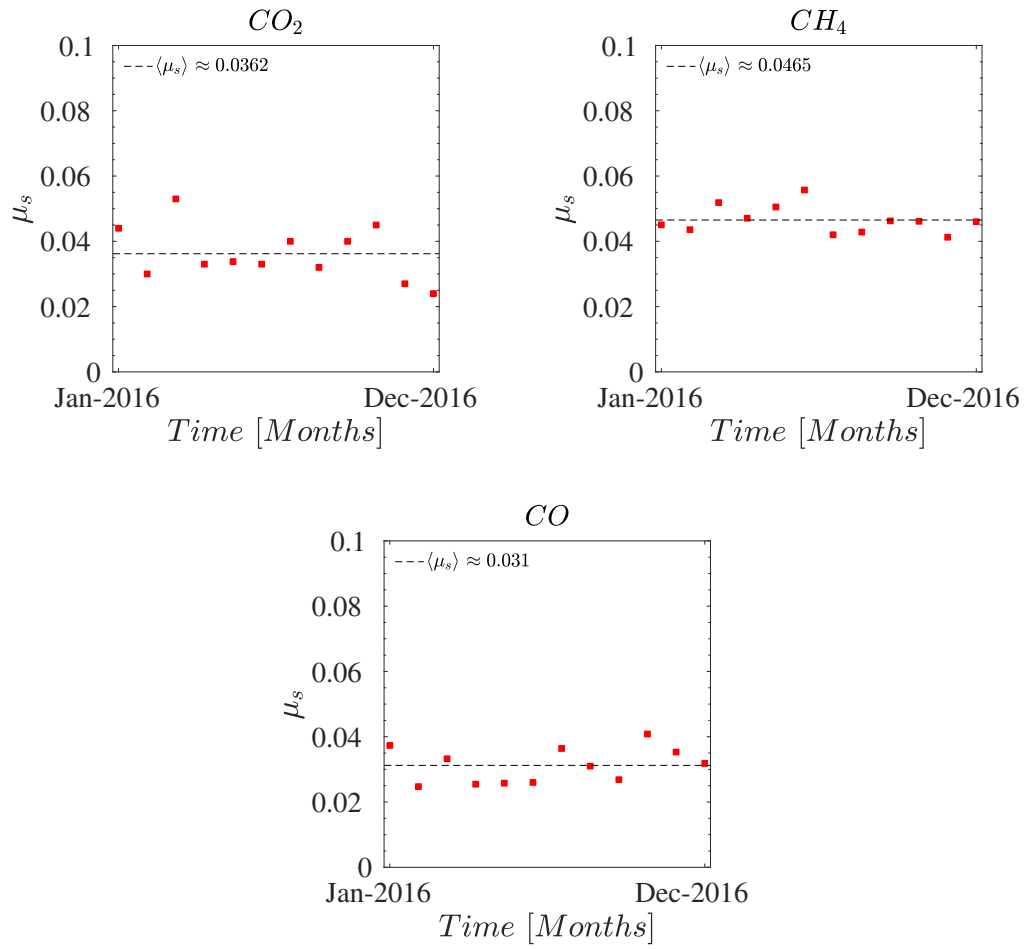

Figure 4.24:
Intermittency parameters estimated via the log-normal model for $s(t)$ components. The dashed lines represents the mean value $\langle\mu_s\rangle$ that is equal to 0.0362, 0.0465 and 0.031 for CO_2, CH_4 e CO respectively.

q	Ruiz[116]	Schimtt[117]	$\langle\zeta_s\rangle_{CO_2}$	$\langle\zeta_f\rangle_{CO_2}$	$\langle\zeta_s\rangle_{CH_4}$	$\langle\zeta_f\rangle_{CH_4}$	$\langle\zeta_s\rangle_{CO}$	$\langle\zeta_f\rangle_{CO}$
1	0.37	0.35	0.34	0.38	0.48	0.37	0.31	0.59
2	0.71	0.7	0.62	0.68	0.84	0.67	0.56	0.66
3	1	1.01	0.83	0.9	1.11	0.94	0.73	0.77
4	1.28	1.3	1.04	1.09	1.34	1.11	0.9	0.86
5	1.53	1.52	1.15	1.16	1.31	1.23	1	0.96

Table 4.1:
Values of classical ζ_q (first two columns) [116],[117] and experimental annual mean value ζ_q found for $f(t)$ and $s(t)$ for CO_2, CH_4 and CO of 2016.

Furthermore, the decomposition applied may have changed the behaviour of the fluctuations in the two components, compared with the original signal in the two different time scales. To verify that this decomposition does not change the

pattern of fluctuations, it is possible to calculate the scaling exponent $\zeta_{c,q}$ (where c indicates the complete datasets) of the structure function on the various days, already done previously, and then averaging them monthly. In fig.4.25 the ratio $\zeta_1/\zeta_{c,1}$ of the $s(t)$ component of the three GHG tracers in the large time range is shown. The ratio in each case is $\zeta_1/\zeta_{c,1} \approx 1$, indicating that the decomposition performed does not change the scaling of the fluctuations.

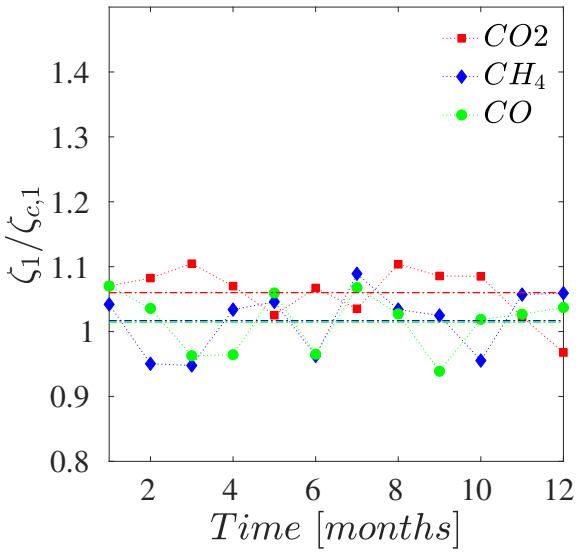

Figure 4.25:
Variation of ratio between ζ_1 and $\zeta_{c,1}$ for $s(t)$ components. In all three case this ration is about one, that are represent by dotted lines.

4.2.1 Hurst exponent estimation via Detrended Fluctuation Analisys

A more sophisticated methods for estimation of the exponent H is the detrended fluctuations analisys (DFA), such method has been applied to every sub-interval for the three years of sampling. In fig.4.26 are reported the fluctuation functions, $F_f(\ell)$, for the $f(t)$ (red circles), and $F_s(\ell)$ for the $s(t)$ (blue squares) components of the CO_2 (first row left panel), CH_4 (first row right panel) and CO (second row left panel), respectively. The $F(\ell)$ calculated for one sub-interval of original datasets of CO_2 is reported in the last panel.

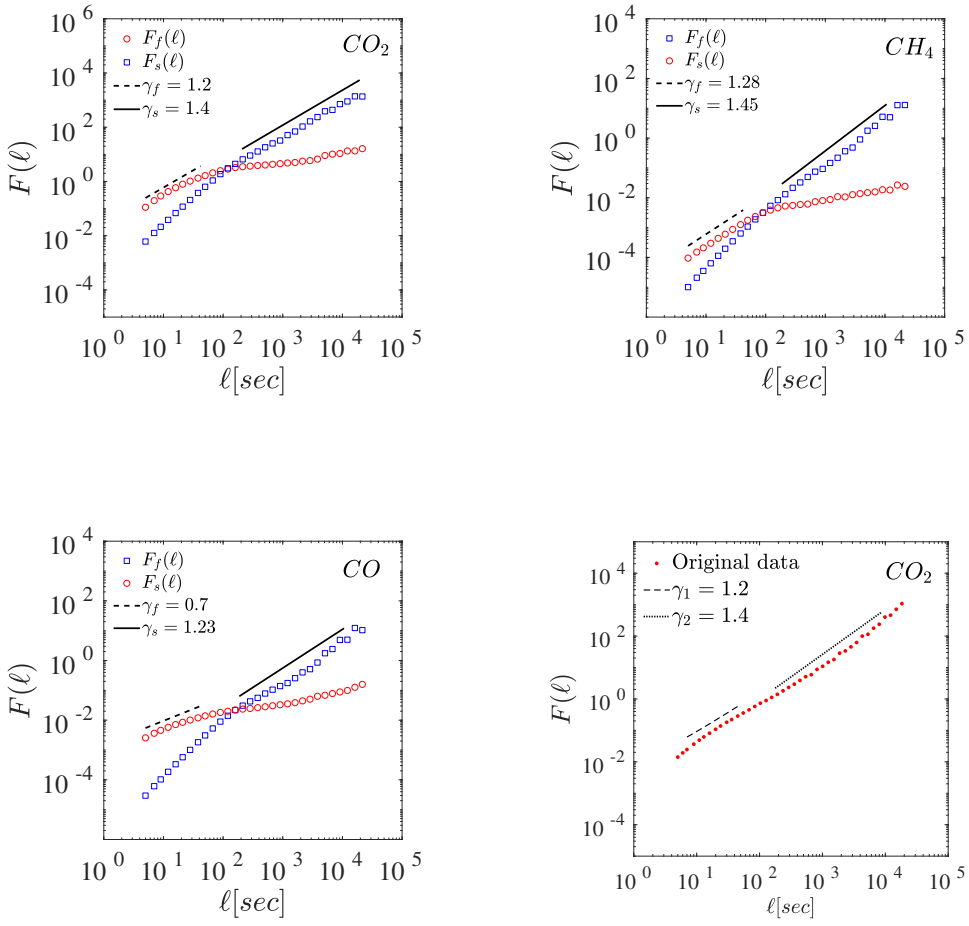

Figure 4.26:
Log-log plot of $F(\ell)$ vs ℓ for separate components of CO_2, CH_4 and CO. The dashed line represents the liner fit computed in the two range of temporal scales, in the legend are shown the values of the slope of these line. In the last panel is presented the $F(\ell)$ of the CO_2 original data where the dashed line represent the value of the scaling exponent in the two range of temporal scale. The value of γ_1 and γ_2 are the same as those found in the same ranges as the separate components.

Applying the DFA method to the $f(t)$ and $s(t)$ components separately yields two different scaling exponents, γ_f for $f(t)$ component and γ_s for the $s(t)$. In other words each component exhibits two different scaling behaviours depending on the range of scales. For the DFA method given $F_q(\ell) \sim \ell^{\gamma}$ is possible to extrapolate the value of γ, which is $H(q = 2) = \gamma$.

Two range of scales were identified: the small time scale $t \in [10, 80]$ sec and the large time scale $t \in [200, 21600]$ sec (such values can slightly varies depending on the particular day, due to particular meteorological and climate conditions). However, the behaviour of $F_f(\ell)$ at small scale and $F_s(\ell)$ of $s(t)$ at large scale overlap perfectly with $F(\ell)$ presented in fig.4.26 (second row right panel) of original data, (in which is represented only CO_2, because the behaviour of CH_4 and CO is equal). The values of the two exponent scaling γ_1 and γ_2 found correspond to the values of γ_f and γ_s, respectively.

The behaviours of $F_f(\ell)$ and $F_s(\ell)$ are intrinsically connected to the method of selection of the components which, being a partial sum of various IMFs $\phi_j(t)$, extrapolated from the original signal, present behaviours at increasing frequencies and periods. Since the scaling exponents γ of the original signal and those of $s(t)$ and $f(t)$ are comparable, indicates that the partial reconstruction employed here does not modify the characteristic structure of the fluctuation dynamics. In the other hand, variations are observed in the scale ranges that do not belong to the partial sums; for example, for the reconstruction of the $f(t)$ component, variations are observed at low scales and vice versa for the $s(t)$ component. The decomposition presented here provides a clearer view of the behaviour on different timescales, and on different datasets.

The components $s(t)$ and $f(t)$ overlap at a scale $l \approx 200$ sec, corresponding to the value between the period of the last $\phi_j(t)$, considered in the partial summation used in the reconstruction of $f(t)$ and the period of the first $\phi_j(t)$ considered for $s(t)$. However, although four different scaling behaviours can be defined four respective γ, the only significant γ, for the purpose of the work, are γ_f and γ_s and correspond to the values of γ of the $F_f(\ell)$ at small scales and the $F_s(\ell)$ of $s(t)$ at large scales. The other two γ exponents, referred to $F_f(\ell)$ at large scales and to $F_s(\ell)$ at small scales, which are consistently equal to $\gamma_s \sim 2$ and $\gamma_f \sim 0.3$, are not significant, since, as mentioned earlier, changes in the two components are noticeable on different time scales.
For both CO_2 fig.4.26 (first row left panel) and CH_4 fig.4.26 (first row right panel), the values of γ_f and γ_s are greater than 1. Considered that the γ is greater than 1, the fluctuations dynamics of CO_2 and CH_4 are strongly per-

sistent in nature with a non-stationary behaviour [51], and they are positively correlated at both small and large scales.

This strong persistence of CO_2 and CH_4, on all time scales, indicates that the signal is positively correlated in a power-law fashion (as seen in the previous section), where the autocorrelation function ACF defined as: $ACF(\tau) \equiv \langle x(t)x(t+\tau)\rangle$ where $x(t)$ is the signal and τ is the variable temporal lag. The ACF represents the correlation of the original function at time instants delayed by a time τ. If the autocorrelation function rapidly goes to 0, it means that the subsequent data values cannot be predicted with success from neighboring values, and the system loses the memory of the process. If it does not vanish quickly, the behavior of the function is less random. From the value at lag 0 one can estimate possible values at future times with better success. For example, if the data are periodic with period T, after one period T one can make reasonable estimate what the next values will be, and the autocorrelation function comes out also periodic. If the process under analisys is a Brownian motion without correlation (H=0.5), the next values are hard to predict successfully, and the autocorrelation function decays very fast (usually exponentially, the width of the exponential is a measure of the decorrelation time). In other words, the autocorrelation is a measure of how deterministic the system dynamic is. A perfectly deterministic system will always have a normalized ACF of '1', while a perfectly random system will have have an ACF that looks like a delta function. For real systems where dissipation, or sources and sinks are present, the autocorrelation function will generally presents a decay slower than an exponential function, usually the decay assumes a power-law fashion. This behavior indicates the complexity of the phenomena under study, where the "mixing" of multiple compartments can reinforce correlation effects on multiple time-scales. Considering a monthly time interval it is possible to verify the positive correlation that exists in the time series of CO_2 (left panel), CH_4 (Right panel) and CO (bottom panel), as shown in fig.4.27. Thus the behaviour of ACF indicates a slower and not exponentially decay of concentration[23]. The auto correlation functions and their behaviour agree with the values of the H exponents found, since the value of the slope of the ACF function is specifically the H coefficient that defines the memory or not of the fluctuations in the signal. In fact, for both CO_2 and CH_4 the ACF of the component $s(t)$ (black line) mimics behaviour of the ACF of the original signal, indicating that a large portion information is contained in this slow component, as seen in the previous section, unlike the $f(t)$ (red line). Despite ACF is persistent, it presents a sudden fall as a noise in

the signal. In other words, CO_2 and CH_4 are defined by long-range correlations in which long time lags fluctuations maintain memory of the previous ones, and this is inherently present in the $s(t)$ component. However, fluctuations in $f(t)$ at large time lags have no memory of previous ones causing the ACF to decay very quickly. Then it fluctuates around zero and, for small temporal scales, it does not come down immediately to zero. For the CO the behaviour of the component $f(t)$ compared to the other two cases has a much faster decay. Having a low lifetime it has not a memory on short time scales, and this is the reason why the memory is lost. On the other hand, the $f(t)$ component loses memory completely after a certain time, that is, when it goes to zero, and in some cases it is seen to become anti-correlated.

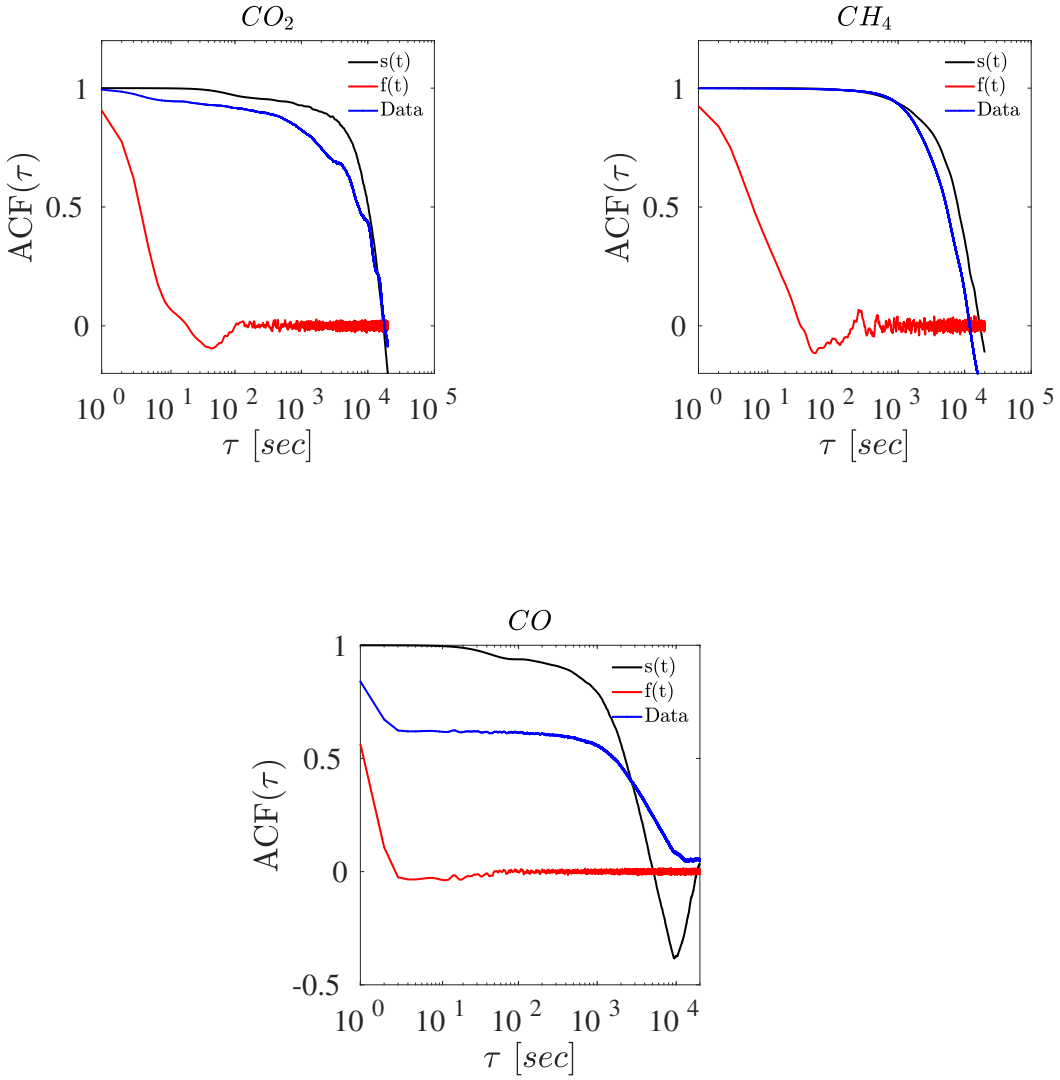

Figure 4.27:
Semi-log plot of autocorrelation function of dataset (blue line), $f(t)$ (red line) and $s(t)$ (black line) for CO_2 (left panel), CH_4 (right panel) and CO (bottom panel). Since, both at small and large scales, these three concentrations turn out to be positively correlated, in this case has been chosen to take an interval of monthly length, always sampled at high frequency with $\Delta t = 1sec$, to better show how ACF has a slower decay.

4.3 Temporal evolution and and seasonal behaviour for Hurst exponent

The monthly evolution for H_f, estimated through DFA method, is reported in fig.4.28 for CO_2 (left panel), CH_4 (right panel), and CO (lower panel), respectively, where error bars represent the 95% confidence bounds. The monthly values represented in fig.4.28 and fig.4.29 were calculated as an average of the individual values extracted from each daily sub-interval. It is interesting to see that, if for the $f(t)$ component of the three GHG traces, there is no particular pattern in the behaviour of the H_f.

The mean value of H_f for CO_2 and CH_4 is comparable with the value of H in turbulence [113], [58]. In fact, as analysed before, since $f(t)$ is the turbulent component present in the signal, the variation of fluctuations on short time scales are related to wind velocity that transports molecules from one region to another. For CO instead also the resulting H_f values are in line with what has been said. In fact the CO has a low variability [118] than CO_2 and CH_4, as well as having a short lifetime causing the stationarity of the $f(t)$ with a higher H_f coefficient than that of CO_2 and CH_4. In addition, the range of periods used to define $f(t)$ is within the noise part of the modes, which results in a noise-like signal structure that justifies the values of the H coefficient. This can also be seen when the H coefficient was calculated with the variance of the IMFs since the trend is decreasing.

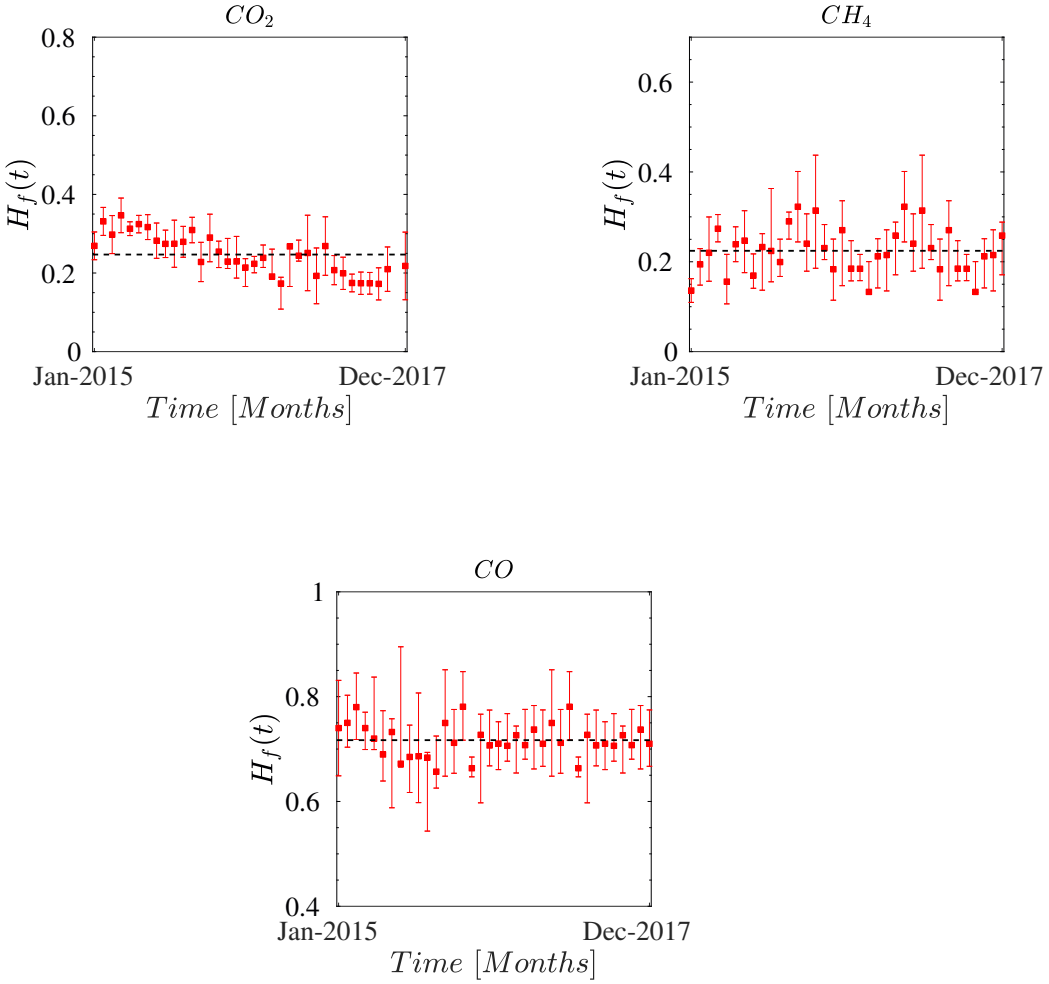

Figure 4.28:
Left panel and **Right panel**: variation of average monthly Hurst exponent H_f of CO_2 and CH_4 time series per second recorder at Monte Curcio respectively, with the associated 95% confidence bounds. Dashed line represent the H_f average that is 0.23 and 0.229 respectively for CO_2 and CH_4. **Bottom panel**: variation of average monthly Hurst exponent H of fast $f(t)$ component of CO. Dashed line represent the H average that is 0.72

The monthly variation H_s of $s(t)$ for CO_2 (left panel), CH_4 (right panel), CO (bottom panel) are represented in fig.4.29. $H_s(t)$, for CO_2, presents a intra-year time dependent pattern. This pattern is defined by a minimum in the winter season, followed by a subsequent increasing during spring season and finally reaching a maximum during summer season, particularly in July, before decreasing again in autumn. For component $s(t)$ of CH_4, H_s seems to have a phase lag of six months with respect to the CO_2 modulation. For CO the

behaviour of H_s coefficient is flat which is compatible with that of turbulence. So probably the fluctuations seen on long timescales in CO are a surrogate in some way for the turbulent motion of the atmosphere.

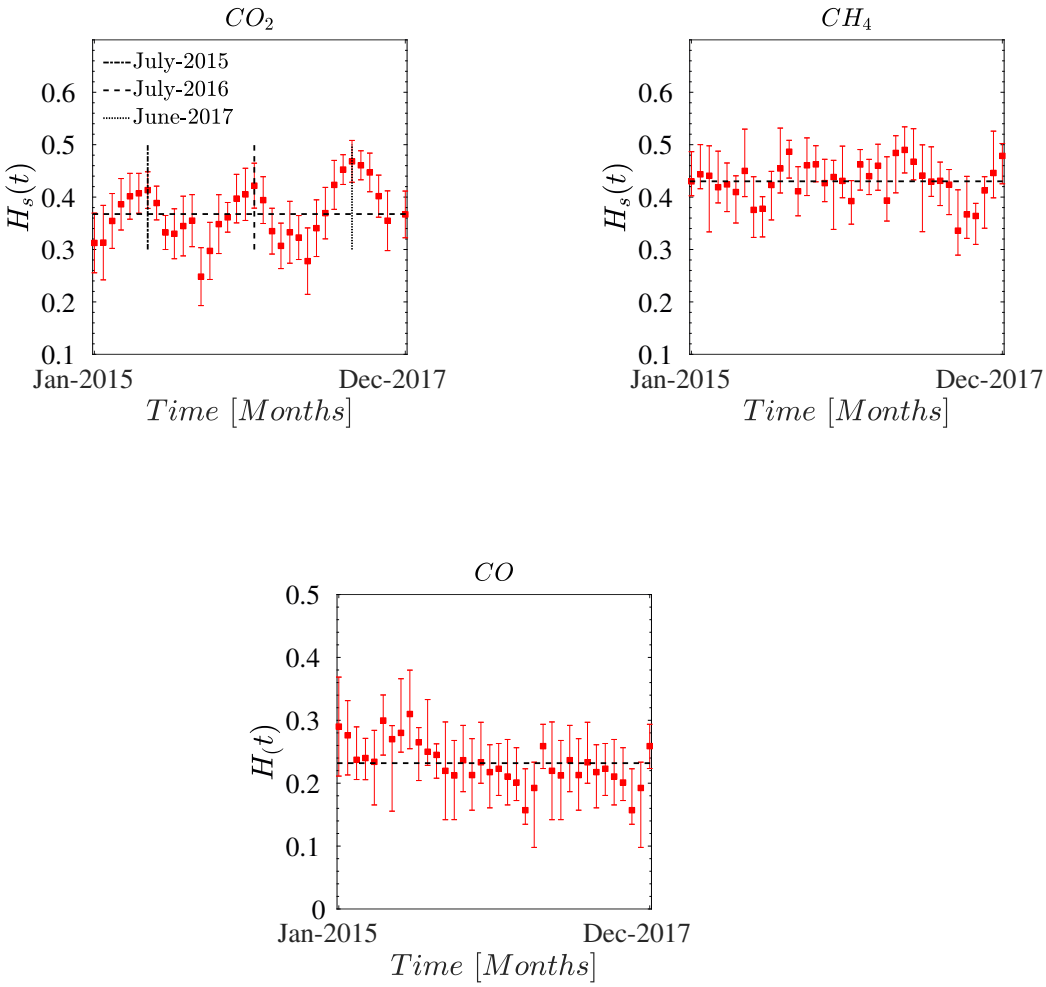

Figure 4.29:
Left panel: variation of average monthly Hurst exponent H of slow $s(t)$ component of CO_2 time series per second recorder at Monte Curcio respectively, with the associated 95% confidence bounds. The horizontal dashed line represents the average H equal to 0.367 and the vertical lines are the calculated maximums. **Right panel** and **bottom panel**: variation of average monthly Hurst exponent H_s of CH_4 and CO respectively. Dashed line represent the average H_f for CH_4 and CO that equal to 0.438 e 0.21 respectively.

On average, winter concentration presents more fluctuations in the $s(t)$ than the summer concentration, where the amplitude of fluctuations are smaller, making the value of H_s higher. To validate the existence of a modulation pattern in the behaviour of the H_s coefficient, as well the behaviour of H_f, it is possible to extrapolate the slope values by calculating the distributions of probability density function of the H_s and H_f through the bootstrap method. In this case are evaluated the values of $F_{2,s}(\ell)$ and $F_{1,f}(\ell)$ slopes, namely $1\gamma_f$ and γ_s in the two different time scales through a linear fit.

The statistical variable under consideration in this context are the slopes γ_s and γ_f, that are calculated from time to time based on the resampling done in the two different scale ranges. In this way it is possible to define a probability density functions (PDFs) of the values of the coefficients H_s and H_f, in terms of γ, and not a unique ones as previously extrapolated. In fig.4.30 are reported the PDFs of the Hurst exponents H_s and H_f for CO_2 for January, May, July and October.

In each panel these PDFs are compared in order to verify whether these distributions are different or overlapping, in order to define the validity of the modulation of the coefficient H_s. The PDFs of the H_s of the various months do not overlap within the prediction interval of 97%. They are represented by the dashed lines within the figures, where in each panel those on the left represent the 2^{nd}-percentile and those on the right the 97^{th}-percentile. The value in the central bin in each distribution represents the 50^{th}-percentile, or the median of distribution of H_s. The only overlap in the PDF, which results in an undefined difference between the two distributions, is between May (black bar) and July (blue bar) (second row right panel). In fact, as shown in fig.4.29, the values of the H_s exponents, for the two months under consideration, overlap within the confidence interval represented by the error bars. The corroboration that H_f of CO_2 has no relevant patterns in its behavior is given by the values of the PDFs of H_f. In fact, all the PDFs of H_f overlap in the prediction interval, as can be seen from fig.4.31, confirming precisely that there is no distinction between the very values of H_f of different months.

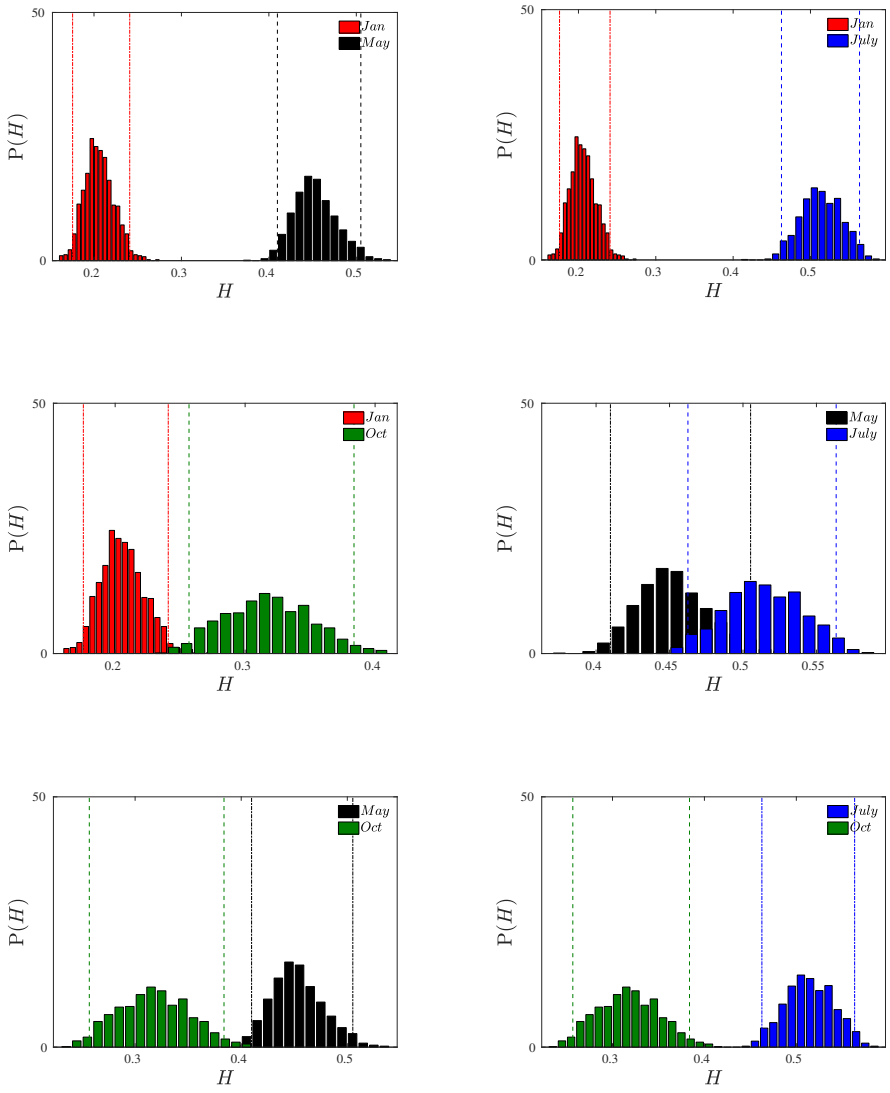

Figure 4.30:
First row: Plot of the PDFs of the Hurst exponents H for $s(t)$ component, extracted through the bootstrap method, of January vs May (left) and January vs July (right). **Second row**: Plot of the PDFs of the the Hurst exponents H for $s(t)$ component, extracted through the bootstrap method, of January vs October (left) and May vs July (right). **Third row**: Plot of the PDFs of the the Hurst exponents H for $s(t)$ component, extracted through the bootstrap method, of May vs October (left) and July vs October (right). In all panels, the vertical dashed lines represent the 97% confidence intervals.

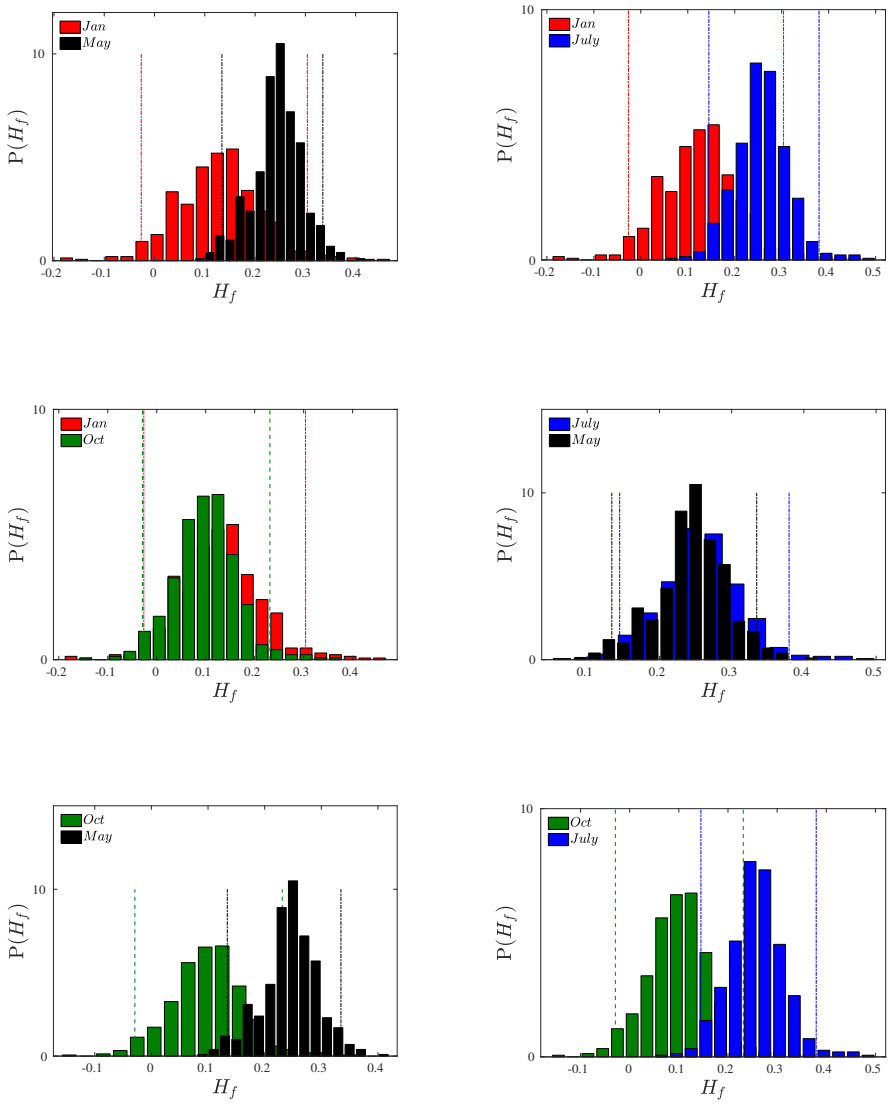

Figure 4.31:
First row: Plot of the PDFs of the Hurst exponents H for $f(t)$ component, extracted through the bootstrap method, of January vs May (left) and January vs July (right). **Second row**: Plot of the PDFs of the Hurst exponents H for $f(t)$ component, extracted through the bootstrap method, of January vs October (left) and May vs July (right). **Third row**: Plot of the PDFs of the Hurst exponents H for $f(t)$ component, extracted through the bootstrap method, of May vs October (left) and July vs October (right). In all panels, the vertical dashed lines represent the 97% confidence intervals.

4.3.1 A possible link between Environmental drivers and Hurst modulation

Accordingly with the turbulent scale invariance theory [104], modulation of H_s for CO_2 could be related to principal drivers of its dynamics. In fact, being $H_p = 5/9$ the Hurst value expected for a passive tracer transport [104], since Hs fluctuate around values greater than H_p during hot periods (spring/summer), and on values lower than Hp during cold season (autumn/winter), this behavior could be related to the source/sink seasonality. Here two distinct drivers could be taken into account, which could be the phenomena responsible for this modulation.

The photosynthesis-respiration process, defined by variation of gross primary production or photosynthetic uptake (GPP) and ecosystem respiration (RE) in the year [77], and the seasonal variation of atmospheric boundary layer height[28] are considered.

Given the correlation between GPP and EVI[119], it is possible to relate the monthly variation of EVI, and for completeness also of NVDI, with the values of the coefficient H_s. In fig.4.32 are presented the variations of H_s (green diamonds) with those of EVI (left panel) for an area of $9km^2$ (red square) and for an area of $25km^2$ (blue diamonds), and those of NDVI (right panel) for an area of $9km^2$ (red square) and for an area of $25km^2$ (blue diamonds).

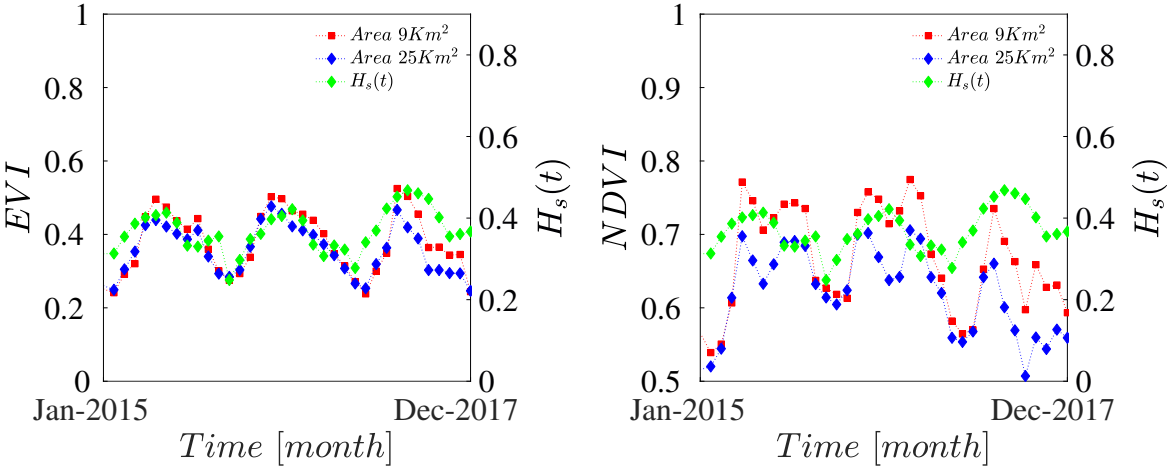

Figure 4.32:
Plot of the average monthly variation of H_s coefficient (green diamonds) and EVI index (left panel), and for NDVI index (right panel) for an area of $9 * 9Km^2$ (red square) centred on MC, and for multiple cells (blue diamonds) with area of $25km^2$ centred on MC.

Note that in the two panels in fig.4.32, the patterns between $H_s(t)$ and EVI/NDVI

(produced by the MODIS satellite [33]) have been superimposed to see that the behaviours are similar but the values of the same are different. As can be seen the modulation found in the variation of the H_s mimics the monthly variation of the EVI/NDVI (but less pronounced), with alternating minima in winter and maxima in summer. Since the H_s is an index of signal fluctuations, while EVI and/or NDVI is an index measuring the amount of vegetation, it is possible relate them by quantifying the correlation that exists between these values. So, given the cause-effect relationship, the correlation between these two variables is measured. In fig.4.33 is reported the cross-correlation as a function of the lag-time in months for EVI (left panel) and NDVI (right panel), respectively.

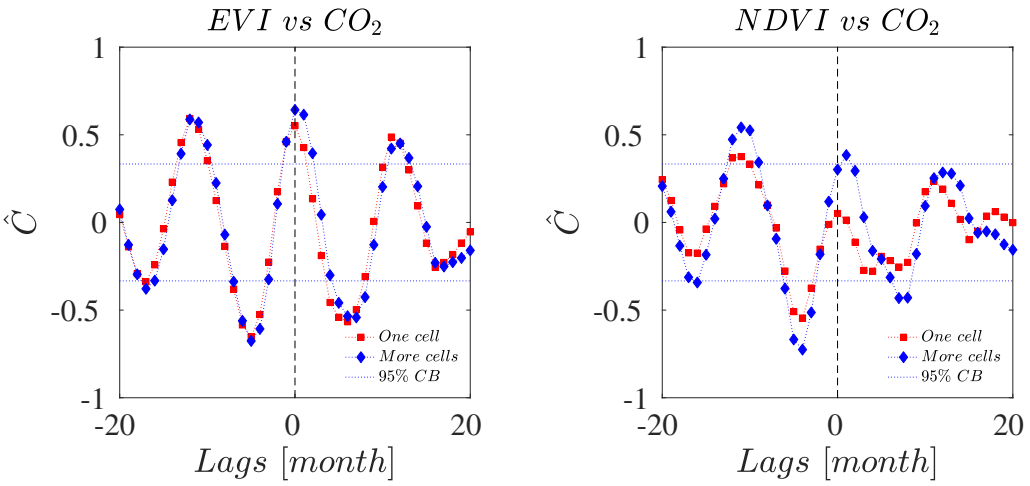

Figure 4.33:
Plot of cross correlation between monthly variation of the H_s coefficient and EVI index (left panel) and NDVI index (right panel) for an area of $9 * 9Km^2$ (red square) and for an area of $25 * 25Km^2$ (blue diamonds). The dashed lines in both panels represents the 95% confidence bounds.

So that, the strong positive correlation $\hat{C} = 0.63$ at lags 0 for H_s and EVI represent how the variation in vegetation density for both single cells or multiple cells, and thus the change rate of photosynthesis-respiration process plays a primary role in the intra-day fractal properties of CO_2. Therefore, the variation in the dynamics of $s(t)$ for CO_2 at MCU, due to physical processes that develop on a local spatial scale. The second peak of cross correlation is a lag of 12 months indicating the periodicity of process. A positive correlation shifted by one month can also be seen with the NDVI index, but since this index does not take into account the presence of strong biomass, as present at MCU, the correlation with the H_s is not well visible.

Regarding the variation of the H_s for CH_4 it is possible to notice a weak modulation. Compared to the seasonal variability of CO_2, as shown in fig.3.6, CH_4 presents a seasonal mean diurnal cycle much more pronounced in winter than in summer. This, as discussed for CO_2, causes the value of the H_s coefficient to increase relative compared to summer. Given the almost total absence of a vertical gradient, the mixing seen for CO_2 does not explain the behaviour of the H_s coefficient of CH_4. However, the seasonal periodicity of OH (one of the main oxidants of CH_4 in the atmosphere) in the northern hemisphere [88], could cause an increase of the fluctuations in the summer period with a consequent decrease of the same in the winter period. This modulates the intra-day dynamics of the $s(t)$ component of the CH_4. In addition it should be pointed out that the variation of CH_4 fluctuation amplitude (in percentage) of CH_4, is one order of magnitudes lower than CO_2.

The average value of H_s over the three years for CH_4 is higher than the values observed in CO_2. This is due to the fact that the concentrations of CH_4 sampled, at high frequency, fluctuate less than that of CO_2, and this results in a higher H_s coefficient. Finally the evolution of H_s for CO does not show any appreciable pattern. However, differently from CH_4, the average value, of the exponent H_s over the whole period of analysis, is also lower than in CO_2. This tells us that the concentrations of CO, sampled at high frequencies, fluctuate in a more than the other two GHG tracers, making the CO signal more noisy.

Fluctuations in the concentrations of CO_2, and in general of CH_4 and CO, could be affects by variation of PBL height. The height variation of the same, causing a dilution or a higher concentration of GHG tracers in the sampling region, significantly affects the fluctuations. The CO_2 produced and destroyed through the photosynthesis-respiration process thus undergoes more vigorous vertical mixing during summer while the PBL height is deeper with a transport of CO_2 from the lower to the upper troposphere [99], thus making the amplitude of the diurnal mean cycle more pronounced. On the contrary, in autumn and even more in winter the PBL height decreases and the signal of respiration remains trapped near the surface increasing the concentration and decreasing the amplitude of the cycle because there is less upward scattering due to the decrease in light exposure.

Therefore, as can be seen in fig.4.34 the variation of PBL height (green square) is strongly positively correlated with the monthly variation of the H_s exponent. Both the values of H_s and those of the PBL height can be seen to be minimum in the winter months and maximum in the summer months, and this trend

is mostly repeated in all the three years of sampling. In fig.4.35 is reported the cross correlation between the PBL height (taken from ERA5[34]) and the H_s for CO_2 (red square), CH_4 (green diamond) and CO (blue diamond), as a function of time lags. It is possible to notice how at lag-time 0 exists a strong correlation between the height of the PBL and the H_s which then decreases with time. Compared to CO_2, the H_s for CH_4 is anti-correlated with the PBL height. Although the shallow depth of the PBL results in an increase in the monthly average concentration of CH_4 in winter compared to autumn, the intra-day dynamics and than the destruction-production process, is governed by different processes and not the same process as for CO_2. In fact CH_4 is produced by biological and anthropogenic activities. Moreover it is mostly oxidized by the process of oxidation with the radical OH[85]. Therefore, the seasonality of OH, which is maximum in summer and minimum in winter[88], acts more in the period of maximum production of CH_4. This causes the higher CH_4 produced to be more compensated by making the amplitude of the larger fluctuations. This aspect is observable in the fluctuations of the $s(t)$ component, which has smaller measured values of H_s. On the other hand, in winter lower OH levels are produced OH resulting in a decrease in oxidation activity, corresponding to the period of maximum CH_4 concentration due to the lowering of the H_s of the PBL. This results in decreased fluctuations and an increase in the H coefficient. It was logical to expect the lower correlation values with the CO, because the signal of CO, as seen before, presents different characteristics with the presence of stationarity in the same without any particular trend in the evolution of the coefficient H_s.

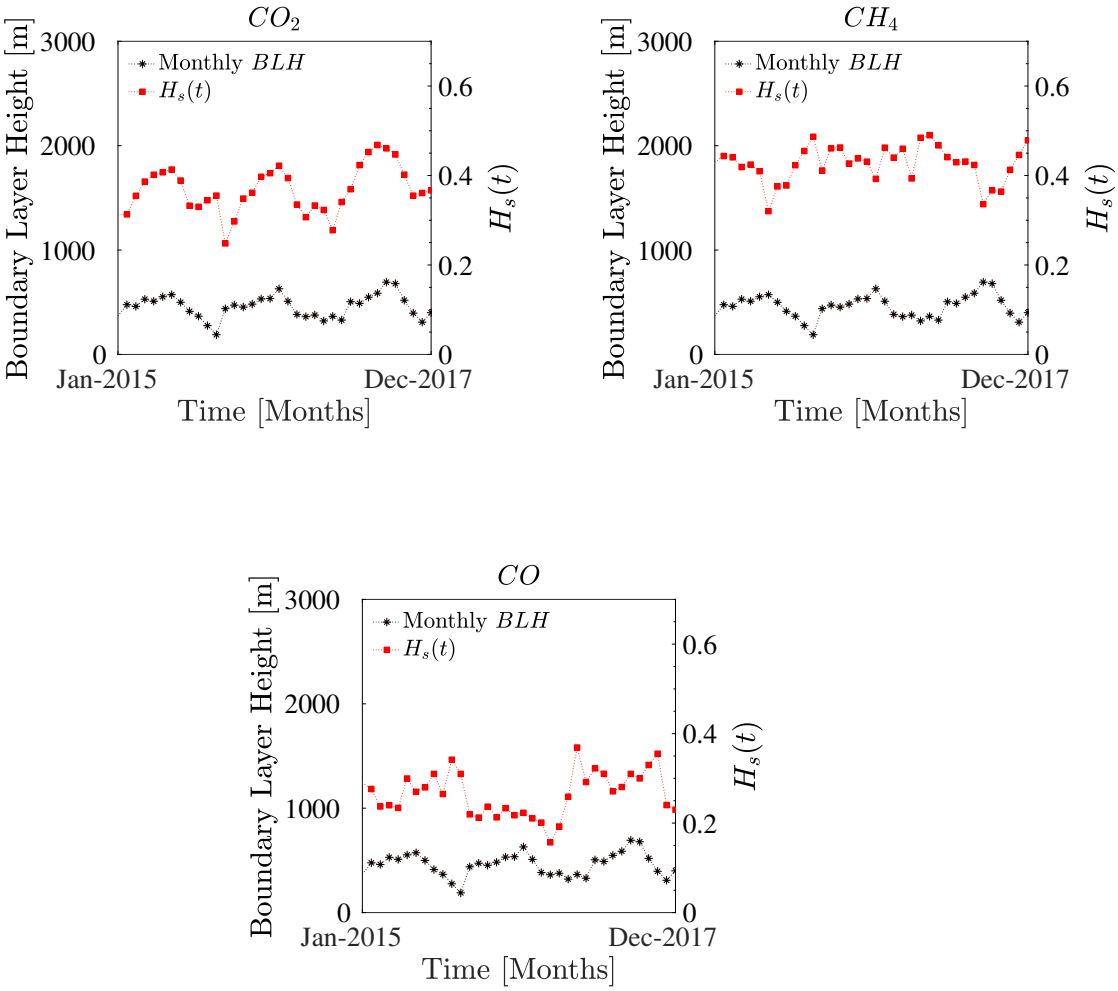

Figure 4.34:
Plot of monthly variation of Boundary Layers Height (green square) and monthly variation of the H coefficient of $s(t)$ component for CO_2 (red square) of three years of analysis.

The variation of coefficient $H_s(t)$ as been also investigate by considering gradually increasing time windows $\mathcal{T}_W$. In this case $s(t)$ component will be extrapolated starting with a time window $\mathcal{T}_W = 31$ days and then increasing the width of $\mathcal{T}_W$ up to a duration of 365 days. Again, the $s(t)$ component is reconstructed using the same methodology as applied previously. The evolution of $H_s(\mathcal{T}_W)$ is reported in fig.4.36, and a steeper variation is observed for CO_2 at $\mathcal{T}_W = 150$ days, in agreement with the seasonal modulation found previously (fig. 4.29). For $\mathcal{T}_W > 150$ $H_s(\mathcal{T}_W)$ presents a constant behaviour despite the decrease of H_s observed in fig. 4.29. This occurs because the increase of $\mathcal{T}_W$ incorporates the

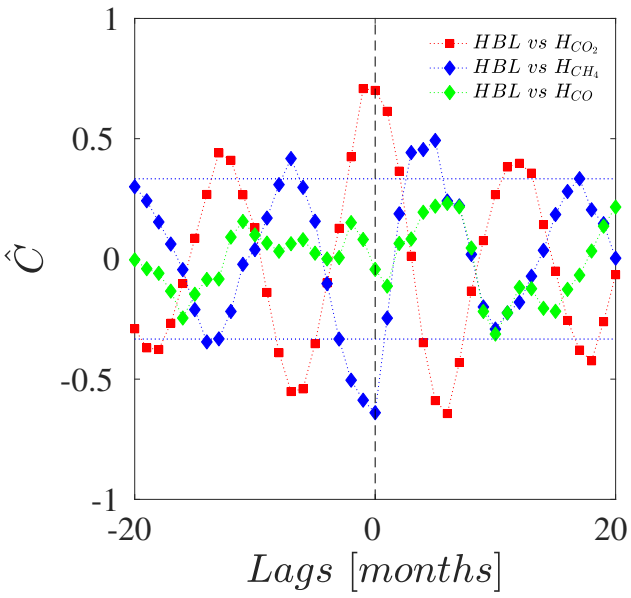

Figure 4.35:
Plot of the cross correlation between the BL Height and H_s of CO_2 (red square), CH_4 (blue diamond) and CO (green diamond) as a function of time lags. Vertical dotted line represent the time $lag = 0$. Horizontal lines represents the 95% confidence bounds

effects occurring in previous months (i.e. seasonal effects) thus resulting in a constant value of $H_s(\mathcal{T}_W)$. In other words, this behaviour is due to the fact that the increase of $\mathcal{T}_W$ produces an averaging between the physical processes involved in the dynamics of CO_2 in the various time periods implying first a steeper variation of H_s and successively a saturation of it. An almost constant behaviour for $H_s(\mathcal{T}_W)$ is observed for CO and CH_4, according with results presented in fig. 4.29. In fact, the amplitude variation of CO and CH_4 fluctuations during the year are two orders lower compared to that of CO_2; therefore the diurnal cycle does not act with the same intensity compared to CO_2. The behaviour of H as a function of $\mathcal{T}_W$ identified for the three GHG tracers is reported in fig.4.36 (right panel). It is interesting to note that, net of the values of the individual $H_s(\mathcal{T}_W)$ of DFA method, are in good agreement with values obtained through the SF method. In fact, for both methods a constant behaviour for CH_4 and CO and an increasing trend in $H_s(\mathcal{T}_W)$ for CO_2 have been found.

It is possible to quantify $H(\mathcal{T}_W)$ also through SF analysis in order to quantify the difference between ζ_1 and the coefficients H(tw) reported in fig.4.36), obtained through the DFA method. Unlike DFA where a discontinuity is appreciable at $\mathcal{T}_W = 150$, for SF method there is a smooth increment up to $\mathcal{T}_W = 180$.

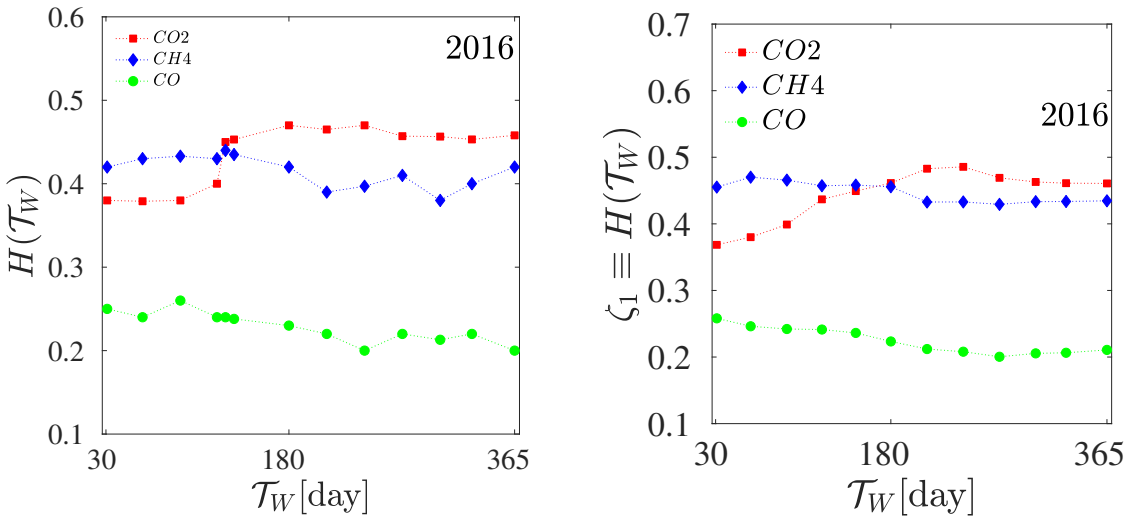

Figure 4.36:
left panel: Plot of variation $H(\mathcal{T}_W)$ according with time windows $\mathcal{T}_W$ for CO_2 (red squares), CH_4 (blue diamonds) and CO (green dots) of s(t) component. The rapid increase in the value of H at $\mathcal{T}_W = 150$ is in agreement with the modulation of H_s. **Right panel**: Variation of ζ_1 for CO_2 (red square), CH_4 (blue diamond) and CO (green dot) in function of time windows $\mathcal{T}_W$.

The relationship between them in terms of ratio $\zeta_1(\mathcal{T}_W)/H_s(\mathcal{T}_W)$ as a function of $\mathcal{T}_W$ is reported in fig.4.37. The ratio on average for all three GHG tracers is $\zeta_1(\mathcal{T}_W)/H_s(\mathcal{T}_W) \approx 1$, represented by the dashed lines in the plot for each GHG tracers,indicating that the two methods have the same efficiency in extracting the value of H_s.

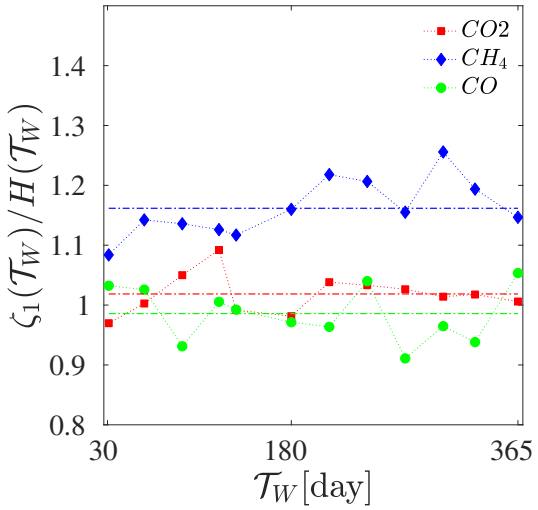

Figure 4.37:
Plot of the ratio between ζ_1 and $H(\mathcal{T}_W)$ for CO_2 (red squares), CH_4 (blue diamonds) and CO (green dots) as a function of $\mathcal{T}_W$. The dashed lines represents the mean value of the ratio for CO_2 (red), CH_4(blue) and CO (green) respectively which are about equal to one.

4.4 Fractal analysis of Mauna Loa CO_2 and CH_4 concentration

Since the datasets recorder to MLO are hourly, it is only possible to compare the results obtained between the two monitoring stations, since the data collected at MCU are sampled with a time interval $\Delta = 1$sec and those of MLO with $\Delta = 1$hour. This implies that both the $fast$ and the $slow$ components, defined for the MC datasets, cannot be defined on the MLO datasets on the same range of time scales. However, in the extrapolation of the components $f(t)$ for the Mauna Loa data, the scales used in the reconstruction evolves on the same range of the $s(t)$ component extrapolate for MCU. The scaling exponents obtained from $F_2(\ell)$ for the $f(t)$ component will be compared with those of the $s(t)$ component of MCU.

Another consideration that must be made regarding the analysis of the Mauna loa data is that the sub-intervals analysed do not have the same number points, in the same temporal length as those of MCU datasets. This is because, if sub-intervals of daily durations were considered $\mathcal{T}_W \approx 8.6 \times 10^4$ sec for MCU datasets, then in the case of Mauna Loa they have been considered directly

temporal intervals of a month, with the temporal window of duration $\mathcal{T}_W \approx 744$ hours, variable according to the month considered. In this case, the γ exponents is unique for each month, differently from the previous case where the data have been monthly averaged starting from 1 seconds data. Since they are hourly data, considering daily time windows would imply to have only 24 points, and applying the EMD method for the extrapolation of $\phi_j(t)$ on this interval, it would not give correct results given the small sample size. However, since the time intervals are monthly the value of the exponent H_f will be unique without averaging as done previously and the error will be the same as the one calculated on the fit.

In fig.4.38 are shown the monthly values of the H_f exponent for CO_2 (left panel) and CH_4 (right panel). The modulation of H_s observed in the CO_2 data collected at at MCU is also present in the CO_2 data collected at MLO. The

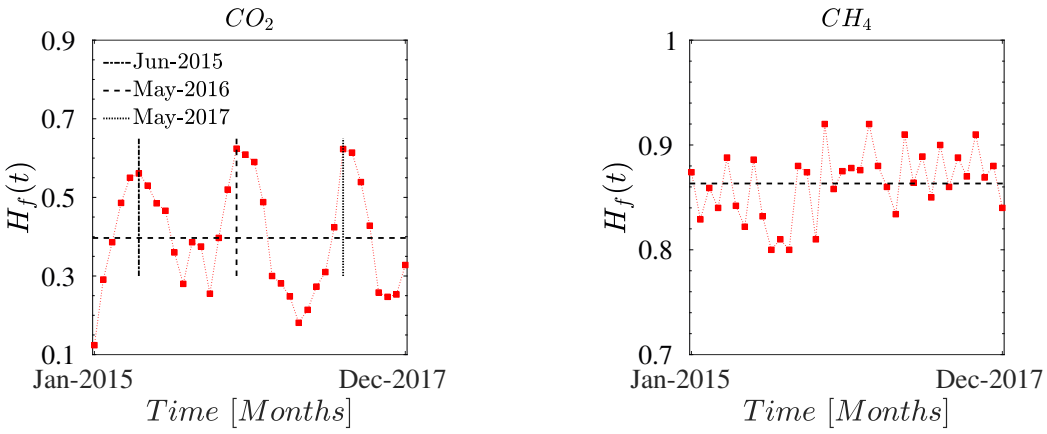

Figure 4.38:
Left panel: Variation of monthly Hurst exponent H_f of CO_2. The vertical dashed lines correspond to the maxima measured in the three sampling years, which correspond to the months in which the highest concentrations are detected in the year. The horizontal dashed line corresponds to the average H_f which is about 0.4. **Right panel**: Evolution temporal evolution of the Hurst H coefficient for the fast component of the CH_4. There are no repeated absolute maxima over time that identify any patterns. The dashed horizon line is the average of the H_f coefficients equal to about 0.86.

alternation of minimums, in the winter months, and maximums in the summer months confirms the previous results. However, while it was possible for MCU to demonstrate how intra-day dynamics, through the periodicity of the H_s coefficient, is related to local effects such as the photosynthesis-respiration process and variation in PBL height, at Mauna Loa, this is not partly possible, due to the different geographically location of the site. Also, given the location it is pos-

sible that the effect is not due to local sources but to long-range transport. e.g. Amazonian forest etc. In fact, as it can see from fig.4.39, no significant correlation is evident between the EVI index and the H coefficient. The EVI index has been calculated considering the entire island where the MLO observation station is located, as there is no vegetation around it. Given this particular location,

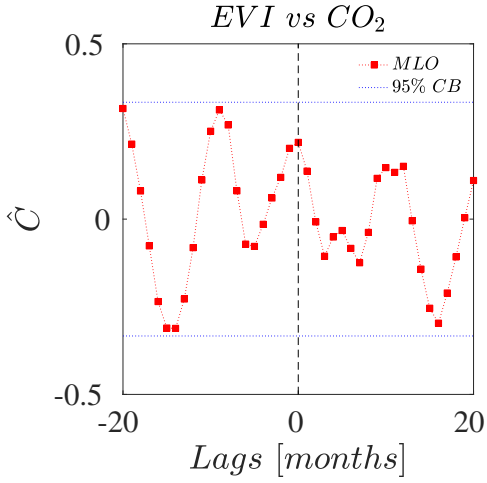

Figure 4.39:
Plot of cross correlation between monthly variation of H_f coefficient with EVI index for an area of $50 * 50Km^2$ centred on MLO. Horizontal dotted lines represents the 95% confidence bounds

several studies have been conducted to identify where air masses pollutants come from, showing that the seasonal variability of CO_2 is strongly correlated to the seasonal variation in PBL height seasonality of the wind, That could influence through long-range transport the variability of CO_2[120]. In fig.4.40 are shown the seasonal variation of the coefficient $H_f(t)$ and the height of the PBL (left panel) and their cross correlation (right panel).
A positive correlation between the change in PBL height and $H_f(t)$ for CO_2 at lag 0,is observed, which possibly confirms that vertical mixing coupled with long-range transport, could be the principal drivers of the evolution of CO_2 fluctuations, even on intra-day scales.

However there are some differences between the two results, first of all the maximum value is not recorded in the month of July, as found for the data of MCU, but in May and this is due to the fact that the maximum concentration of CO_2 is found in May. This confirms the hypothesis that the monthly behaviour of the value of H_f, being to the dynamics and therefore to the fluctuations of the signal under examination, is strictly connected to the period under examination

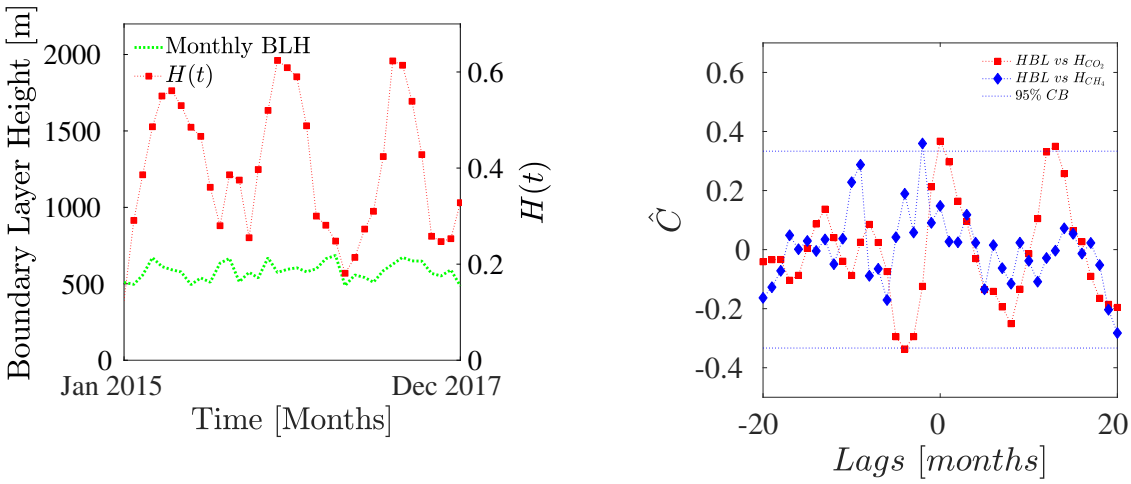

Figure 4.40:
Left panel: Plot of monthly variation of BL height (green square) and H_f monthly variation (red square) of three years of analysis. **Right panel**: Plot of cross correlation between BL height with CO_2 (red square) and CH_4 as a function of time lags.

and ,therefore, is linked to the phenomena that regulate the same. Secondly it is possible to see how the H_f in modulus are greater in MLO than in MCU. Being the sampling of MLO records hourly, the signal will be smoother than that of MCU which is sampled per second and this results in an increase of the coefficient H_f.

Another feature that it is possible to notice, but which has already been analysed in other work[23], is the long-range persistence of fluctuations in CO_2 concentrations. Although the datasets that are examined are of different lengths, resulting in an analysis on different time scales, this work strengthens the thesis for which the fluctuations of CO_2 concentrations, in addition to positively correlated in a power-law fashion on scales (up to 11 years), are also positively correlated on daily and monthly time scales. The H_s for CH_4 does not presents any trend, despite the sources and sink of CH_4 are everywhere similar. However, as has been shown by Harris et al. [121], the records at MLO of the CH_4 are related to flow regime perturbations, and do not depend on exclusively sources/sinks characteristics.

4.5 Multifractal Detrended Fluctuation Analysis

The multifractality of GHG concentrations has been widely studied in other works[122]. Furthermore, it was seen that complex patterns that related to the degree of multifractality, also indicates long-range correlations [122]. Here slow components of CO_2, CH_4 and CO have been analysed through the MFDFA method in order to understand how the multifractal properties are affected by studying the phenomenon on different time windows $\mathfrak{T}_W$ (gradually increasing). For each $\mathfrak{T}_W$ the multifractal spectra is calculated and the width, measured in order to see how much the strength of multifractality, increases.

4.5.1 Characterization of MFDFA variables

The MFDFA method allows to analyse the scaling of the $F_q(\ell)$ for various generalized q-orders moments not only that for $q = 2$. In fig.4.41 is reported the scaling of the $F_q(\ell)$ versus ℓ for $q = -10, 0, 10$ obtained for the $s(t)$ components of the CO_2 (left panel), CH_4 (central panel) and CO (right panel) of a sub-interval (it is considered the datasets referred to January 2016). In fig.4.41 $F_q(\ell)$ have been plotted, and as it can be seen from the $F_q(\ell)$ it has a linear dependence on the scale ℓ. Moreover the slopes of $F_q(\ell)$ depends on the value of q.

Through the MFDFA method it is possible to define the variation of H as a

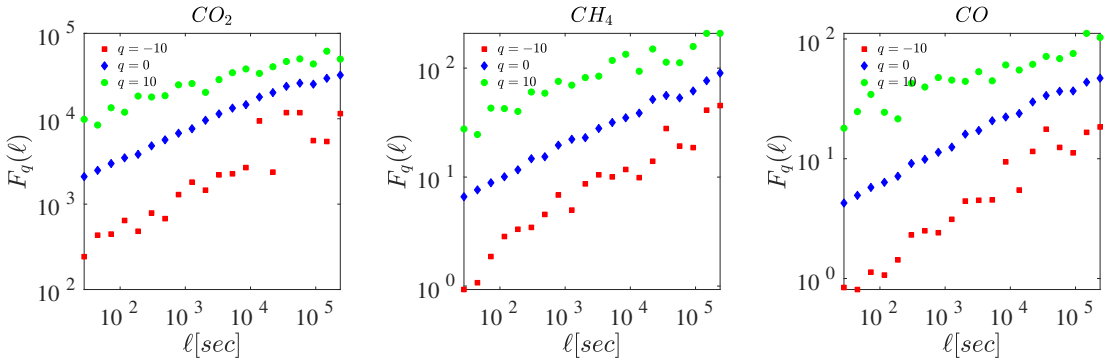

Figure 4.41:
Log-log plot of fluctuations function $F_q(\ell)$ for CO_2 (left panel), CH_4 (central panel) and CO (right panel) $s(t)$ component. The difference in $F_q(\ell)$ between positive and negative q is more visible for small scales than for large scales.

function of moments q by extrapolating the values $H(q)$ through a linear fit of the various $F_q(\ell)$. In fig.4.42 (left panel) is reported the behaviour of the coefficient $H(q)$ as a function of the q-order moments for the time window $\mathfrak{T}_W = 31$ days, i.e. January 2016.

The value of the coefficient $H(q)$ is not constant, indicating the multifractality of the signal, or in other words that there is a different scaling between small and large fluctuations and also between positive and negative fluctuations. This result indicates that there is a multifractalities on two different levels, namely a multifractality due to the different temporal cyclicity, as they have seen for component $s(t)$ of CO_2, and an intrinsic multifractality in each monthly interval.

In this case, unlike the values shown in fig.4.29 for $H_s(t)$, the value of $H(q)$ is increased by a quantity 1, since this quantity defines the stationarity or not of the process. In fact the values of $H(q)$ vs q define the degree of stationarity, correlation and persistence. If the value of scaling exponent of fluctuations function of $q = 2$ γ is $0 < \gamma < 0.5$, the process is anti-correlated and if $0.5 < \gamma < 1$, the process is positive correlated [30].

Also, in according with Kantelhardt et al.[64], if $0 < \gamma < 1$ the value of Hurst exponent is $H(q = 2) = \gamma$. The particular case where $\gamma = 0.5$ and $\gamma = 1$ indicate respectively an uncorrelated (white noise) and a $1/f$-noise (pink noise) process. In general if $1 < \gamma < 2$ the signal is a non-stationary process where if $\gamma = 1.5$, the process is a Brownian process [59],[123], and in this case $H(q = 2) = \gamma - 1$. This argument obviously holds for any $H(q)$, and from the fig.4.42 (left panel) is evident that the value of $H(q)$ is greater than 1 indicating a strong persistence. The behaviour of $H(q)$ is obviously reflected in that of the q-order mass exponent $\tau(q)$, which is related to $H(q)$ via the relation $\tau(q) = qH(q) - 1$. Indeed if $H(q)$ is a constant linear behaviour for $\tau(q)$ is expected, and a non-linear q-dependency is observed if $H(q)$ is not constant. The behaviour of $\tau(q)$ vs q is shown in fig.4.42(right panel) for all GHG tracers, where it is clearly visible the curved q-dependency in all three processes, fingerprint of the multifractal nature of the process.

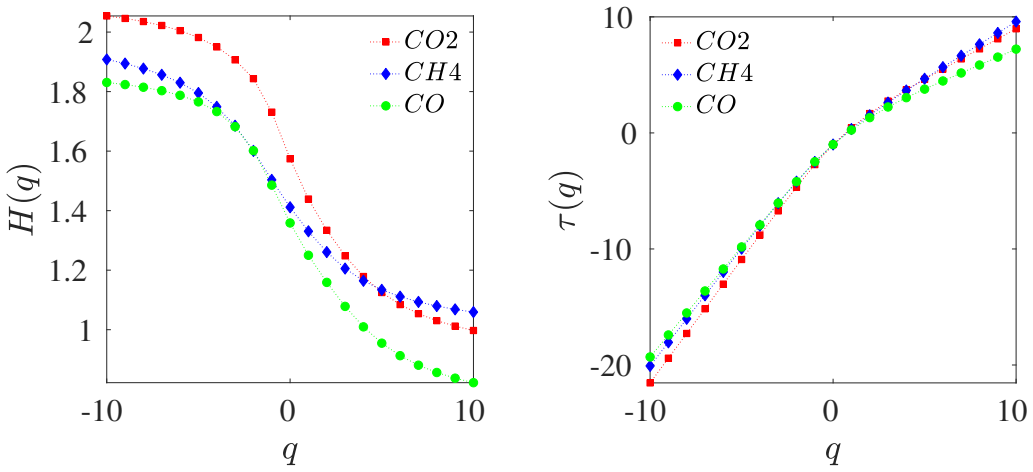

Figure 4.42:
Left panel: variation of $H(q)$ in function of q-moment for CO_2 (red square), CH_4 (blue diamond) and CO(green dot). **Right panel:** variation of q-order mass exponent $\tau(q)$ in function of q for CO_2 (red square), CH_4 (blue diamond) and CO(green dot).

4.5.2 Singularity spectrum $D_q(\alpha)$

The singularity spectrum $D_q(\alpha)$ is obtained via the relation $D_q(\alpha) = q\alpha_q - \tau(q)$ where α_q is obtained via through the Legendre transform: $\alpha_q = d\tau_q/dq$. In fig.4.43(left panel) are reported the singularity spectra of the interval considered of CO_2, CH_4 and CO (January 2016). It should be emphasized that the Hölder exponent α_q is related to the exponent H from which $\tau(q)$ is calculated, and is not directly a singularity exponent. The width of the spectrum $D_q(\alpha)$ defined as $\Delta_\alpha = \alpha_{max} - \alpha_{min}$ with $D_q(\alpha_{max}) = D_q(\alpha_{min}) = 0$ is a measure of the degree of multifractality of the time series [124]. In fact, as the width of the spectrum $D_q(\alpha)$ increases, also increases the strength of multifractality. In other words, a greater width of the spectrum involves stronger singularity exponents α_q and a wider distribution of H values. The asymmetrical shape of the spectra, especially for the CO_2 (red square), gives information about the events that characterize the dynamics. Indeed, the $s(t)$ component is characterized by fluctuations over long timescales, on the other hand, there are not higher frequency fluctuations present in the $s(t)$ component. Therefore, the singularity spectrum has a more pronounced tail. Thus, the higher right tail of the spectra (especially for CO_2) is related to local fluctuations with large magnitudes, where this is reflected on the $F_q(\ell)$ which are insensitive to local fluctuations[48]. Because the $s(t)$ component contains low-frequency component, this means that it is mainly formed by relatively large events indicating that the multifractality is mainly governed

by small fluctuations. The existence of a singularity spectrum implies that the paths of the processes contain multiple Holder $H(q)$ exponents other than the dominant one. These singularities are the irregularities resulting from the power laws that are the basis of the self-similarity of process statistics[125].

The α_q value, corresponding to the maximum of the peak of the spectrum $D_q(\alpha)$, is different for the three GHG tracers. Since the value varies over a range of values, where for example for CO_2 this range is between 0.3 and 1.2, then it differs from the K41 law[125]. On the other hand, this diversity indicates that there is not a universal scaling law that describes the dynamics of GHG tracers in the atmosphere. The stability of atmosphere appears to play a significant role in determining the observed scaling laws[125]. Now, considering the same time windows $\mathcal{T}_W$ used for the estimation of $H(\mathcal{T}_W)$, it is possible to understand how the width of the spectrum $D_q(\alpha)$ varies as $\mathcal{T}_W$ varies . In fig.4.43(left panel) are reported the behaviour of $\Delta_\alpha(\mathcal{T}_W)$ as a function of $\mathcal{T}_W$ for the $s(t)$ component of CO_2 (red square), CH_4(blue diamond) and CO (green circle). For CO_2 it can be seen a rapid increase in Δ_α for $\mathcal{T}_W = 150$ followed by a constant behaviour. This modification is in line with the behaviour of $H(\mathcal{T}_W)$ previously analysed. On the other hand, the increasing of the time window $\mathcal{T}_W$ corresponds to the increasing number of physical processes, involving the dynamics of CO_2 during different months, and in general GHG tracers. In fact, the increasing value of the H coefficient from winter to summer months causes an increment of multifractality of $s(t)$ for CO_2 resulting in a broadening of the spectrum $D_q(\alpha)$. The behaviour of Δ_α is maintained constant because the $\mathcal{T}_W$ time window is expanded and therefore more physical processes, with many other different H_s, are added. The decreasing effect of the amplitude of the diurnal cycles passing from the summer months to the winter ones (which involves a decrease of H_s), does not affects Δ_α, which remains almost constant. Using large time windows includes the presence of summer diurnal cycles that increasing Δ_α. In fact, this is clearly visible by comparing the behaviour of the same in the first temporal windows $\mathcal{T}_W$ considered that it has a lower value than the rest. On the other hand, for CH_4 and CO there is no well-defined modification for $\Delta_\alpha(\mathcal{T}_W)$. In fact, the average values of $\Delta_\alpha(\mathcal{T}_W)$ are 1 and 0.8 respectively, which however represent the multifractality of the transport phenomena, but not an enhancement of the multifractality strength. The effect of multifractality is due to modulation of Hs that was identified earlier.

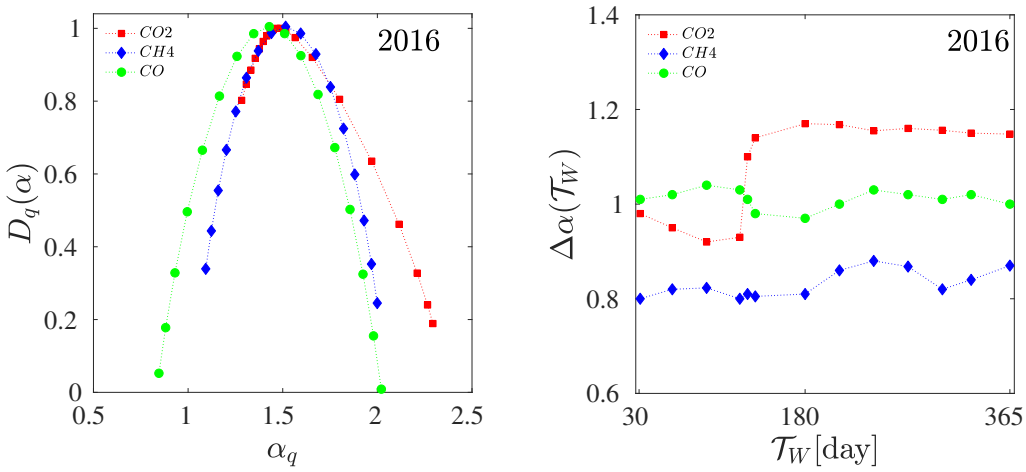

Figure 4.43:
Left panel: plot of singularity spectrum $D_q(\alpha)$ in function of α_q for CO_2 (red square), CH_4 (blue diamond) and CO(green dot). **Right panel:** variation of width of the singularity spectrum $D_q(\alpha)$ defined as Δ_α in function of time windowed $\mathcal{T}_W$ for CO_2 (red square), CH_4 (blue diamond) and CO(green dot).

Chapter 5

Conclusions

In this work have been analysed the scaling properties of the intra-day components that constitute the temporal behaviour of GHG tracers (CO_2, CH_4 and CO) through different methodologies in order to capture their fractal and multifractal nature. From the analysis two components (acting two different timescales), were observed in their dynamics. Moreover, the results showed that local properties of the fluctuations of such component, labelled $s(t)$ and $f(t)$, and therefore the properties of the GHG tracers, that are strictly related to particular timescale and period of the year (season) considered. Such properties could be related to the principal drivers affecting the dynamics of CO_2, CH_4 and CO concentrations.

By decomposing the GHG datasets, within the EMD framework, a first heuristic estimation of Hurst coefficient H (measure of the long-term memory of a time series), had been obtained by relating the variance V_j of each individual IMF with their of characteristic periods T_j, in particular, a power law behaviour was found in two distinct range of temporal scale: the first in a range in $t \in [10, 100]$ sec, and a second in $t \in [200, 21600]$. Due to the fact that each range presents a different power slope, two distinct Hurst coefficients have been defined H_f and H_s, respectively, related to the distinct temporal ranges. In addition, by monthly averaging the values obtained for H_s, a seasonal modulation of the Hurst coefficient has been identified for the CO_2 dataset, ranging in $H_s \in [0.46, 0.58]$, while a constant temporal evolution had been observed for CO and CH_4.

Accordingly with the turbulent scale invariance theory [104], [105], a passive tracer transport is expected for $H = 5/9 \approx 0.56$, and the variation from this value can represent sources or sinks of the tracer. Here, the modulation identified for the CO_2 is an indication of the period of sources during hot seasons (spring/summer, $H_s > 5/9$), and sinks (due to particular climatic or meteorolog-

ical conditions) during the cold seasons (autumn/winter $H_s < 5/9$). Concerning the other GHG tracers, a continuous sinks effects have been identified for CH_4 and CO, since H_s <5/9 during the whole period, where the only H_f coefficient of CO is $H_f > 5/9$. For CO the behaviour of H_s coefficient is flat which is compatible with that of turbulence. So probably the fluctuations seen on long timescales in CO are a surrogate in some way for the turbulent motion of the atmosphere.

So, through Mutual information, starting from the various IMFs, and applying the decomposition criteria presented in [69], the system was divided in four different datasets, encompassing different physical properties:
a fast (turbulent) and a slow (synoptic) components, an experimental noise term, and a constant daily offset. On the other hand, for each dataset, the $s(t)$ component is defined as sum of IMFs for which the value of Mutual Information is greater than the cut-off point v_z, calculated as the average of all $I(\Theta_j, \Theta_{j+1})$. The first two IMF modes, such as $I < 10^{-3}$, constitute the experimental noise term. And finally, the residual $r(t)$ constitutes the daily offset. The $f(t)$ component is the sum of all others IMFs, such as the value of v_j is less than the cut-off point v_z. The decomposition performed on the sub-intervals of the GHG tracers is validated by relating the energy density E_j with the average period T_j of each IMFs [108],[109]. In addition, by applying such test it was found that all IMFs extracted via the sifting procedure, are significant. In fact, because the energy values of each IMF are above the theoretical line, this is an indication of the fact that each IMFs contain statistical information corresponding to different physical processes. On the other hand, the IMFs extracted from a white-noise signal correspond to little perceptible physical processes indicating that the few useful statistical informations is contained in all IMFs. Moreover, in the $s(t)$ components is captured the characteristic diurnal modulation cycle that is recorded in the original datasets. On the other hand, the $f(t)$ components could be considered as a turbulent component.

In order to corroborate the results, the values of the two Hurst exponents have been extrapolated also via classical scaling of structure functions, which present a good agreement between the first order exponent ζ_1 and H_s/H_f, in the same range of time scale defined above. The scaling of the high order moment ζ_q ($q > 1$) presents a discrepancy from a linear behaviour, fingerprint of an intrinsic multifractality of the phenomena. The scaling exponents ζ_q have been compared with the classical Kolmogorov K41 prediction (no intermittency correction), and a strong discrepancy had been identified, especially for moment $q = 4$, which

indicates the active presence of the classical small scale intermittency. By comparing the monthly average values of ζ_q with classical values of the atmospheric turbulence [116],[117], $f(t)$ components for CO_2 and CH_4 are related to the turbulent component of the atmospheric motion, in which the values of first three q orders are comparable. However, for the slow component $s(t)$ the values of ζ_q are different, suggesting that the dynamics on a larger timescales is related to different phenomena.

Such effects have been characterized by means of a simple log-cascade model[114], dependent from a single parameter: the so called intermittency parameter μ. The average values of the intermittency parameter in the fast timescale (μ_f), for all three GHG traces, are slightly higher than the classical value $\mu \approx 0.02$ obtained in fully developed homogeneous and isotropic turbulence experiments [52],[115],[58]. The study in frequency space of components for CO_2, allows a further analysis about the value of the Hurst coefficient given by the relation $\zeta_2 = \beta - 1$, where β is the power-law exponent of the power spectral density, and confirms the temporal modulation of H_s and the constant behaviour of H_f pointed out with the other methods.

The scaling properties of these components have also been described by applying the DFA method, in which the same behaviour of H_f and H_s are observed in both timescales. Moreover, the effects of temporal modulation of H_s coefficient are also evident when considering $s(t)$ component defined over gradually increasing $\mathcal{T}_W$ time windows. Evolution of $H_s(\mathcal{T}_W)$ undergoes a steeper variation for $\mathcal{T}_W = 150$ days, and a constant behaviour for $\mathcal{T}_W > 150$. This occurs because the increase of $\mathcal{T}_W$ incorporates the effects occurring in previous months (i.e. seasonal effects) thus resulting in a constant value of $H_s(\mathcal{T}_W)$.

Analysis by MFDFA method of the $D_q(\alpha)$ singularity spectra of $s(t)$ components of GHG tracers defines the multi-fractal nature of the datasets. Since $s(t)$ component contains low-frequency components, the $D_q(\alpha)$ spectrum (especially for CO_2) shows a higher right tail. On the other hand, the $s(t)$ components are more governed by relatively larger events indicating a multifractality governed by small fluctuations. The temporal behaviour of H_s coefficients of GHG tracers is also reflected by the analysis of the width Δ_α, which is a measure of the degree/strength of multifractality of the time-series, of the $D_q(\alpha)$ spectrum as the time window $\mathcal{T}_W$ gradually increases. Indeed for CO_2, a steeper variation is observed for $\mathcal{T}_W = 150$ with a constant trend for $\mathcal{T}_W > 150$, indicating an increase in the degree of multifractality. The meteorological GHG tracers data collected from a turbulent atmosphere reveal that the flow and dispersion

dynamics exhibit a multi-fractal behaviour, as observed through the computed singularity spectrum, $D_q(\alpha)$, which is a characteristic as well as a self-similar behaviour. On the other hand, atmospheric physical processes that define the stability or instability of the atmosphere plays a central role in determining the scaling properties of the tracer fluctuations. The multifractality found in these time series can be observed from two different perspectives. In fact, one type of multifractality is due to the fact that the time series of GHG tracers are intermittent, and the other is found by the fact that for a complete description there is a need for a range of values of the H coefficient. On the other hand, an increasing in the time window $\mathcal{T}_W$ corresponds to analysing time series, in which dynamics governed by different physical processes that are defined according to the time period considered. Finally, the same set of analysis has been performed on a dataset of GHG tracers recoded at the MLO observatory. By analysing the MLO dataset, the same modulation was found in for the H_s of the CO_2 data. However, such modulation is positively correlated with the PBL height, but not with EVI index.

Different physical processes influence the dynamics of greenhouse gas tracers at the two stations, with the complication that the same source/sink process or the coupling of multiple processes may act differently at the specific site due to different climatic conditions. However, the seasonal modulation of the H_s of CO_2 and CH_4 and the constant behavior observed in the H_s value for CO represent distinctive and robust features that can be identified in the dynamics of GHG tracers regardless of the different geographic or climatological conditions. On the other hand, it is possible that the overall dynamics, without considering the values of individual H_s and the different position of the maxima and minima, which still correspond to the maxima and minima measured in the records datasets, are due to the same local physical phenomena, which define similar intra-day fractal properties.

The modulation of H_s could be related to principal drivers of the dynamics of CO_2, where the effect of turbulence could be masked by more energetic phenomena. The variation of Boundary layers height and variation of the photosynthesis-respiration process, through analysis of variation in the EVI and NDVI indices, were investigated. The high correlation value $\hat{C} = 0.63$ between H_s and EVI index and $\hat{C} = 0.86$ between H_s and the PBL height at $lag = 0$ suggest that these phenomena play a primary role in the intra-day fractal properties of CO_2.

From the performed analyses the modulation of $H_s(t)$ for CO_2 and CH_4 is appreciable in every case, like the constant behaviour of H_s for CO, but

the values of $H_s(t)$ sometimes differ among the various methods, since each method performs differently on the same dataset [126]. In fact, if the same values of H_s observed through the analysis of the IMFs variances (extracted via EMD method), are comparable with those observed in the PSD, while SF and DFA methods gives a slightly lower values for H_s. The H_f of the three GHG tracers, calculated through the different methodologies presents similar values and a constant behavior in time. However, it is important to note that analysis through one methodology versus another, shows H values that differ slightly from each other. Likewise, analysing intra-day properties involves analysing low-scale fluctuations, it is possible that one method versus is sensitive to the structure of the signal itself.

Since the evolution of climate system is characterized by complex phenomena that interact with each other, the analysis of the scaling properties of these systems, such as GHG tracers, provides an help in the implementation of new methodologies in climate-atmospheric models. Indeed, the intra-day fractal properties and the primary role that environmental drivers play in the evolution of the dynamics of GHG tracers, analysed in this work, are important properties that can be exploited in the parametrization of sub-grid processes in atmospheric-climatic models. In fact, it is possible to improve the quality of sub-grid scale processes and various parametrizations of air quality and global circulation models. In addition, they provide to generate emission maps with stochastic or fractal dynamics, improving the results of climate scenarios.

Bibliography

[1] S. A. Stocker, T., "Influence of co2 emission rates on the stability of the thermohaline circulation," *Nature*, vol. 388, p. 862–865, 1997.

[2] N. Loeb, B. Wielicki, D. Doelling, G. Smith, D. Keyes, S. Kato, N. Manalo-Smith, and T. Wong, "Toward optimal closure of the earth's top-of-atmosphere radiation budget," *Journal of Climate - J CLIMATE*, vol. 22, pp. 748–766, 02 2009.

[3] S. Manabe, "Role of greenhouse gas in climate change**," *Tellus A: Dynamic Meteorology and Oceanography*, vol. 71, no. 1, p. 1620078, 2019.

[4] C. D. Keeling, "The concentration and isotopic abundances of carbon dioxide in the atmosphere," *Tellus*, vol. 12, no. 2, pp. 200–203, 1960.

[5] C. D. Keeling, R. B. Bacastow, A. E. Bainbridge, C. A. Ekdahl Jr., P. R. Guenther, L. S. Waterman, and J. F. S. Chin, "Atmospheric carbon dioxide variations at mauna loa observatory, hawaii," *Tellus*, vol. 28, no. 6, pp. 538–551, 1976.

[6] W. Buermann, B. R. Lintner, C. D. Koven, A. Angert, J. E. Pinzon, C. J. Tucker, and I. Y. Fung, "The changing carbon cycle at mauna loa observatory," *Proceedings of the National Academy of Sciences*, vol. 104, no. 11, pp. 4249–4254, 2007.

[7] P. K. PATRA, M. TAKIGAWA, K. ISHIJIMA, B.-C. CHOI, D. CUNNOLD, E. J. DLUGOKENCKY, P. FRASER, A. J. GOMEZ-PELAEZ, T.-Y. GOO, J.-S. KIM, P. KRUMMEL, R. LANGENFELDS, F. MEINHARDT, H. MUKAI, S. Orsquo;DOHERTY, R. G. PRINN, P. SIMMONDS, P. STEELE, Y. TOHJIMA, K. TSUBOI, K. UHSE, R. WEISS, D. WORTHY, and T. NAKAZAWA, "Growth rate, seasonal, synoptic, diurnal variations and budget of methane in the lower atmosphere," *Journal*

of the Meteorological Society of Japan. Ser. II, vol. 87, no. 4, pp. 635–663, 2009.

[8] R. B. BACASTOW, "Modulation of atmospheric carbon dioxide by the southern oscillation," *Nature*, vol. 261, pp. 116–118, 1976.

[9] P. Friedlingstein, J.-F. Müller, and G. Brasseur, "Sensitivity of the terrestrial biosphere to climatic changes: Impact on the carbon cycle," *Environmental Pollution*, vol. 83, no. 1, pp. 143–147, 1994.

[10] I. Y. Fung, C. J. Tucker, and K. C. Prentice, "Application of advanced very high resolution radiometer vegetation index to study atmosphere-biosphere exchange of co2," *Journal of Geophysical Research: Atmospheres*, vol. 92, no. D3, pp. 2999–3015, 1987.

[11] E. L. McGrath-Spangler and A. S. Denning, "Global seasonal variations of midday planetary boundary layer depth from calipso space-borne lidar," *Journal of Geophysical Research: Atmospheres*, vol. 118, no. 3, pp. 1226–1233, 2013.

[12] J. Holton, "An introduction to dynamic meteorology," 2004.

[13] R. S. J. Tol and A. F. de Vos, "Greenhouse statistics-time series analysis," *Theoretical and Applied Climatology*, vol. 48, pp. 63–74, Jun 1993.

[14] A. M. Selvam, "Nonlinear dynamics and chaos: Applications in atmospheric sciences," 2010.

[15] B. B. Mandelbrot, "Fractals: Form, chance and dimension," 1977. Freeman, San Francisco.

[16] H. E. Stanley, "Power laws and universality," *Nature*, vol. 378, 1995.

[17] H. Hurst, "Long-term storage capacity of reservoirs," *Transactions of the American Society of Civil Engineers*, vol. 116, pp. 770–799, 1951.

[18] D. Harte, *Multifractals: Theory and applications*. 01 2001.

[19] P. Patra, M. Santhanam, M. P., M. Takigawa, and T. Nakazawa, "1/f noise and multifractality in atmospheric-co2 records," 11 2006.

[20] R. O. Weber and P. Talkner, "Spectra and correlations of climate data from days to decades," *Journal of Geophysical Research: Atmospheres*, vol. 106, no. D17, pp. 20131–20144, 2001.

[21] C.-K. Lee, D.-S. Ho, C.-C. Yu, and C.-C. Wang, "Fractal analysis of temporal variation of air pollutant concentration by box counting," *Environ. Model. Softw.*, vol. 18, pp. 243–252, 2003.

[22] C. G. Tzanis, I. Koutsogiannis, K. Philippopoulos, and N. Kalamaras, "Multifractal detrended cross-correlation analysis of global methane and temperature," *Remote Sensing*, vol. 12, no. 3, 2020.

[23] C. Varotsos, M.-N. Assimakopoulos, and M. Efstathiou, "Technical note: Long-term memory effect in the atmospheric co_2 concentration at mauna loa," *Atmospheric Chemistry and Physics*, vol. 7, no. 3, pp. 629–634, 2007.

[24] K. Shi and C.-Q. Liu, "Self-organized criticality of air pollution," *Atmospheric Environment*, vol. 43, pp. 3301–3304, 07 2009.

[25] C. Varotsos, J. Ondov, and M. Efstathiou, "Scaling properties of air pollution in athens, greece and baltimore, maryland," *Atmospheric Environment*, vol. 39, no. 22, pp. 4041–4047, 2005.

[26] C.-K. Lee, L.-C. Juang, C.-C. Wang, Y.-Y. Liao, C.-C. Yu, Y.-C. Liu, and D.-S. Ho, "Scaling characteristics in ozone concentration time series (octs)," *Chemosphere*, vol. 62, pp. 934–46, 03 2006.

[27] A. Sarkar and P. Barat, "Scaling analysis on Indian foreign exchange market," *Physica A Statistical Mechanics and its Applications*, vol. 364, pp. 362–368, May 2006.

[28] N. Chandra, S. Lal, S. Venkataramani, P. K. Patra, and V. Sheel, "Temporal variations of atmospheric co_2 and co at ahmedabad in western india," *Atmospheric Chemistry and Physics*, vol. 16, no. 10, pp. 6153–6173, 2016.

[29] G. P. Brasseur and D. J. Jacob, *Parameterization of Subgrid-Scale Processes*, p. 342–398. Cambridge University Press, 2017.

[30] C. K. Peng, S. V. Buldyrev, S. Havlin, M. Simons, H. E. Stanley, and A. L. Goldberger, "Mosaic organization of dna nucleotides.," *Physical review. E, Statistical physics, plasmas, fluids, and related interdisciplinary topics*, vol. 49 2, pp. 1685–9, 1994.

[31] A. N. Kolmogorov, V. Levin, J. C. R. Hunt, O. M. Phillips, and D. Williams, "The local structure of turbulence in incompressible viscous fluid for very large reynolds numbers," *Proceedings of the Royal Society of*

London. Series A: Mathematical and Physical Sciences, vol. 434, no. 1890, pp. 9–13, 1991.

[32] N. Nava, T. Di Matteo, and T. Aste, "Anomalous volatility scaling in high frequency financial data," *Physica A: Statistical Mechanics and its Applications*, vol. 447, pp. 434–445, 2016.

[33] D. K., "Mod13c1 modis/terra vegetation indices 16-day l3 global 0.05deg cmg v006 [data set]," 2015. NASA EOSDIS Land Processes DAAC.

[34] B. B. B. P. B. G. H. A. M. S. J. N. J. P. C. R. R. R. I. S. D. S. A. S. C. D. D. T. J.-N. Hersbach, H., "Era5 hourly data on single levels from 1979 to present.," 2018. Copernicus Climate Change Service (C3S) Climate Data Store (CDS).

[35] C. Chatfield, *The Analysis of Time Series*. New York: Plenum Press, 2003.

[36] N. E. Huang, Z. Shen, S. R. Long, M. li C. Wu, H. H. Shih, Q. Zheng, N. chyuan Yen, C. C. Tung, and H. H. Liu, "The empirical mode decomposition and the hilbert spectrum for nonlinear and non-stationary time series analysis," *Proceedings of the Royal Society of London. Series A: Mathematical, Physical and Engineering Sciences*, vol. 454, pp. 903 – 995, 1998.

[37] P. Flandrin, G. Rilling, and P. Goncalves, "Empirical mode decomposition as a filter bank," *IEEE Signal Processing Letters*, vol. 11, pp. 112–114, Feb 2004.

[38] N. Tsakalozos, K. Drakakis, and S. Rickard, "A formal study of the nonlinearity and consistency of the empirical mode decomposition," *Signal Process.*, vol. 92, pp. 1961–1969, sep 2012.

[39] G. Rilling, P. Flandrin, and P. Gonçalves, "On empirical mode decomposition and its algorithms," *Proceedings of IEEE-EURASIP Workshop on Nonlinear Signal and Image Processing NSIP-03*, vol. 3, 06 2003.

[40] R. Rato, M. Ortigueira, and A. Batista, "On the hht, its problems, and some solutions," *Mechanical Systems and Signal Processing*, vol. 22, pp. 1374–1394, August 2008.

[41] P. P. M. Grasso and B. M. Colosimo, "Empirical mode decomposition of pressure signal for health condition monitoring in waterjet cutting,"

The International Journal of Advanced Manufacturing Technology, vol. 72, pp. 347 – 364, 2014.

[42] B. B. Mandelbrot and J. W. V. Ness, "Fractional brownian motions, fractional noises and applications," *SIAM Review*, vol. 10, no. 4, pp. 422–437, 1968.

[43] B. B. Mandelbrot and J. R. Wallis, "Some long-run properties of geophysical records," *Water Resources Research*, vol. 5, no. 2, pp. 321–340, 1969.

[44] R. Peltier, J. Levy Vehel, P. Signal, and P. Fractales, "Multifractional brownian motion : Definition and preliminary results," 10 1995.

[45] C. Meneveau and K. R. Sreenivasan, "Simple multifractal cascade model for fully developed turbulence," *Phys. Rev. Lett.*, vol. 59, pp. 1424–1427, Sep 1987.

[46] I. Graham, F. Kuo, D. Nuyens, R. Scheichl, and I. Sloan, "Analysis of circulant embedding methods for sampling stationary random fields," *SIAM Journal on Numerical Analysis*, vol. 56, 10 2017.

[47] S. V. Muniandy and S. C. Lim, "Modeling of locally self-similar processes using multifractional brownian motion of riemann-liouville type," *Phys. Rev. E*, vol. 63, p. 046104, Mar 2001.

[48] E. Ihlen, "Introduction to multifractal detrended fluctuation analysis in matlab," *Frontiers in Physiology*, vol. 3, p. 141, 2012.

[49] A.-L. Barabási and T. Vicsek, "Multifractality of self-affine fractals," *Phys. Rev. A*, vol. 44, pp. 2730–2733, Aug 1991.

[50] E. Bacry, J. Delour, and J. F. Muzy, "Multifractal random walk," *Phys. Rev. E*, vol. 64, p. 026103, Jul 2001.

[51] J. W. Kantelhardt, S. A. Zschiegner, E. Koscielny-Bunde, S. Havlin, A. Bunde, and H. Stanley, "Multifractal detrended fluctuation analysis of nonstationary time series," *Physica A: Statistical Mechanics and its Applications*, vol. 316, no. 1, pp. 87 – 114, 2002.

[52] J. F. Muzy, E. Bacry, and A. Arneodo, "Wavelets and multifractal formalism for singular signals: Application to turbulence data," *Phys. Rev. Lett.*, vol. 67, pp. 3515–3518, Dec 1991.

[53] Z. Wu and N. E. Huang, "A study of the characteristics of white noise using the empirical mode decomposition method," *Proceedings of the Royal Society of London. Series A: Mathematical, Physical and Engineering Sciences*, vol. 460, no. 2046, pp. 1597–1611, 2004.

[54] N. E. Huang, *INTRODUCTION TO THE HILBERT–HUANG TRANSFORM AND ITS RELATED MATHEMATICAL PROBLEMS*, pp. 1–26.

[55] Y. X. Huang, F. G. Schmitt, Z. M. Lu, P. Fougairolles, Y. Gagne, and Y. L. Liu, "Second-order structure function in fully developed turbulence," *Phys. Rev. E*, vol. 82, p. 026319, Aug 2010.

[56] F. Carbone, C. N. Gencarelli, and I. M. Hedgecock, "Lagrangian statistics of mesoscale turbulence in a natural environment: The agulhas return current," *Phys. Rev. E*, vol. 94, p. 063101, Dec 2016.

[57] Y. X. Huang, F. G. Schmitt, Z. M. Lu, and Y. L. Liu, "An amplitude-frequency study of turbulent scaling intermittency using empirical mode decomposition and hilbert spectral analysis," *EPL (Europhysics Letters)*, vol. 84, p. 40010, nov 2008.

[58] F. Carbone, D. Telloni, A. G. Bruno, I. Hedgecock, F. De Simone, F. Sprovieri, L. Sorriso-Valvo, and N. Pirrone, "Scaling properties of atmospheric wind speed in mesoscale range," *Atmosphere*, vol. 10, p. 611, 10 2019.

[59] K. Hu, P. C. Ivanov, Z. Chen, P. Carpena, and H. Eugene Stanley, "Effect of trends on detrended fluctuation analysis," *Phys. Rev. E*, vol. 64, p. 011114, Jun 2001.

[60] S. Havlin, L. Amaral, Y. Ashkenazy, A. Goldberger, P. Ivanov, C. Peng, and H. Stanley, "Application of statistical physics to heartbeat diagnosis," *Physica A: Statistical Mechanics and its Applications*, vol. 274, pp. 99–110, 12 1999.

[61] L. Telesca, M. Lovallo, A. Ramirez-Rojas, and F. Angulo-Brown, "Scaling instability in self-potential earthquake-related signals," *Physica A: Statistical Mechanics and its Applications*, vol. 388, pp. 1181–1186, 04 2009.

[62] C. Varotsos and D. Kirk-Davidoff, "Long-memory processes in ozone and temperature variations at the region 60 s - 60 n," *Atmospheric Chemistry and Physics*, vol. 6, no. 12, pp. 4093–4100, 2006.

[63] A. Bunde, S. Havlin, J. W. Kantelhardt, T. Penzel, J.-H. Peter, and K. Voigt, "Correlated and uncorrelated regions in heart-rate fluctuations during sleep," *Phys. Rev. Lett.*, vol. 85, pp. 3736–3739, Oct 2000.

[64] J. W. Kantelhardt, E. Koscielny-Bunde, H. H. Rego, S. Havlin, and A. Bunde, "Detecting long-range correlations with detrended fluctuation analysis," *Physica A: Statistical Mechanics and its Applications*, vol. 295, no. 3, pp. 441 – 454, 2001.

[65] J. Feder, *Fractals*. New York: Plenum Press, 1988.

[66] C. E. Shannon, "A mathematical theory of communication," *Bell System Technical Journal*, vol. 27, no. 3, pp. 379–423, 1948.

[67] A. Kraskov, H. Stögbauer, and P. Grassberger, "Estimating mutual information," *Phys. Rev. E*, vol. 69, p. 066138, Jun 2004.

[68] A. Papana and D. Kugiumtzis, "Evaluation of mutual information estimators on nonlinear dynamic systems," 2008.

[69] R. A. Rios, L. Parrott, H. Lange, and R. F. de Mello, "Estimating determinism rates to detect patterns in geospatial datasets," *Remote Sensing of Environment*, vol. 156, pp. 11 – 20, 2015.

[70] G. Darbellay and I. Vajda, "Estimation of the information by an adaptive partitioning of the observation space," *IEEE Transactions on Information Theory*, vol. 45, no. 4, pp. 1315–1321, 1999. cited By 237.

[71] M. G. Schultz, H. Akimoto, J. Bottenheim, B. Buchmann, I. E. Galbally, S. Gilge, D. Helmig, H. Koide, A. C. Lewis, P. C. Novelli, C. Plass-Dülmer, T. B. Ryerson, M. Steinbacher, R. Steinbrecher, O. Tarasova, K. Tørseth, V. Thouret, and C. Zellweger, "The Global Atmosphere Watch reactive gases measurement network," *Elementa: Science of the Anthropocene*, vol. 3, 10 2015. 000067.

[72] K. Thoning, A. Crotwell, and J. Mund, "Atmospheric carbon dioxide dry air mole fractions from continuous measurements at mauna loa, hawaii, barrow, alaska, american samoa and south pole," 2020. 1973-2019, Version 2020-08 National Oceanic and Atmospheric Administration (NOAA), Global Monitoring Laboratory (GML), Boulder, Colorado, USA.

[73] J. C. Pales and C. D. Keeling, "The concentration of atmospheric carbon dioxide in hawaii," *Journal of Geophysical Research (1896-1977)*, vol. 70, no. 24, pp. 6053–6076, 1965.

[74] C. D. Keeling, R. B. Bacastow, A. E. Bainbridge, C. A. E. Jr., P. R. Guenther, L. S. Waterman, and J. F. S. Chin, "Atmospheric carbon dioxide variations at mauna loa observatory, hawaii," *Tellus*, vol. 28, no. 6, pp. 538–551, 1976.

[75] G. L. Vaghjiani, "New measurement of the rate coefficient for the reaction of oh with methane," *Nature*, vol. 350, pp. 406–409, 1991.

[76] J. M. Harris, P. P. Tans, E. J. Dlugokencky, K. A. Masarie, P. M. Lang, S. Whittlestone, and L. P. Steele, "Variations in atmospheric methane at mauna loa observatory related to long-range transport," *Journal of Geophysical Research: Atmospheres*, vol. 97, no. D5, pp. 6003–6010, 1992.

[77] A. I. et al., "Decadal trends in the seasonal-cycle amplitude of terrestrial co2 exchange resulting from the ensemble of terrestrial biosphere models," *Tellus B: Chemical and Physical Meteorology*, vol. 68, no. 1, p. 28968, 2016.

[78] K. W. Thoning, P. P. Tans, and W. D. Komhyr, "Atmospheric carbon dioxide at mauna loa observatory: 2. analysis of the noaa gmcc data, 1974–1985," *Journal of Geophysical Research: Atmospheres*, vol. 94, no. D6, pp. 8549–8565, 1989.

[79] Y. Yuan, L. Ries, H. Petermeier, T. Trickl, M. Leuchner, C. Couret, R. Sohmer, F. Meinhardt, and A. Menzel, "On the diurnal, weekly, and seasonal cycles and annual trends in atmospheric co2 at mount zugspitze, germany, during 1981–2016," *Atmospheric Chemistry and Physics*, vol. 19, no. 2, pp. 999–1012, 2019.

[80] G. Sreenivas, P. Mahesh, J. Subin, A. L. Kanchana, P. V. N. Rao, and V. K. Dadhwal, "Influence of meteorology and interrelationship with greenhouse gases (co_2 and ch_4) at a suburban site of india," *Atmospheric Chemistry and Physics*, vol. 16, no. 6, pp. 3953–3967, 2016.

[81] T. NAKAZAWA, S. AOKI, S. MURAYAMA, M. FUKABORI, T. YAMANOUCHI, H. MURAYAMA, M. SHIOBARA, G. HASHIDA, S. KAWAGUCHI, and M. TANAKA, "The concentration of atmospheric carbon dioxide at the japanese antarctic station, syowa," *Tellus B*, vol. 43, no. 2, pp. 126–135, 1991.

[82] M. D. Dettinger and M. Ghil, "Seasonal and interannual variations of atmospheric co2 and climate," *Tellus B: Chemical and Physical Meteorology*, vol. 50, no. 1, pp. 1–24, 1998.

[83] F. Zhang, L. Zhou, T. J. Conway, P. P. Tans, and Y. Wang, "Short-term variations of atmospheric co2 and dominant causes in summer and winter: Analysis of 14-year continuous observational data at waliguan, china," *Atmospheric Environment*, vol. 77, pp. 140–148, 2013.

[84] W. D. C. for Greenhouse Gases (WDCGG), "Atmospheric co_2 hourly concentration data," 2010.

[85] D. H. Ehhalt, "The atmospheric cycle of methane," *Tellus*, vol. 26, no. 1-2, pp. 58–70, 1974.

[86] M. Saunois, A. R. Stavert, B. Poulter, P. Bousquet, J. G. Canadell, R. B. Jackson, P. A. Raymond, E. J. Dlugokencky, S. Houweling, P. K. Patra, P. Ciais, V. K. Arora, D. Bastviken, P. Bergamaschi, D. R. Blake, G. Brailsford, L. Bruhwiler, K. M. Carlson, M. Carrol, S. Castaldi, N. Chandra, C. Crevoisier, P. M. Crill, K. Covey, C. L. Curry, G. Etiope, C. Frankenberg, N. Gedney, M. I. Hegglin, L. Höglund-Isaksson, G. Hugelius, M. Ishizawa, A. Ito, G. Janssens-Maenhout, K. M. Jensen, F. Joos, T. Kleinen, P. B. Krummel, R. L. Langenfelds, G. G. Laruelle, L. Liu, T. Machida, S. Maksyutov, K. C. McDonald, J. McNorton, P. A. Miller, J. R. Melton, I. Morino, J. Müller, F. Murguia-Flores, V. Naik, Y. Niwa, S. Noce, S. O'Doherty, R. J. Parker, C. Peng, S. Peng, G. P. Peters, C. Prigent, R. Prinn, M. Ramonet, P. Regnier, W. J. Riley, J. A. Rosentreter, A. Segers, I. J. Simpson, H. Shi, S. J. Smith, L. P. Steele, B. F. Thornton, H. Tian, Y. Tohjima, F. N. Tubiello, A. Tsuruta, N. Viovy, A. Voulgarakis, T. S. Weber, M. van Weele, G. R. van der Werf, R. F. Weiss, D. Worthy, D. Wunch, Y. Yin, Y. Yoshida, W. Zhang, Z. Zhang, Y. Zhao, B. Zheng, Q. Zhu, Q. Zhu, and Q. Zhuang, "The global methane budget 2000–2017," *Earth System Science Data*, vol. 12, no. 3, pp. 1561–1623, 2020.

[87] C. R. F. W. E. Bréas, O. Guillou, "The global methane cycle: isotopes and mixing ratios, sources and sinks," *Isotopes Environ Health Stud.*, vol. 37, no. 4, pp. 257–379, 2001.

[88] D. Taraborrelli, D. Cabrera-Perez, S. Bacer, S. Gromov, J. Lelieveld, J. Sodeau, and A. Pozzer, "Influence of aromatics on tropospheric

gas-phase composition," *Atmospheric Chemistry and Physics*, vol. 21, pp. 2615–2636, 02 2021.

[89] P. C. Novelli, K. A. Masarie, and P. M. Lang, "Distributions and recent changes of carbon monoxide in the lower troposphere," *Journal of Geophysical Research: Atmospheres*, vol. 103, no. D15, pp. 19015–19033, 1998.

[90] T. R. Lee, S. F. J. D. Wekker, S. Pal, A. E. Andrews, and J. Kofler, "Meteorological controls on the diurnal variability of carbon monoxide mixing ratio at a mountaintop monitoring site in the appalachian mountains," *Tellus B: Chemical and Physical Meteorology*, vol. 67, no. 1, p. 25659, 2015.

[91] S. Henne, J. Klausen, W. Junkermann, J. M. Kariuki, J. O. Aseyo, and B. Buchmann, "Representativeness and climatology of carbon monoxide and ozone at the global gaw station mt. kenya in equatorial africa," *Atmospheric Chemistry and Physics*, vol. 8, no. 12, pp. 3119–3139, 2008.

[92] J. Forrer, R. Rüttimann, D. Schneiter, A. Fischer, B. Buchmann, and P. Hofer, "Variability of trace gases at the high-alpine site jungfraujoch caused by meteorological transport processes," *Journal of Geophysical Research*, vol. 105, pp. 12241–12251, 2000.

[93] R. Eskridge, M. Ku, S. Rao, P. Porter, and I. Zurbenko, "Separating different scales of motion in time series of meteorological variables," *Bulletin of The American Meteorological Society - BULL AMER METEOROL SOC*, vol. 78, pp. 1473–1483, 07 1997.

[94] S. T. Rao and I. Zurbenko, "Detecting and tracking changes in ozone air quality," *Air Waste Manag. Assoc*, vol. 44, p. 1089–1095, 1994.

[95] I. Zurbenko, "The spectral analysis of time series (north-holland series in statistics and probability)," *Elsevier Science Ltd*, vol. 78, 1986.

[96] R. Fisher, "The correlation between relatives on the supposition of mendelian inheritance," *Philosophical Transactions of the Royal Society of Edinburgh*, vol. 52, pp. 399–433, 1918.

[97] E. Boegh, H. Soegaard, N. Broge, C. Hasager, N. Jensen, K. Schelde, and A. Thomsen, "Airborne multispectral data for quantifying leaf area index, nitrogen concentration, and photosynthetic efficiency in agriculture," *Remote Sensing of Environment*, vol. 81, no. 2, pp. 179–193, 2002.

[98] A. R. Huete, K. Didan, Y. E. Shimabukuro, P. Ratana, S. R. Saleska, L. R. Hutyra, W. Yang, R. R. Nemani, and R. Myneni, "Amazon rainforests green-up with sunlight in dry season," *Geophysical Research Letters*, vol. 33, no. 6, 2006.

[99] K. Esteki, N. Prakash, Y. Li, C. Mu, and K. Du, "Seasonal variation of co2 vertical distribution in the atmospheric boundary layer and impact of meteorological parameters," *International Journal of Environmental Research*, vol. 11, 11 2017.

[100] P. K. Shaw, S. Ghosh, D. Saha, M. S. Janaki, and A. N. S. Iyengar, "Investigation of coherent modes and their role in intermittent oscillations using empirical mode decomposition," *Physics of Plasmas*, vol. 23, no. 11, p. 112103, 2016.

[101] P. K. Shaw, D. Saha, S. Ghosh, M. Janaki, and A. S. Iyengar, "Investigation of coherent modes in the chaotic time series using empirical mode decomposition and discrete wavelet transform analysis," *Chaos, Solitons & Fractals*, vol. 78, pp. 285–296, 2015.

[102] W. J. STASZEWSKI and K. WORDEN, "Wavelet analysis of time-series: Coherent structures, chaos and noise," *International Journal of Bifurcation and Chaos*, vol. 09, no. 03, pp. 455–471, 1999.

[103] G. Casella and R. L. Berger, *Statistical Inference Vol. 70*. Duxbury Press Belmont, Ca, 1990.

[104] A. F. Tuck, "From molecules to meteorology via turbulent scale invariance," *Quarterly Journal of the Royal Meteorological Society*, vol. 136, no. 650, pp. 1125–1144, 2010.

[105] S. Lovejoy, D. Schertzer, and A. Tuck, "Fractal aircraft trajectories and nonclassical turbulent exponents," *Physical review. E, Statistical, nonlinear, and soft matter physics*, vol. 70, p. 036306, 09 2004.

[106] R. A. Rios and R. F. de Mello, "Applying empirical mode decomposition and mutual information to separate stochastic and deterministic influences embedded in signals," *Signal Processing*, vol. 118, pp. 159 – 176, 2016.

[107] A. Jerri, "The shannon sampling theorem—its various extensions and applications: A tutorial review," *Proceedings of the IEEE*, vol. 65, no. 11, pp. 1565–1596, 1977.

[108] Z. Wu and N. E. Huang, "A study of the characteristics of white noise using the empirical mode decomposition method," *Proceedings of the Royal Society of London. Series A: Mathematical, Physical and Engineering Sciences*, vol. 460, pp. 1597 – 1611, 2004.

[109] Z. Wu, E. Schnneider, Z.-Z. Hu, and L. Cao, "The impact of global warming on enso variability in climate records," 01 2002.

[110] G. WANG, X.-Y. CHEN, F.-L. QIAO, Z. WU, and N. E. HUANG, "On intrinsic mode function," *Advances in Adaptive Data Analysis*, vol. 02, no. 03, pp. 277–293, 2010.

[111] B. Efron and R. Tibshirani, "Bootstrap methods for standard errors, confidence intervals, and other measures of statistical accuracy," *Statist. Sci.*, vol. 1, pp. 54–75, 02 1986.

[112] A. N. Kolmogorov, V. Levin, J. C. R. Hunt, O. M. Phillips, and D. Williams, "The local structure of turbulence in incompressible viscous fluid for very large reynolds numbers," *Proceedings of the Royal Society of London. Series A: Mathematical and Physical Sciences*, vol. 434, no. 1890, pp. 9–13, 1991.

[113] M. A. W. W. Davis, A. and R. Cahalan, "Multifractal characterizations of nonstationarity and intermittency in geophysical fields: Observed, retrieved, or simulated," *Journal of Geophysical Research: Atmospheres*, vol. 99, no. D4, pp. 8055–8072, 1994.

[114] O. D. Medina, F. G. Schmitt, and R. Calif, "Multiscale analysis of wind velocity, power output and rotation of a windmill," *Energy Procedia*, vol. 76, pp. 193–199, 2015. European Geosciences Union General Assembly 2015 - Division Energy, Resources and Environment, EGU 2015.

[115] R. Baile and J.-F. m. c. Muzy, "Spatial intermittency of surface layer wind fluctuations at mesoscale range," *Phys. Rev. Lett.*, vol. 105, p. 254501, Dec 2010.

[116] G. Ruiz-Chavarria, S. Ciliberto, C. Baudet, and E. Lévêque, "Scaling properties of the streamwise component of velocity in a turbulent boundary layer," *Physica D: Nonlinear Phenomena*, vol. 141, no. 3, pp. 183–198, 2000.

[117] F. G. Schmitt, "Linking eulerian and lagrangian structure functions' scaling exponents in turbulence," *Physica A: Statistical Mechanics and its Applications*, vol. 368, no. 2, pp. 377–386, 2006.

[118] A. B. Chelani, "Persistence analysis of extreme co, no2 and o3 concentrations in ambient air of delhi," *Atmospheric Research*, vol. 108, pp. 128 – 134, 2012.

[119] D. Sims, F. Rahman, V. Cordova, B. El Masri, D. Baldocchi, L. Flanagan, A. Goldstein, D. Hollinger, L. Misson, R. Monson, W. Oechel, H. Schmid, S. Wofsy, and L. Xu, "On the use of modis evi to assess gross primary productivity of north american ecosystems: Estimation of gpp from modis evi," *Journal of Geophysical Research: Biogeosciences*, vol. 111, pp. n/a–n/a, 12 2006.

[120] J. A. Taylor, "Atmospheric mixing and the co2 seasonal cycle," *Geophysical Research Letters*, vol. 25, no. 22, pp. 4173–4176, 1998.

[121] J. M. Harris, P. P. Tans, E. J. Dlugokencky, K. A. Masarie, P. M. Lang, S. Whittlestone, and L. P. Steele, "Variations in atmospheric methane at mauna loa observatory related to long-range transport," *Journal of Geophysical Research: Atmospheres*, vol. 97, no. D5, pp. 6003–6010, 1992.

[122] S. Dutta, "A multifractal analysis of time series of atmospheric co2 concentration," *International Journal of Global Warming*, vol. 14, p. 1, 01 2018.

[123] P. Talkner and R. O. Weber, "Power spectrum and detrended fluctuation analysis: Application to daily temperatures," *Phys. Rev. E*, vol. 62, pp. 150–160, Jul 2000.

[124] Y. Ashkenazy, S. Havlin, P. C. Ivanov, C.-K. Peng, V. Schulte-Frohlinde, and H. Stanley, "Magnitude and sign scaling in power-law correlated time series," *Physica A: Statistical Mechanics and its Applications*, vol. 323, pp. 19 – 41, 2003.

[125] P. Mouzourides, A. Kyprianou, and M. K.-A. Neophytou, "Exploring the multi-fractal nature of the air flow and pollutant dispersion in a turbulent urban atmosphere and its implications for long range pollutant transport," *Chaos: An Interdisciplinary Journal of Nonlinear Science*, vol. 31, no. 1, p. 013110, 2021.

[126] Y. X. Huang, F. G. Schmitt, J.-P. Hermand, Y. Gagne, Z. M. Lu, and Y. L. Liu, "Arbitrary-order hilbert spectral analysis for time series possessing scaling statistics: Comparison study with detrended fluctuation analysis and wavelet leaders," *Phys. Rev. E*, vol. 84, p. 016208, Jul 2011.